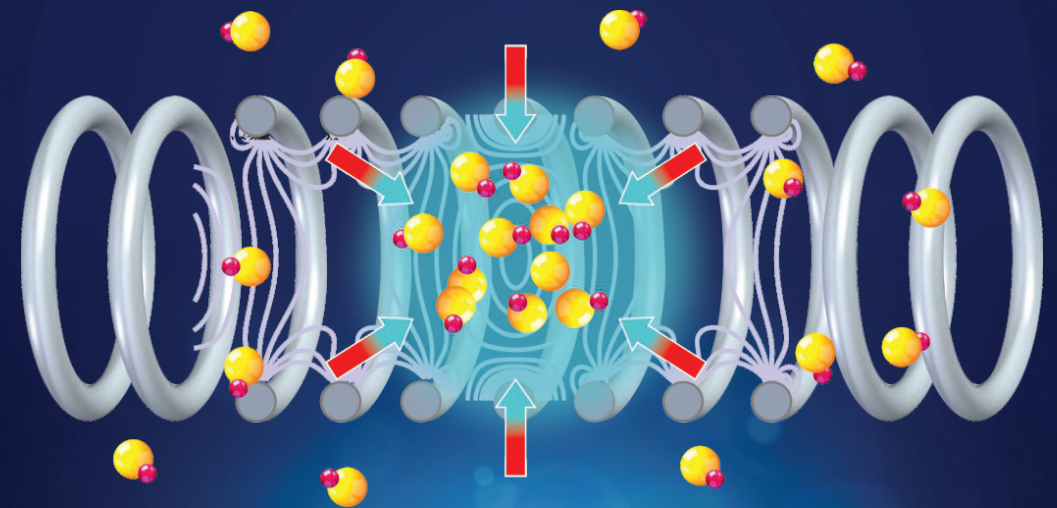


# Production, Deceleration and Trapping of SrF molecules



Parul Aggarwal

University of Groningen

## Production, deceleration and trapping of SrF molecules

Aggarwal, Parul

**IMPORTANT NOTE:** You are advised to consult the publisher's version (publisher's PDF) if you wish to cite from it. Please check the document version below.

*Document Version*

Publisher's PDF, also known as Version of record

*Publication date:*

2021

[Link to publication in University of Groningen/UMCG research database](#)

*Citation for published version (APA):*

Aggarwal, P. (2021). *Production, deceleration and trapping of SrF molecules*. University of Groningen.

### Copyright

Other than for strictly personal use, it is not permitted to download or to forward/distribute the text or part of it without the consent of the author(s) and/or copyright holder(s), unless the work is under an open content license (like Creative Commons).

### Take-down policy

If you believe that this document breaches copyright please contact us providing details, and we will remove access to the work immediately and investigate your claim.

*Downloaded from the University of Groningen/UMCG research database (Pure): <http://www.rug.nl/research/portal>. For technical reasons the number of authors shown on this cover page is limited to 10 maximum.*



# **Production, deceleration and trapping of SrF molecules**

*The cover depicts a fraction of the SrF molecular beam trapped in a single electric field minima created inside the ring electrodes of the traveling-wave Stark decelerator.*



The work in this thesis has been carried out at the Van Swinderen Institute for Particle Physics and Gravity of the University of Groningen. This work is done as part of the NL-eEDM consortium which receives funding (EEDM-166) from the Netherlands Organisation for Scientific Research (NWO).

Cover : Jasmeet Jassal, Parul Aggarwal  
Printing : Gildeprint, The Netherlands





university of  
 groningen

# **Production, deceleration and trapping of SrF molecules**

**PhD thesis**

to obtain the degree of PhD at the  
University of Groningen  
on the authority of the  
Rector Magnificus Prof. C. Wijmenga  
and in accordance with  
the decision by the College of Deans.

This thesis will be defended in public on

Friday 27 August 2021 at 9.00 hours

by

**Parul Aggarwal**

born on 5 June 1994  
in Punjab, India

**Supervisor**

Prof. S. Hoekstra

**Co-supervisor**

Prof. K.H.K.J. Jungmann

**Assessment Committee**

Prof. C.H. van der Wal

Prof. F.E. Schreck

Prof. S. Ospelkaus-Schwarzer



# Contents

<b>1</b>	<b>Introduction</b>	<b>1</b>
1.1	Beyond the Standard Model . . . . .	1
1.2	Electric dipole moments . . . . .	3
1.3	Measurement principle . . . . .	4
1.4	History of eEDM experiments . . . . .	7
1.5	Advances in the production of intense, cold and slow molecular beams . . . . .	9
1.5.1	Molecular beam sources . . . . .	9
1.5.2	Techniques for slowing and trapping the molecules. . . . .	10
1.5.3	Trapping . . . . .	12
1.6	eEDM experiments using polar molecules . . . . .	14
1.7	The NL-eEDM experiment. . . . .	16
1.8	Outline of the thesis . . . . .	18
<b>2</b>	<b>Molecular structure and theory</b>	<b>21</b>
2.1	Energy structure of molecules . . . . .	21
2.2	Electronic energy level structure . . . . .	22
2.3	Vibrational energy levels . . . . .	23
2.4	Rotational energy levels . . . . .	23
2.5	Coupling of angular momentum: Hund's cases. . . . .	24
2.6	Spin-orbit and spin-rotation, hyperfine structure and $\lambda$ -doubling terms . . . . .	25
2.6.1	Spin-rotation and hyperfine structure in $^2\Sigma$ state . . . . .	25
2.6.2	Spin-orbit and lambda-doubling structure in $^2\Pi$ state . . . . .	26
2.7	Selection rules . . . . .	30
2.8	Field-Molecule interaction . . . . .	31
2.8.1	Stark effect . . . . .	31
2.8.2	Zeeman effect . . . . .	34
2.9	Conclusions. . . . .	35
<b>3</b>	<b>A supersonic laser ablation beam source of SrF and BaF molecules</b>	<b>37</b>
3.1	Experimental setup. . . . .	38
3.2	Lasers . . . . .	39
3.3	Data Acquisition System. . . . .	40
3.4	Results . . . . .	41
3.4.1	Time of flight profile . . . . .	41
3.4.2	Relative velocity spread . . . . .	45
3.4.3	Optimisation of the beam . . . . .	45
3.4.4	Backing pressure variation . . . . .	47
3.4.5	Rotational temperature. . . . .	47
3.4.6	Number of molecules . . . . .	48

3.5	Comparison with other work . . . . .	50
3.6	Outlook . . . . .	51
<b>4</b>	<b>Lifetime measurements of the <math>A^2\Pi_{1/2}</math> and <math>A^2\Pi_{3/2}</math> states in BaF</b>	<b>53</b>
4.1	Introduction . . . . .	53
4.2	Method. . . . .	54
4.3	Results . . . . .	56
4.4	Conclusion . . . . .	60
<b>5</b>	<b>Deceleration of SrF molecules in a 4 m long decelerator</b>	<b>61</b>
5.1	Operational principle of a traveling-wave Stark decelerator . . . . .	62
5.2	Experimental set-up . . . . .	63
5.2.1	Molecular source . . . . .	63
5.2.2	Design of Traveling-wave Stark decelerator. . . . .	64
5.2.3	Detection system . . . . .	65
5.3	Results . . . . .	66
5.3.1	Absorption signal of SrF beam from the cryogenic source . . . . .	66
5.3.2	Guiding. . . . .	68
5.3.3	Deceleration measurements. . . . .	73
5.4	Number of molecules. . . . .	74
5.5	Conclusion . . . . .	78
<b>6</b>	<b>Trapping of SrF molecules in a 4.5 m long decelerator</b>	<b>79</b>
6.1	Experimental setup recap . . . . .	79
6.2	Results . . . . .	82
6.2.1	Guiding of SrF molecules. . . . .	82
6.2.2	Deceleration of SrF molecules . . . . .	84
6.2.3	Analysis of the peak substructure for the calculation of longitudinal position and velocity spread . . . . .	87
6.2.4	Transverse position and velocity spread . . . . .	92
6.3	Stopping and trapping of molecules . . . . .	94
6.3.1	Experimental and simulation results . . . . .	95
6.3.2	Lifetime of the molecules in the electric trap. . . . .	96
6.3.3	Longitudinal velocity and position spread of the trapped molecular beam . . . . .	96
6.4	Number of molecules. . . . .	98
6.5	Conclusion and outlook . . . . .	102
<b>7</b>	<b>Summary and Outlook</b>	<b>103</b>
<b>8</b>	<b>Nederlandse Samenvatting</b>	<b>109</b>
	<b>Bibliography</b>	<b>115</b>
	<b>List of Publications</b>	<b>133</b>
	<b>Acknowledgements</b>	<b>135</b>



# 1

## Introduction

We shall not cease from exploration and the end of all our exploration will be to arrive where we started and know the place for the first time.-Thomas Stearns Eliot

The Standard Model (SM) of Particle Physics describes all known fundamental particles and three out of the four known fundamental interactions, i.e the electromagnetic, weak and strong interactions leaving out gravity [1]. Most of its foundational elements were developed over fifty years ago including the seminal Higgs mechanism [2, 3, 4], electroweak gauge symmetry [5, 6] and discoveries of asymptotic freedom [7, 8]. The SM has been rigorously tested since its completion with probes of energy three orders of magnitude higher than were possible when it first was introduced, but all its predictions have been confirmed with unparalleled precision. The discovery of charm [9, 10] and bottom quark [11], tau lepton [12], gluons [13], W and Z bosons [14, 15], the top quark [16, 17], tau neutrino [18] and most recently Higgs boson [19] have strengthened its validity. The SM, however, does not provide a complete explanation of the world around us. The SM does not currently provide answers to some intriguing open questions in physics: What is dark matter and dark energy? Why do we observe so much more matter than antimatter despite the laws of physics treating them both nearly equivalently? Why do the elementary particles have the mass values that they have? Why is the top-quark so heavy? Why are there three families of fundamental fermions? All unanswered questions such as these provide strong motivation to look for new physics beyond the present SM.

### 1.1. Beyond the Standard Model

The SM describes low energy particles with their strong non-gravitational couplings. Physics beyond the SM can appear in the form of massive particles or weakly coupled particles with coupling constants at inverse energy scales ( $g \approx 10 \text{ GeV}^{-1}$ ). The supersymmetric extensions of the SM predict new particles with masses up to several TeV [20] and light QCD axions with masses of order meV, with coupling constants  $g \approx 10^{-13} \text{ GeV}^{-1}$  [21]. New physics could

also appear in the form of modified Newtonian dynamics in which the gravitational forces are reduced in the low acceleration limit [22]. There are a variety of other possibilities for extending the SM in order to explain some of the observed features in nature that lack a deeper explanation within the SM. They have been already discussed extensively in the literature [23].

One way of looking out for yet undiscovered massive elementary particles is at use at the Large Hadron Collider in CERN, where the protons are made to collide at high energies in the TeV range and the particles produced are detected or inferred from their decay products. The other way is to look at the properties of already known fundamental particles with high precision. The fundamental particles like electrons, neutrons interact with the quantum fields of other elementary particles, which can lead to changes in their properties. These changes can be investigated with high precision in the lab, thanks to the large technological advances in the past few decades. Precision experiments open a window to look for the new particles in an indirect way, which might be difficult to be directly produced in the lab.

The measurements of the anomalous magnetic moment of the muon ( $a_\mu$ ) [24], which started in the 1960ies provide for precise tests of the SM since and have yielded limits on the muon's electric dipole moment ( $d_\mu$ ) [25]. The most recent experiment at Brookhaven National Laboratory set the bound on the muon EDM at  $|d_\mu| < 1.8 \times 10^{-19}$  e.cm (95% C.L) [26]. The limit represents an improvement by a factor of 5 over the previous results. The measurement of the anomalous magnetic moment of the muon appears to show a  $\sim 3.5$  standard deviation difference between the experiment and theory [27]. A new experiment is now underway at Fermilab, US which aims for a factor 10 improvement on  $d_\mu$  and a factor 5 improvement on  $a_\mu$ . The first results of the muon g-2 experiment at Fermilab show a 4.2 standard deviation difference between the experiment and theory [28]. Any verification of the discrepancy in the  $a_\mu$  could be a sign of new physics [29].

The magnetic moment of the electron has also been used to test [30, 31, 32] and verify our understanding of the theory of particle physics with greater than ten decimal digits of fractional precision. Also, the interaction of the electron with the new particles can impart the electron an electric dipole moment (eEDM). A non-zero value of eEDM would violate the  $\mathcal{T}$ -symmetry and in turn,  $\mathcal{CP}$  symmetry provided the  $\mathcal{CP}\mathcal{T}$  theorem holds. The SM of particle physics predicts for the electron an EDM of the order  $10^{-38}$  e.cm. Within the SM, the EDMs cannot appear at tree level [33, 34, 35]. It arises in higher-order loops and therefore the predicted value of eEDM by the SM is very small. In the framework of SM extensions, which are proposed to explain observations not yet covered by the SM, the eEDM could be larger with the specifics of the interaction between the electron and the new particle depending on the respective theoretical model. The contribution to the permanent electric dipole moment ( $d_e$ ) of the electron due to its interaction with new yet undiscovered particles is expected at [36]

$$d_e = C \frac{m_e}{m_X^2} \sin(\phi_{\mathcal{CP}}), \quad (1.1)$$

where  $m_e$  is the mass of the electron,  $m_X$  is the mass of the new particle,  $\phi_{\mathcal{CP}}$  is a  $\mathcal{CP}$ -violating phase describing the process and  $C$  is the coupling constant that determines the strength of the interaction. The difficult part is that the values of  $C$ ,  $\phi_{\mathcal{CP}}$ ,  $m_X$  are unknown. In various models, the value of  $C$  is assumed to be of the order  $\simeq \alpha/2\pi$  where  $\alpha$  is the fine

structure constant and  $\phi_{CP} \sim 1$  [37]. With these assumptions, the recent experimental limit on the permanent electric dipole moment of the electron  $|d_e| < 1.1 \times 10^{-29}$  e.cm (90% confidence) by the ACME collaboration set bounds on the masses of new particles, which appear as virtual particles in the loops, in the range 3-30 TeV [38].

## 1.2. Electric dipole moments

The dipole moment for a system of two discrete opposite charges  $+q$  and  $-q$  separated by a distance  $\vec{r}$ , is given by the product  $q\vec{r}$ . For a fundamental particle like an electron with a homogeneous charge density  $\rho(\vec{r})$  and an EDM,  $\vec{d}_e$ , the  $\vec{d}_e$  for a distance  $\vec{r}$  from the center of mass and volume element  $dV$  has the following form [39]

$$\vec{d}_e = \int_V \rho(\vec{r}) \vec{r} dV. \quad (1.2)$$

In physical terms, it is the polarisation of the vacuum field close to the electron. The direction of the electric dipole moment vector is bound to be along the same axis as the direction of the spin of the electron,  $\vec{d}_e = d_e \frac{\vec{s}}{|\vec{s}|}$ . An independent direction of  $d_e$  from the spin would be in disagreement with elementary quantum mechanics. A permanent electric dipole moment violates both parity ( $\mathcal{P}$ ) and time-reversal symmetry ( $\mathcal{T}$ ). The violation of  $\mathcal{T}$  and  $\mathcal{P}$  symmetry by the electron EDM can be understood by the transformation of  $H_{d_e}$  under  $\mathcal{P}$  and  $\mathcal{T}$  symmetry.  $\vec{S}$  is odd under time-reversal and even under parity transformation and the electric field ( $\vec{E}$ ) is odd under parity transformation and even under time-reversal. Therefore,  $H_{d_e}$  transforms as

$$\mathcal{T} : H_{d_e} \rightarrow -2d_e(-\vec{s}) \cdot \vec{E} = -H_{d_e} \quad (1.3)$$

$$\mathcal{P} : H_{d_e} \rightarrow -2d_e\vec{s} \cdot (-\vec{E}) = -H_{d_e}. \quad (1.4)$$

This is also essentially the difference between the EDM of a fundamental particle and the EDM of a classical charge distribution, which is odd under  $\mathcal{P}$  and even under  $\mathcal{T}$  transformation.  $\mathcal{T}$  violation is equivalent to  $C\mathcal{P}$  violation, provided the  $C\mathcal{P}\mathcal{T}$  theorem holds.

$C\mathcal{P}$  violation has been suggested as one of the possible mechanisms to explain the matter-antimatter asymmetry prevalent in the universe [40] in a state of thermal non-equilibrium and with baryon number violating processes. The observed dominance of matter over anti-matter could, however also be explained by  $C\mathcal{P}\mathcal{T}$  violation, even without the need for thermal non-equilibrium and many other assumptions [41, 42]. Experiments that test Lorentz invariance and  $C\mathcal{P}\mathcal{T}$  conservation have been conducted, although no breaking of these symmetries has been found so far. As an example, an experiment to test Lorentz and  $C\mathcal{P}\mathcal{T}$  invariance in the electromagnetic interactions used a comagnetometer which is based on the detection of the freely spin precessing nuclear spins from polarised  $^{129}\text{Xe}$  and  $^3\text{He}$ . The experiment searches for sidereal variation of the spin precession frequencies of colocated species, i.e. modulation of the frequency ratio as a function of the rotation of the earth and hence the laboratory reference frame [43, 44]. The Lorentz invariance in weak interactions was searched for at the TRIUMF facility in Groningen. The experiment searches for a dependence of the lifetime of  $^{20}\text{Na}$  nuclei on the nuclear spin direction in the universe by

exploiting the rotation of the earth. Any difference in the lifetime between nuclei polarised in different directions would be a signature of Lorentz invariance and  $\mathcal{CPT}$  violation. A limit of  $2 \times 10^{-4}$  (90% C.L) on the amplitude of the sidereal variation with the relative lifetime difference was set by the experiment [45].

### 1.3. Measurement principle

The searches for EDMs of the fundamental particles are categorised based on the physical systems on which the experiment is performed: electrons, muons, tauons, nucleons, nuclei, atoms, ions, molecules and condensed matter systems. Any measured EDM for the leptons, electron, muon and tauon is an intrinsic property of the particle because they do not have any known substructure. Neutrons and protons consist of quarks. The EDM of neutron and proton can therefore be due to the EDM of the constituent quarks or the interaction between the quarks. The measured EDM of the atom, ion, molecule and condensed matter system, depending upon their electronic configuration could be an indication of the EDM of the electron or nuclei. Whereas in paramagnetic systems, the sensitivity to an EDM on the electron is favoured, in diamagnetic systems, to leading order, the potential electron EDM contributions from the various electrons would cancel. The EDMs of diamagnetic systems can be due to the dominant contributions from nuclear EDMs and nucleon-nucleon interactions (which may be many times larger than the EDM of a single nucleon) [46]. These latter two contributions are described by a common coupling constant called Nuclear Schiff Moment  $Q$ . Additionally, iso-scalar and isovector nuclear-pion interaction  $g_\pi^{(0)}$  and  $g_\pi^{(1)}$  and scalar and tensor electron-nucleon interactions  $C_s$  and  $C_T$  can also contribute to EDMs of diamagnetic systems [46].

In this section, we will primarily focus on the extraction of the electron EDM from the measurement on paramagnetic atomic and molecular systems. The basic idea to measure the EDM of an electron is to place it in the presence of the external electric field ( $\mathcal{E}$ ) and look for a change in energy proportional to the applied electric field, given by the Hamiltonian  $-d_e \cdot \mathcal{E}$ .<sup>\*</sup> Some of the earlier measurements of the eEDM were performed on free electrons, as part of the experiments that measured the anomalous magnetic moment of the electron [49, 50]. However, there were a lot of complications aided by the acceleration of the electron in an external electric field, resulting in reduced interaction time and increased complexity. Most successful experiments have used the open-shell atomic and molecular systems to measure the eEDM, an extensive review of which can be found in [51].

The challenge is to extract a value or limit on the eEDM from the response of neutral atoms and molecules with a single unpaired electron. The theoretical investigation to look into it began in the 1960s [52]. In the beginning, it was pointed out that even if the electron had an electric dipole moment, it might never be detected in a neutral system. Electrons cannot experience an external electric field without being subjected to acceleration and since the orbiting electrons cannot be accelerated, the net field experienced by them should be zero.

---

<sup>\*</sup>Note that the limit on the EDM of the leptons was also interpreted from the lifetime measurement of metastable state [47] and also from a good agreement between the experiment and theory for the transition frequency [48].

Since the Lorentz force is the only force at play here, the electric field experienced by all electrons and nucleons should be zero. In other words, the field on average at each charged point would be cancelled by the re-arrangement of other charges [53].

It was later pointed out by Schiff, that this might not be the case for real atoms, where finite volume and relativistic effects come into the picture [52]. Due to the finite volume, the charge might be distributed non-uniformly leading to the possibility of imperfect shielding. Further, due to the relativistic motion of electrons close the nucleus, the dipole moment experiences length contraction. So, even if the average electric field vanishes, the interaction energy between the electric field and eEDM may still be non-vanishing. Later, Sandars recognized that the energy shifts experienced in atoms and molecules due to the electron dipole moment and field interaction would not only be non-vanishing but also larger than the shifts due to a free electron [54]. The relativistic effects add a correction term to the interaction Hamiltonian-

$$H' = \frac{\gamma}{1+\gamma} \vec{\beta} \cdot \vec{d}_e \vec{\beta} \cdot \vec{E}, \quad (1.5)$$

where  $\vec{\beta} = \vec{v}/c$  and  $\gamma = \frac{1}{\sqrt{1-\beta^2}}$  is the Lorentz factor.

This term results in a non-zero expectation value for the energy Hamiltonian. The energy shift is then given as  $U_{EDM} = -\langle d_e \rangle \cdot E_{\text{eff}}$ , where  $E_{\text{eff}}$  is the effective electric field. This energy shift can be significantly larger than the applied electric field. The purpose of the laboratory electric field is to polarise the atomic system. Based on this recognition, subsequent eEDM experiments were conducted by exploiting the properties of heavy atoms. The most successful amongst them being Cs [55, 56, 57, 58] and Tl [59, 60, 61], which have enhancement factors for external fields of 120 and -58 [62], respectively. The enhancement factors arise from detailed calculations of the atomic structure.

The progress in AMO techniques such as cooling, trapping, quantum state control combined with advances in laser technology led to improvements in precision experiments. The atomic eEDM experiments improved the eEDM limit by almost 12 orders of magnitude. It was recognized by Sandars, that through exploiting polar diatomic molecules, the enhancement can be increased even further [63]. The external field polarises the molecules by mixing states of opposite parity. For polar molecules, the small energy difference between the opposite parity eigenstates means the electric field required to polarise the molecules can be very small, a few V/cm for some molecules. For atoms, the opposite parity eigenstates are separated by eV energy scales and are polarised only partially by the lab electric field. The energy shift is therefore given by

$$U_{EDM} = -d_e \eta E_{\text{eff}}, \quad (1.6)$$

where  $\eta$  is the degree of polarisation. Generally, the effective electric field scales with the third power of the atomic number,  $E_{\text{eff}} \propto Z^3$ . Effective electric fields for polar molecules can be as large as tens of GV/cm at typical lab electric fields. In the case of ThO, the effective electric field is  $\approx 80$  GV/cm [64] with electric fields on the order of 10 V/cm.

To measure the eEDM using atoms and molecules: Firstly, with selective population and depletion, a pure spin state is prepared, such as the  $|F, m_F\rangle = |0, 0\rangle$  hyperfine state of the electronic ground state  $X^2\Sigma^+$  ( $\nu = 0, N = 0$ ) (for e.g. in heavy paramagnetic molecular systems YbF and BaF). The molecules will be transferred to an equal superposition of the  $m_F = 1$  and  $m_F = -1$  states of the  $F = 1$  [ $X^2\Sigma^+$  ( $\nu = 0, N = 0$ )] hyperfine state. The molecules are then subjected to an electric ( $\mathcal{E}$ ) and a magnetic ( $\mathcal{B}$ ) field. The molecules evolve in the  $\mathcal{E}$  and  $\mathcal{B}$  field for a time  $\tau$  and accumulate a phase  $\phi = \omega\tau = \phi_{\mathcal{B}} + \phi_{\mathcal{E}}$ , where the phases  $\phi_{\mathcal{B}}$  and  $\phi_{\mathcal{E}}$  due to Zeeman and eEDM interactions, respectively are given by.

$$\phi_{\mathcal{E}} = -d_e \eta E_{\text{eff}} \tau / \hbar, \quad (1.7)$$

$$\phi_{\mathcal{B}} = g \mu_{\mathcal{B}} \mathcal{B} \tau / \hbar. \quad (1.8)$$

The EDM signal is detectable through a difference in the total accumulated phase for the parallel and antiparallel orientation of the magnetic and electric fields. The superposition state is then projected back onto the ground hyperfine state  $|F, m_F\rangle = |0, 0\rangle$ ,  $X^2\Sigma^+$  ( $\nu = 0, N = 0$ ). The populations in the two hyperfine levels,  $F = 0$  and  $F = 1$  states can be detected by laser-induced fluorescence. Let the number of photons detected on exciting the molecules on the transitions from these two hyperfine levels,  $F = 0$  and  $F = 1$  of the electronic ground state  $X^2\Sigma^+$  ( $\nu = 0, N = 0$ ) to any electronic excited state be  $a_1$  and  $a_2$ , respectively. The probability of finding the molecules in the two states would be  $p_1 = \cos^2 \phi$  and  $p_2 = \sin^2 \phi$ . The photons corresponding to the number of molecules detected in the two hyperfine levels separately can be combined to define a quantity called asymmetry ( $A$ ) which would be immune to the shot-to-shot fluctuations in the number of molecules from the source,  $N_{\text{total}}$ -

$$A = \frac{a_1 - a_2}{a_1 + a_2}. \quad (1.9)$$

Ideally,  $a_1 = N_{\text{total}} \epsilon \cos^2 \phi$  and  $a_2 = N_{\text{total}} \epsilon \sin^2 \phi$  where  $\epsilon$  is the detection efficiency. So, the asymmetry is given by  $A = \cos(2\phi)$ . The experiment measures  $\phi_{\mathcal{E}}$  by measuring the resulting change in  $A$  on reversing the direction of the  $\mathcal{E}$  field, from which eEDM can be extracted.

### Statistical uncertainty

The statistical uncertainty in the measurement of  $d_e$  is given by

$$\begin{aligned} \delta d_e &= \frac{\hbar}{\eta E_{\text{eff}} \tau} \delta \phi \\ &= \frac{\hbar}{\eta E_{\text{eff}} \tau} \left| \frac{\partial \phi}{\partial A} \right| \delta A \\ &= \frac{\hbar}{\eta E_{\text{eff}} \tau} \frac{1}{2 \sin(2\phi)} \delta A. \end{aligned} \quad (1.10)$$

To minimise the uncertainty, the magnitude of the magnetic field can be chosen to set  $\phi_{\mathcal{B}} = \pi/4$ . At this phase, provided detection efficiency  $\epsilon \ll 1$ , the uncertainty in the asymmetry

is limited by the Poissonian statistics of photon counting,  $\delta A = 1/\sqrt{a}$ , where  $a = a_1 + a_2$ , as denoted in the preceding section. The shot-noise limited sensitivity can then be written as

$$\delta d_e = \frac{\hbar}{2\eta\tau E_{\text{eff}}\sqrt{a}}. \quad (1.11)$$

This equation holds for short coherence times, e.g. in a pulsed beam with the pulse repetition time longer than the coherence time. This equation implies that to maximise the sensitivity of the experiment, the coherence time and the photon count and hence the total number of molecules per pulse should be maximised.

### Common systematic errors

Common systematic uncertainties in such a precision measurement have been discussed in detail by Lamoreaux and Golub [65]. All experiments searching for EDMs can be categorised broadly into two types, confinement and beam type experiments. In confinement experiments, e.g. in the case of neutrons, the motion is constrained. In the case of beam type experiments- the particles travel through a vacuum chamber and are manipulated and detected at different points along the experimental path. The magnetic fields which depend on the applied electric field, are of primary concern. These fields induce an energy shift  $-\boldsymbol{\mu} \cdot \boldsymbol{\mathcal{B}}$  similar to the  $-d \cdot \boldsymbol{\mathcal{E}}$  shift induced by the electric field which can fake an EDM signal.

One source of systematic error is the motional magnetic field, When a particle moves through a lab electric field  $\vec{\mathcal{E}}$ , magnetic field  $\vec{\mathcal{B}}_{\text{mot}} = \vec{\mathcal{E}} \times \vec{v}/c^2$  is sensed by the particle in its rest frame. This field is in addition to a static magnetic field,  $\vec{\mathcal{B}}$  in which the spin of the particles precesses. The motional magnetic field modifies the total magnetic field sensed by the particle in the electric field free situation and this additional field flips on reversing the direction of the  $\mathcal{E}$ -field. This type of schematic affects the beam experiments more because of the spread in the particle velocities [61]. Motional magnetic fields also affect the confinement experiments despite the random particle motion (See reference [65]).

A second source of systematic error is the geometric phase. This can imitate an EDM signal when the particles move through inhomogeneous electric and magnetic fields that change when the direction of the applied electric field is reversed. Since this systematic bias depends on the motion of the individual particles, it is particularly hard to track in confinement type experiments [66].

Lastly, leakage currents between high voltage electrodes can generate a magnetic field. In the worst-case scenario, the magnetic field not only aligns with the applied electric field but its direction also reverses following the polarity changes in  $\vec{\mathcal{E}}$ . In confinement type experiments, leakage currents can be problematic as the cell walls are often used to separate the high-voltage electrodes [58]. In beam experiments, the electrode support structure can be chosen to be highly resistive and little conducive to the circulating current.

## 1.4. History of eEDM experiments

One of the earliest experimental limits on the eEDM was set by the Lamb shift [67], electron g-factor [50, 49] and by the measurement of scattering of electrons on  $\text{He}^4$  [68]. Later,



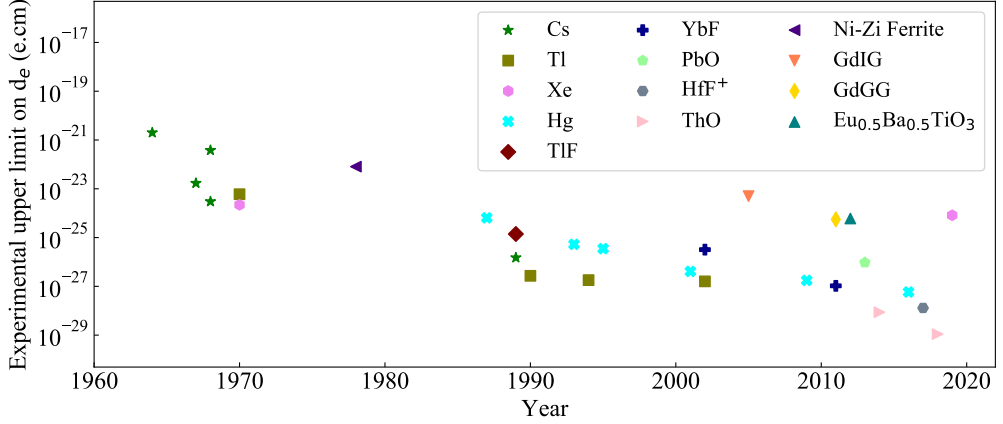


**Figure 1.1** | Review of the experimental upper limits on the electron’s electric dipole moment (90% C.L.) . The earliest measurements were done using the paramagnetic atoms, Cs [55][56][69][57][58], Tl [70][59][60][61]. Measurements on diamagnetic systems are also sensitive to eEDM, including Xe [71][72], Hg [73][74][75][76][77][78, 79]. Most recent measurements have been performed on polar diatomic molecules, TlF [80], YbF [81][82], PbO [83], HfF<sup>+</sup> [84], ThO [85][38]. Further, some measurements were also performed on solid-state systems which includes Ni-Zi Ferrite [86], GdIG [87], GdGG [88], Eu<sub>0.5</sub>Ba<sub>0.5</sub>TiO<sub>3</sub> [83].

the searches for an eEDM were performed in atomic and molecular systems due to the enhancement of the permanent electric dipole moment in composed systems. A survey of permanent electron EDM experiments over the last seven decades and the experimental limits obtained for  $d_e$  is shown in Fig. 1.1.

The lowest bound on the permanent electron EDM set by an atomic system was achieved with an atom beam of thallium. It is at  $|d_e| < 1.6 \times 10^{-27}$  e.cm [61]. The experiment reached its sensitivity limit as the systematic uncertainties could not be improved to achieve higher precision. The main systematic error was due to the motional magnetic field. To combat this issue, two pairs of counter-propagating atomic beams were used. Each beam contained thallium and sodium, and Ramsey interferometry was performed. Since sodium is a relatively light atom with a rather small EDM enhancement compared to thallium, it served as an atomic comagnetometer.

Since the past decade, there is an increased interest to use heavy molecules for the measurement of electron EDM. The limit on the permanent electron EDM has been reduced by further two orders of magnitude by using polar diatomic molecules with the lowest bound set by the ACME collaboration, which employed ThO molecules in an excited state, at  $|d_e| < 1.1 \times 10^{-29}$  e.cm [89].

The success of the molecular eEDM experiments in the past, in general, can be attributed to the development of intense molecular beam sources such as cryogenic buffer gas sources. In the past two decades, there has been immense progress in the development of techniques to

slow down molecules e.g. Stark deceleration and the extension of the laser cooling technique originally implemented on atoms to the molecules. These techniques are in preparation to be used for future eEDM searches [90, 91]. In the coming sections, we will discuss the molecular beam sources and the techniques demonstrated for slowing molecular beams briefly. We will further discuss our eEDM experiment along with the other molecular eEDM experiments.

## 1.5. Advances in the production of intense, cold and slow molecular beams

From equation 1.11, a high beam flux, a long interaction time and a long coherence time should be aimed for increasing the sensitivity of a precision experiment i.e. whatever combination gives the highest figure of merit. For a beam experiment, it would be advantageous to start from an intense source of molecules in an appropriate molecular state. For low-velocity beam, also the coherent interaction time could be longer in an interaction zone of a given length. Supersonic beam sources were used in the first generation molecular eEDM experiments. A decade earlier, cryogenically-cooled buffer gas sources were demonstrated to produce high-intensity beams with much lower longitudinal velocity [92] which can increase the interaction time. Both of these sources will be discussed in the following section. We will also briefly discuss the techniques of laser cooling, Zeeman and Stark deceleration which have been used successfully to slow and trap molecules in the past decade. The reduction of the longitudinal velocity of molecular beams from state-of-the-art sources can increase the coherent interaction time even further.

### 1.5.1. Molecular beam sources

#### Supersonic beam

The birth of the versatile supersonic beams can be owed to the theoretical predictions by A. Kantrowitz and J. Grey in 1951 [93]. The technique led to a many-fold increase in the intensity, density and decrease in the velocity spread over the effusive beams used around that time. Since the 1970s, most molecular beam experiments were done using supersonic beams. A gas expands isentropically into a vacuum through a pinhole nozzle. During the expansion process, the pressure and temperature of the molecules drop abruptly [94]. Collisions at the exit of the nozzle bring all the molecules to nearly the same temperature and velocity. Very low internal temperature could be attained as a result of which only the lowest energy states were populated. Temperatures as low as 1 mK were first achieved in the expansion of He gas through pulsed nozzles [95]. Later, molecular beams were produced by expansion in light carrier gases with rotational temperatures around  $\sim 1$  K [96, 97]. The technique could be extended to molecules that require laser ablation. The laser ablation products off a solid target were entrained in the expanding gas coming out of a nozzle to produce polar molecular beams for electron EDM searches [98, 99].

#### Cryogenic buffer gas source

A cryogenic buffer gas source was proposed and implemented [100] for atomic beams in 2009 and one year later extended to producing a molecular beam of ThO [101]. A cold cell cooled to a few 10s of Kelvin is at the heart of this technique. A continuous flow of pre-cooled buffer

gas, helium or neon, is ensured inside the cell. The molecules are ablated from a solid target. They undergo many collisions with the cold buffer gas. As a result, the temperature of the molecules reduces. The target molecule and the buffer gas then escape the cell through an exit aperture after complete thermalization of the molecules. The molecular beams produced in the cryogenic source are more intense than the ones produced in the supersonic source. The technique of buffer gas cooling has recently also been extended to polyatomic molecules such as YbOH and CaOH [102, 103]. The possibility of measuring the eEDM with YbOH is also currently being investigated [104].

### 1.5.2. Techniques for slowing and trapping the molecules

#### **Stark deceleration**

The technique was first used to slow down CO molecules in 1999 [105], in a switching type Stark decelerator (see Figure 1.2 (b)), in which 82% of the kinetic energy was removed in 63 electric field stages. The prerequisite condition for deceleration of molecule is the presence of a large chemical electric dipole moment, which acts as the effective "charge" on the neutral molecule. The working principle to decelerate molecules is explained in Figure 1.2(a)). The beams decelerated in the Stark-decelerator have a narrow velocity spread and therefore can be used for high-resolution spectroscopy. Many different species have been decelerated so far including ND<sub>3</sub> [106], OH [107], H<sub>2</sub>CO [108], NH [109], SO<sub>2</sub> [110], OD [111], LiH [112], CaF [113]. A detailed review of all the neutral molecules decelerated by this technique can be found in [114, 115]. There are, however, certain limitations to the Stark deceleration technique. It is most efficient when you start with a narrow initial velocity distribution. Since the decelerator focuses the molecules, they undergo oscillatory trajectories inside the decelerator. It was found that below a certain velocity of 100 m/s, molecules are over-focused, and they thus crash into the electrodes [116].

The technique also works in case magnetic fields are used in place of the electric fields, referred to as the Zeeman deceleration. It was first demonstrated by decelerating a beam of O<sub>2</sub> molecules in a Zeeman decelerator from 389 m/s to 83 m/s in 2008 [117]. Since then, it has been used to slow down two more molecules such as CH<sub>3</sub> [118] and He<sub>2</sub> [119]. It also suffers from the same issues as the Stark deceleration technique.

#### **Traveling-wave Stark decelerator**

The traveling-wave Stark decelerator (TWSD) is an extension of the conventional Stark decelerator. It helps to combat the issue of over-focusing as in Stark decelerator and also has comparatively larger phase-space acceptance. In a TWSD, a true three-dimensional potential well is created inside an array of ring electrodes to which high voltage is applied. The voltage on the adjacent ring electrodes is phase-shifted by  $\pi/4$ . The molecules can be decelerated by ramping down the frequency of the voltage sine-wave applied to the ring electrodes. The technique was first demonstrated on CO molecules where the molecules were decelerated from 288 m/s to 144 m/s [120]. Since then the technique has been successfully applied to decelerate NH<sub>3</sub> [121, 122] and SrF [123]. The technique is far more versatile than laser cooling, which can only be applied to molecules with closed cycles of transitions. Within our NL-eEDM collaboration, we plan to use a BaF beam decelerated in a TWSD for an eEDM measurement [90].

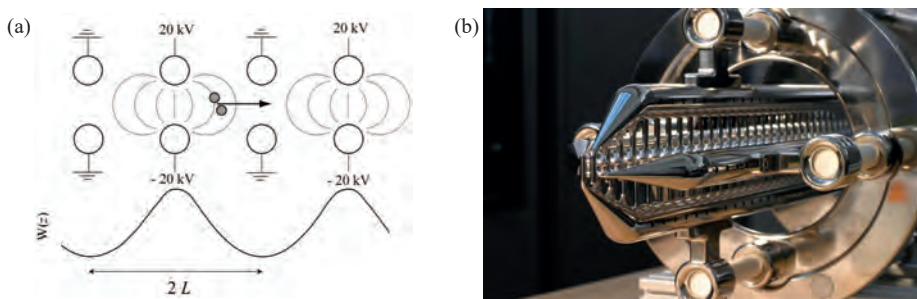


**Figure 1.2** | (a) Working principle of Stark decelerator. A region of time-varying high and low electric field is created inside a conventional Stark decelerator. A series of two-parallel electrodes oriented perpendicular to the molecular beam propagation direction alternate between being grounded and oppositely charged. This creates electric field maxima and minima. The energy levels of the molecules are shifted in the presence of an electric field with the energy for a high-field seeking (hfs) molecule decreasing and for a low-field seeking (lfs) molecule, increasing in the high electric field region. The bottom part shows the Stark shift (not to scale) for a weak-field seeking (wfs) molecule. When a wfs molecule enters an electric field region, its internal energy increases, and as a result, the kinetic energy decreases. When the wfs molecule reaches the middle between the two-charged electrodes, the fields on the adjacent electrodes are switched. The switching of the electrodes has to be synchronised with the longitudinal velocity of the molecular species inside the decelerator. The grounded pair of electrodes are charged and the charged pair of electrodes are grounded. This forces the molecule to climb another electric field hill and this trend continues. This way the longitudinal velocity of neutral molecular beams can be reduced. (b) Picture of the switching type Stark decelerator at Fritz-Haber-Institut, Berlin [124].

### Laser cooling

Laser cooling is a technique that is based on the transfer of momentum between an atom or a molecule and a laser light field. The first successful demonstration was on an atomic beam of sodium atoms in 1982 [125] in which the researchers successfully removed 40% of the initial thermal velocity of the beam after  $15 \times 10^3$  absorptions. When an atom is traveling in a direction counter-propagating to a red-detuned laser light field, it can absorb photons and it thereafter re-emits photons on average at the center transition frequency. As a result of many scattering events, the momentum of the atom is reduced, on average by the momentum that corresponds to the detuning of the laser field. The atom is excited to a higher excited state from where it decays eventually. The second photon is released in this process in a random direction. The velocity change ( $\delta v$ ) for one photon absorption depends on the mass of the atom ( $M$ ) and the wavelength ( $\lambda$ ) of the light absorbed-  $\delta v = \frac{h}{\lambda M}$ . A large number of such scattering cycles ( $\sim 10^4$ ) are needed for the deceleration to the photon recoil limit.

The laser cooling was extended to molecules almost three decades later. In 2010, the transverse laser cooling of SrF molecular beam [126] was achieved, followed by longitudinal cooling of the same molecule in 2012 [127]. Laser cooling is more complicated for molecules because

they have vibrational, rotational levels in addition to the electronic levels and therefore there are various leaks in the cooling cycle. For a molecule to be a good candidate for laser cooling, a couple of conditions should be fulfilled: 1) The lifetime of the state to which the molecule is excited should be short, which is generally true for electronic states but not for vibrational and rotational states. 2) The molecule should have favourable Frank-Condon factors, which ensures a high chance for the molecule to decay to the same vibrational state and results in a closed transition. Further, it was suggested by Stuhl *et al.* in 2008 that the decay between different rotational levels can be constrained by exciting the molecules from  $N = 1$  rotational level in the ground state to  $N = 0$  level in the excited state. Since then, the transverse laser cooling of YO [128] and longitudinal laser cooling and slowing of CaF have been demonstrated [129, 130]. The YbF molecule, which is a molecule suited for sensitive eEDM searches, has also been transversally laser cooled [91]. Recently, a new class of molecules, alkaline earth monohydride, BaH has been laser-cooled [131].

### 1.5.3. Trapping

Once molecules are slow, the next step is to trap them. In this section, we will briefly review various trapping techniques employed for molecules.

#### Magneto-optical trap

A Magneto-optical trap cools and traps atoms or molecules. The cooling is facilitated by the presence of three orthogonal pairs of red-detuned laser light. The trapping is facilitated by a quadrupole magnetic field produced by a pair of coils carrying currents in opposite directions. The principle of a MOT has been explained for  $F = 0$  to  $F = 1$  transition in Figure 1.3.

Up to date, five different molecular MOTs have been demonstrated: a MOT of SrF molecules [133, 134], two MOTs of CaF molecules [135, 136], a MOT of YO molecules [137] and very recently a 1D-MOT of a polyatomic molecule, CaOH. [103].

#### Conservative traps

In a MOT, the molecules continuously scatter photons. It is necessary for many applications, that involve quantum control, to transfer the molecules into a conservative trap. These traps have long lifetimes and unlike a MOT, the internal state of the molecule in a conservative trap can also be preserved.

① Magnetic trap: This trap uses the force arising from an interaction between the magnetic moment of an atom/molecule and an external inhomogeneous magnetic field to confine them. This force was first used by Otto Stern and Walter Gerlach in their famous experiment of 1924 [138, 139]. This concept was refined and put into use for the construction of hexapole lenses for focussing in the 1950s. The design of the magnetic quadrupole trap consisting of two identical coils carrying opposite current, with a single field minimum is attributed to W. Paul [140]. The first molecule which was loaded into a magnetic trap is calcium hydride [141]. A total of  $1 \times 10^8$  molecules were trapped at 400(50) mK with a lifetime of 2 seconds. Since then, OH [142], NH [143] and CaF [144] molecules have been magnetically trapped at a relatively low temperature of 30 mK. Recently, ultracold SrF [145] and CaF [146] have



inversely proportional to the  $I/(\delta)^2$  against the dipole force which is proportional to  $I/\delta$ . The scattering rate should be low to prevent the heating of the molecule. An optical dipole trap for CaF molecules has recently been demonstrated [147].

③ Electric trap: Molecules with large induced (chemical) dipole moments can be trapped in electric traps due to the interaction of their induced dipole moment with an inhomogeneous electric field. With appropriately shaped and placed electrodes, a quadrupole electric field can be created with a field-free center between them. Molecules in certain energy levels (low-field seeking states) prefer to be at the field minimum and hence can be trapped. Such a trap was first proposed for neutral molecules in 1986 [148] and demonstrated on NH<sub>3</sub> molecules in 2000 [106]. Since then, electrostatic traps of NaCs [149] and H<sub>2</sub> [150] in Rydberg states have been demonstrated. A box-like electrostatic trap has also been used to store CH<sub>3</sub>F [151] where the field is rather uniform in the largest part of the trap volume and with a very steep electric field gradient at the edges. We have recently brought SrF molecules to a standstill in the electric field traps inside the TWSD (see Chapter-6).

## 1.6. eEDM experiments using polar molecules

The choice of the molecule for the eEDM measurement is made with the aim to minimise the statistical uncertainty (see Equation 1.11). Molecules with a large EDM enhancement are often preferentially chosen. Most of the molecules such as YbF, ThO, HfF<sup>+</sup>, ThF<sup>+</sup>, BaF presently employed in eEDM search experiments have effective electric fields of a few 10s of GV/cm in the presence of an external laboratory electric field (See Table 1.1). Further, the construction of a reliable high-intensity beam source for the molecules also should be possible. Some work also needs to be done to do the spectroscopy to determine the energy constants, lifetimes and Frank Condon factors as most of these molecules are unstudied. Therefore it is an added advantage if most of the relevant transitions in the molecules can be addressed by convenient diode lasers. We will discuss briefly three molecular eEDM experiments with YbF, ThO and HfF<sup>+</sup>. None of the molecules is a perfect choice, but each of them brings different advantages to the table.

The ACME experiment uses a cryogenic buffer gas source to produce a beam of ThO molecules traveling at a velocity of 200 m/s. After coming out of the exit aperture, the molecules are rotationally cooled by optically pumping the population in the first three excited rotational states to the ground rotational state. After molecules are rotationally cooled, they enter the interaction zone, which has various  $\mu$ -metal shielding layers to precisely control the magnetic field. The molecules pass through a pair of electric field plates charged to  $\pm 50$  V and separated by 4.5 cm. The electric field plates are transparent for visible light and hence enable laser beams to pass through them. The molecules in the ground state are pumped to the state H  $^3\Delta_1$ , from X ( $J=0$ ) via the intermediate state C ( $J=0, P=-1$ ) using STImulated Roman Adiabatic Passage (STIRAP) technique. A laser field polarises the spin of the outer electron to be perpendicular to the electric field. The spin of the electron precesses due to the interaction with the electric and the magnetic fields. After an interaction time of  $\sim 1$  ms (limited by the lifetime of the  $^3\Delta_1$  state), laser light reads out the precession



Molecule	$E_{\text{eff(max)}}$
ThO	84 GV/cm [155]
HfF <sup>+</sup>	24 GV/cm [156]
YbF	-26 GV/cm [157]
BaF	-6 GV/cm [158, 159]
ThF <sup>+</sup>	37 GV/cm [160]

**Table 1.1** | Effective electric fields for molecules used for eEDM experiments.

angle, which is proportional to the  $d_e$ . The  $d_e$  value is usually obtained by reversing the value of the electric field relative to the magnetic field direction and then measuring the difference in the precession phase. In ThO molecules, the EDM state has closely spaced  $\Omega$ -doublets. The EDM-induced shift can be reversed spectroscopically by making a measurement using pairs of states in different components of the doublet. This is an effective way to reject the systematic effects due to geometric phases. In addition to the  $\Omega$ -doublets, the EDM state  $^3\Delta_1$  has a very small magnetic moment [152], which helps in suppressing the systematic errors due to the residual  $\mathcal{B}$  field. The most recent measurement is limited by technical noise. For their third generation measurements, a new thermochemical source has been developed which is based on the reaction  $\text{Th} + \text{ThO}_2 \rightarrow 2\text{ThO}$  [153]. This is expected to improve the sensitivity by one order of magnitude [153].

A second experiment to search for an eEDM uses HfF<sup>+</sup> molecules [84]. The experiment has placed a limit on the eEDM of  $|d_e| < 1.3 \times 10^{-28}$  e.cm (90% confidence). Neutral HfF molecules are produced in a supersonic source and then ionised using UV light in the  $^1\Sigma^+$  ( $\nu = 0$ ) state. The molecules are loaded into an rf-trap and polarised using a rotating electric bias field. The molecules are then prepared in a single magnetic sublevel of the  $^3\Delta_1$  ( $\nu = 0, J = 1$ ) state using stimulated Raman passage [154]. The Ramsey sequence measures the EDM shift between  $M_F = \pm 3/2$  levels in  $^3\Delta_1$  ( $\nu = 0, J = 1$ ). The ions are detected by photodissociating then into Hf<sup>+</sup> and F.

A third eEDM experiment uses YbF molecules. YbF molecule has an effective electric field of 26 GV/cm. They obtained an upper limit on the value of electron EDM at  $|d_e| < 10.5 \times 10^{-28}$  e.cm (90% confidence) back in 2011 [82]. The detection efficiency and the number of molecules produced in the source have each been increased by one order of magnitude since then [161]. A pulsed supersonic beam of YbF molecules traveling at a speed of 600 m/s passes through an electric and magnetic field. The molecules are optically pumped using optical, rf and microwave fields from the higher rotational ( $N = 1, 2$ ) and hyperfine states ( $F = 1$ ), to ground electronic state  $X^2\Sigma^+$  ( $\nu = 0, N = 0, F = 0$ ) state. The molecules further enter a region of uniform electric and magnetic fields,  $\mathcal{E} = \mathcal{E}\hat{z}$  and  $\mathcal{B} = \mathcal{B}\hat{z}$ . A  $\pi$  pulse of rf magnetic field, polarised along the x-axis, transfers the molecules into an equal superposition of  $m_F = +1$  and  $m_F = -1$  states in  $F = 1$  hyperfine level in  $N = 0$  rotational state. The molecules then precess in the  $\mathcal{E}$  and  $\mathcal{B}$  field for  $\sim 1$  ms and another rf  $\pi$ -pulse then projects back any remaining population in the original superposition state back to the  $F = 0$  hyperfine level. A non-zero eEDM will shift the energies of the  $m_F = \pm 1$  states in

$F = 1$  hyperfine level by  $-d_e m_F E_{\text{eff}}$  in addition to the linear Zeeman interaction shifting the levels by  $g\mu_B m_F \mathcal{B}$ .

Unlike ThO and HfF<sup>+</sup> experiments, the state in YbF used for the eEDM measurement,  $X^2\Sigma^+$  ( $\nu = 0, N = 0$ ) is the ground electronic state. Therefore, there is no fundamental limit on the coherent interaction time. YbF can also be produced in a cryogenically-cooled buffer gas source and laser-cooled [91], the techniques which could be used for future eEDM searches with YbF for a higher figure of merit [162]. The  $X^2\Sigma^+$  ( $\nu = 0, N = 0$ ) state in YbF, however, does not have  $\Omega$  doublet, so it suffers from some systematic effects which are eliminated in the eEDM experiments with ThO and HfF<sup>+</sup> molecules.

## 1.7. The NL-eEDM experiment

Within our collaboration, we plan to measure the eEDM using BaF molecules. The planned experimental setup is shown in Figure 1.4. We will produce the BaF molecules in a cryogenic buffer gas beam source. We plan to decelerate the molecules exiting the cryogenic source in the ground electronic state  $X^2\Sigma^+$  ( $\nu = 0, N = 2$ ) in a TWSD and then transversally laser-cool the molecules after they exit the TWSD. The state preparation, phase evolution of the state and the signal readout will take place in the interaction zone.

We have built two cryogenic sources (similar design) and one supersonic source. One cryogenic source is based at VU, Amsterdam and is currently being optimised to increase the intensity of the BaF molecular beam. The second cryogenic source which is used to produce SrF molecules has been connected to the TWSD. We have started with the deceleration of SrF beam for practical reasons, which has a very similar energy level structure and Stark curve to BaF molecules. In the future, the second cryogenic source will also be used to produce BaF molecules and molecules will be decelerated in a TWSD. The supersonic source has been connected to the interaction zone for a first eEDM search in BaF.

(A) Cryogenic source: The BaF (and SrF) molecules are produced in a pulsed cryogenic beam source with a repetition rate of 10 Hz. The cell design of our source is similar to the one reported in [163]. The source creates a beam with a forward velocity of 190 m/s, with some  $10^9$  molecules in a pulse of 5-10 ms length and with a rotational temperature of 11 K, a longitudinal velocity spread of 100 m/s and a transverse velocity spread of 60 m/s.

(B) Supersonic source: The BaF (and SrF) molecules are produced in a pulsed supersonic beam source with a repetition rate of 10 Hz. The source creates a beam with a forward velocity of  $\sim 590$  m/s, with  $\sim 10^6$  molecules in a pulse of 5-10 ms duration and with a rotational temperature of 3 K and a longitudinal velocity spread of 70 m/s.

(C) Stark deceleration: To reduce the forward velocity of the cryogenic beam of molecules from 190 m/s longitudinal velocity out of the cryogenic source to 30 m/s longitudinal velocity, we will use a 4.5 m long Stark decelerator. The decelerator has been used to decelerate supersonic beams of SrF in our group in the past [123]. The cryogenic beams emit a longer

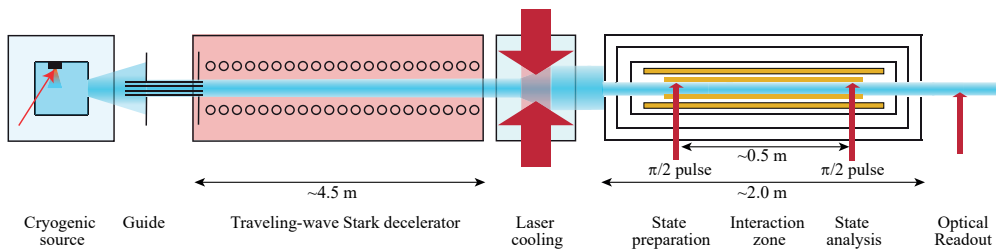


**Figure 1.4** | Schematic overview of the planned experimental setup. The molecular beam of BaF travels from left to right. A beam of BaF molecules with a velocity of 190 m/s created in the cryogenic source will subsequently be decelerated to 30 m/s in a TWSD. A laser cooling section will reduce the transverse velocity spread of the beam, to prevent the beam from spreading out during the 15 ms transit through the 0.5 m interaction zone. For a horizontal beam at such low velocities, the gravitational fall needs some addressing while launching the beam into the interaction zone. In the magnetically shielded interaction zone, the molecules are prepared in a superposition of the hyperfine substates,  $X^2\Sigma^+$  ( $\nu = 0, N = 0, F = 1, m_F = \pm 1$ ), which builds up a phase difference in the presence of an electric and a magnetic field. For the state analysis, the superposition state is projected back onto the  $X^2\Sigma^+$  ( $\nu = 0, N = 0, F = 0, m_F = 0$ ). Readout of the state will be done via laser-induced fluorescence detection.

molecular pulse in comparison to the pulse from a supersonic source. As a result of the longer pulse, multiple co-moving electric field minima are filled (see Chapter 5 and Chapter 6), which have to be all decelerated to the same final velocity. The fraction of molecules accepted by the decelerator depends on the deceleration strength, the applied voltage and the Stark shift of the molecular state of interest. The applied voltage determines the limit on the longitudinal and transverse velocity of the molecules which can be accepted into the decelerator. We have decelerated SrF molecules in their electronic and vibrational ground state and  $N = 1$  rotational state for a sinusoidal voltage amplitude of 5 kV applied to the rings. We are currently in the process of voltage upgrade to 10 kV to facilitate the deceleration of BaF molecules in  $N = 2$  rotational state which has higher Stark shifts.

At a voltage amplitude of 10 kV, the BaF molecules in the  $N = 2$  rotational state of the ground state in BaF will be accepted by the decelerator if their longitudinal velocity is within  $\pm 8.5 \text{ ms}^{-1}$  of the set velocity and a transverse velocity up to  $\pm 5 \text{ ms}^{-1}$ . From numerical trajectory simulations, the beam exiting out of the decelerator should contain  $2 \times 10^6$  molecules per pulse with a longitudinal and transverse velocity spread of  $\pm 6 \text{ ms}^{-1}$  and  $\pm 5 \text{ ms}^{-1}$  respectively<sup>†</sup>.

(D) Interaction/ Measurement zone: We have designed a 0.5 m long interaction zone which is currently being set up. The assembling of the setup has started and spectroscopy for preparation of the state best suited for an eEDM search is also on way. More details on

<sup>†</sup>More details can be found in Eur. Phys. J. D. 72, 197 (2018) [90]

the design of the interaction zone can be found in [90]. The molecules will be prepared in a superposition state of two magnetic sublevels  $m_F = +1$  and  $m_F = -1$  in the  $F = 1$  hyperfine level of the  $N = 0$  rotational state of the electronic ground state  $X^2\Sigma^+$  ( $v = 0$ ). The superposition state will acquire a phase advance while interacting with the external electric and magnetic fields. The eEDM signal will be detected through a phase difference in the total accumulated phase for parallel and anti-parallel orientation of the magnetic and electric fields. After the spin precession, the superposition state is projected back onto an energy eigenstate. This way the total phase advance in the interaction zone can be determined.

In the future, we plan to insert a 0.5 m length guide with a quadrupole lens system between the cryogenic source and the decelerator to match the transverse velocity distribution of the molecular beam with the phase space acceptance at the entrance of the decelerator [122, 164]. Further, the slow beam coming out of the decelerator diverges due to the residual transverse velocity. To ensure that the maximum number of molecules passes through the half-a-meter long interaction zone, transverse laser cooling will be employed. The laser cooling section is currently in the design process. The theoretical investigations of the ground and lowest excited states of BaF using the calculated molecular properties, Franck Condon factors for the  $X^2\Sigma^+$  and  $A^2\Pi_{1/2}$  transition in BaF have been determined. As a result, the transition  $A^2\Pi_{1/2}(v = 0) \leftarrow X^2\Sigma^+(v = 0, N = 1)$  has been identified to be suitable for laser cooling of BaF [165]. Within the experimental program, we measured the lifetime of the  $A^2\Pi_{1/2}(v = 0)$  and  $A^2\Pi_{3/2}(v = 0)$  states in BaF, which govern the possibility of laser cooling of this molecular system. This transition has previously been used successfully for the laser cooling of SrF molecules. More details on the planned laser cooling section can be found in [90].

With the long coherent interaction times obtainable in such a cold beam of BaF, we aim to achieve a sensitivity of  $5 \times 10^{-30}$  e·cm in the eEDM measurement [90].

## 1.8. Outline of the thesis

In this thesis, we describe the development of several key components for an experiment to search for an eEDM. The individual chapters describe crucial steps on the path from a conceptual design towards a precision experiment.

**Chapter 2** provides an introduction to molecule structure, notation and the field-matter interactions which are important for the remainder of the thesis.

**Chapter 3** describes the construction of a supersonic beam source for BaF and SrF molecules.

**Chapter 4** covers an experiment to measure the lifetimes of the  $A^2\Pi_{1/2}$  and  $A^2\Pi_{3/2}$  excited electronic states in BaF. As described in the preceding section, the transition between the ground state  $X^2\Sigma^+$  ( $v = 0, N = 1$ ) to this excited state,  $A^2\Pi_{1/2}(v = 0, J = 1/2)$  is foreseen as the main laser cooling mechanism in the upcoming eEDM experiment.

**Chapter 5** reports the deceleration results for a cryogenic beam of SrF molecules in the 4 m long TWSD. With a molecular beam from a cryogenic source, very low longitudinal velocities could be achieved. Only supersonic beams have been decelerated in a TWSD before.

**Chapter 6** presents the deceleration results for a beam of SrF molecules from a cryogenic

---

source in a decelerator of 4.5 m length. We report here on the achieved confinement of decelerated molecules in the electric field minima formed inside the ring electrodes of the decelerator.



# 2

## Molecular structure and theory

Those who are not shocked when they first come across quantum theory cannot possibly have understood it.-Niels Bohr

The understanding of the molecular structure of SrF and BaF is important for the success of experiments in which the production and detection of beams of these molecules as well as the deceleration and trapping of these molecules are addressed. A general form of the molecular Hamiltonian is specified followed by the expressions of energy contributions and the term symbols of the associated molecular states. Diatomic molecules, in addition to the electronic energy levels, have vibrational and rotational degrees of freedom due to the molecular vibrations and rotation of the molecule perpendicular to the internuclear axis, respectively. We will further describe the molecule-field interactions which are relevant for the results presented in this thesis. The splitting of the molecular energy states in the presence of electric and magnetic fields is discussed. These molecular properties are at the base of the working principle of the Stark decelerator in the subsequent chapters.

### 2.1. Energy structure of molecules

Molecules are composed of nuclei and electrons and therefore have electronic energy levels. Because of having more than one nucleus, molecules have in addition to electronic levels, vibrational and rotational degrees of freedom associated with the motion of the nuclei. In the Born-Oppenheimer (BO) approximation, these three degrees of freedom are treated independently [166]. In the BO approximation, the velocities of the electrons are many orders of magnitude higher than those of nuclei and as a result, the electron orbits many times around the nuclei before the nuclei move significantly. When the contribution of the nuclei to the Hamiltonian is expanded into a power series of  $(m_e/\mu)^{1/4}$ , where  $m_e$  is the mass of the electron and  $\mu$  is the reduced mass of the two nuclei, the vibrations correspond to the



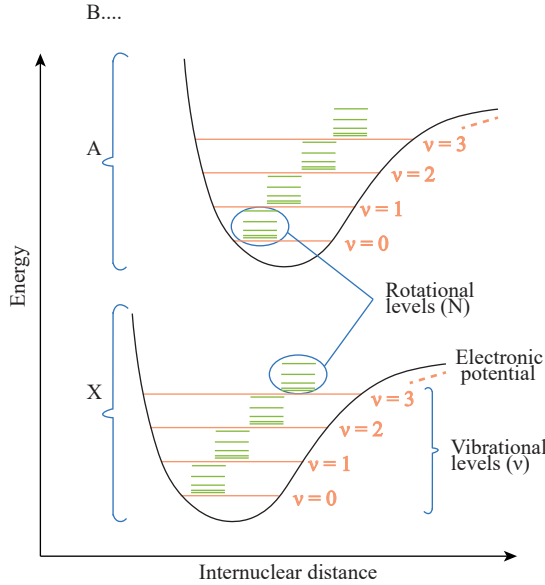


**Figure 2.1** | Schematic depicting the typical energy level structure for a diatomic molecule.

2nd order, rotations to 4th order and the 1st and 3rd order vanish. The three degrees of motion are therefore decoupled to zeroth order. Figure 2.1 depicts the energy level structure of a typical diatomic molecule. All three motions determine the properties and spectra of diatomic molecules. In the case of higher-order coupling, the terms corresponding to these effects can be treated perturbatively or evaluated exactly for the state of interest. The energy Hamiltonian for our diatomic molecules is given to good approximation by [167]

$$H = H_e + H_{vib} + H_{rot} + H_{SO} + H_{SR} + H_{HFS} + H_{\lambda_d}, \quad (2.1)$$

where  $H_e$ ,  $H_{vib}$ ,  $H_{rot}$ ,  $H_{SO}$ ,  $H_{SR}$ ,  $H_{HFS}$  and  $H_{\lambda_d}$  correspond to the electronic, vibrational, rotational, spin-orbit, spin-rotation, hyperfine and  $\lambda$  doubling components of the Hamiltonian.

## 2.2. Electronic energy level structure

The electronic energy level structure of diatomic molecules is similar to that of an atom. We address the total electronic orbital angular momentum by  $\mathbf{L}$ , the total electronic spin by  $\mathbf{S}$  and with those the total electronic angular momentum by  $\mathbf{J} = \mathbf{L} + \mathbf{S}$ .  $\mathbf{L}$  and  $\mathbf{S}$  are vectors which commute with the Hamiltonian and are for most atoms, in good approximation, good quantum numbers. Unlike atoms, the spherical symmetry of the internal electric field in the molecules is broken. Though, the diatomic molecules have axial symmetry along the internuclear axis. The projection of  $\mathbf{L}$ ,  $\mathbf{S}$ ,  $\mathbf{J}$  on the internuclear axis is given by  $\Lambda$ ,  $\Sigma$  and  $\Omega$  respectively, where  $\Omega = \Lambda + \Sigma$ . The sign of  $\Lambda$  can be positive or negative depending

on whether the orbital angular momentum is clockwise or anti-clockwise, respectively. In addition, there is nuclear spin angular momentum,  $\mathbf{I}$  which couples with  $\mathbf{J}$  to produce the total angular momentum  $\mathbf{F} = \mathbf{I} + \mathbf{J}$ . These different angular momenta can couple in the diatomic molecules in various ways, given by the Hund's coupling cases (see Table 2.1). For different coupling approximations, only certain quantities can be considered to be conserved and are defined as good quantum numbers. In general, the energy levels are labelled with their term symbol given as

$$^{2S+1}\Lambda_{\Omega}^{\pm}, \quad (2.2)$$

where  $+/-$  is the reflection symmetry of the electronic state along an arbitrary plane containing the internuclear axis. There are different symbols for different values of  $\Lambda$  given by

$\Lambda$ value	0	1	2	3
Symbol	$\Sigma$	$\Pi$	$\Delta$	$\Phi$

The electronic energy levels are denoted in addition by letters before the term symbol, with X denoting the ground state and the excited electronic states with the same multiplicity as the ground state denoted by (A, B, C....) and the excited state with different multiplicity than the ground state denoted by (a, b, c....). The spacing between the different electronic states are of order 100 THz and the energy of an electronic level is denoted by  $T_e$ .

## 2.3. Vibrational energy levels

The vibrational motion of the two nuclei around the equilibrium distance is quantised and specified by the vibrational quantum number  $\nu$ . The vibrational energy can be expressed as power series

$$E_{\nu} = \omega_e(\nu + 1/2) + \omega_e x_e(\nu + 1/2)^2 + \omega_e y_e(\nu + 1/2)^3 + \dots, \quad (2.3)$$

where  $\omega_e = (k/\mu)^{1/2}$  is the vibrational constant,  $\omega_e x_e$  and  $\omega_e y_e$  are the anharmonic constants of decreasing size. They incorporate the distortion of the vibrational potential from a harmonic potential. The vibrational levels are equidistant for small values of  $\nu$ . For a large value of  $\nu$ , levels are closely spaced and if the energy exceeds the depth of the well, the molecule dissociates. Hence, there is only a finite number of vibrational levels. The constants  $\omega_e$ ,  $\omega_e x_e$  and  $\omega_e y_e$  differ for different electronic energy levels. The spacing between different vibrational energy levels is tens of THz.

## 2.4. Rotational energy levels

The rotational energy levels for diatomic molecules correspond to the energy arising from the rotation of the two nuclei around the molecule's center of inertia. This motion is also quantised and is represented by the quantum number  $N$ . The rotational energy within a given vibrational energy level can be expanded in the following power series

$$E_R = B_e N(N+1) - D_e N^2(N+1)^2 + \dots, \quad (2.4)$$

Angular momentum	Operator	Hund's case (a)	Hund's case (b)
Electronic orbital angular momentum	$\mathbf{L}$		
Electronic spin	$\mathbf{S}$		
Nuclear spin	$\mathbf{I}$		
Nuclei rotational angular momentum	$\mathbf{N}$		
Total angular momentum excluding spin	$\mathbf{R}$		$\mathbf{L}+\mathbf{N}$
Total angular momentum	$\mathbf{J}$	$\mathbf{N}+\mathbf{L}+\mathbf{S}$	$\mathbf{R}+\mathbf{S}$
Grand total angular momentum	$\mathbf{F}$	$\mathbf{J}+\mathbf{I}$	$\mathbf{J}+\mathbf{I}$

**Table 2.1** | Angular momentum relevant to SrF and BaF molecules.

where  $B_e = \hbar^2/2I$  is the rotational constant and  $D_e$  is the centrifugal distortion constant. The moment of inertia changes with the vibrational motion, which in turn changes the rotational constant. Hence the rotational and vibrational motion is interconnected.

## 2.5. Coupling of angular momentum: Hund's cases

The various sources of angular momentum can couple in different ways. The choice of (approximately) good quantum numbers for a molecular state can be classified into Hund's coupling cases. Hund's cases are perturbative approaches with an accuracy of order kHz. Searches for permanent EDMs require energy precision of order nHz. This thesis presents the work on the preparation of the slow and intense molecular beams which will be used for an electron EDM experiment in the near future. Hence, for the scope of the results presented in this thesis, Hund's cases are still a good approximation. For the two molecules, SrF and BaF discussed in this thesis, the ground state is given by Hund's case (b) and the first (and second) excited electronic state is defined by the Hund's case (a) [168, 169]. Their couplings are illustrated in Figure 2.2. In a semi-classical picture, there are five different angular momenta involved in the description, which are  $\mathbf{L}$ ,  $\mathbf{S}$ ,  $\mathbf{J}$ ,  $\mathbf{N}$ ,  $\mathbf{R}$ . As already specified,  $\mathbf{L}$ ,  $\mathbf{S}$  and  $\mathbf{J}$  are the electronic orbital, spin and total angular momentum.  $\mathbf{R}$  and  $\mathbf{N}$  are the total angular momentum excluding spin,  $\mathbf{R} = \mathbf{J} - \mathbf{S}$  and the rotational angular momentum,  $\mathbf{N} = \mathbf{R} - \mathbf{L}$ , respectively.

Hund's case (a)  $\mathbf{L}$  couples strongly with the internuclear axis by electrostatic forces and the electron spin  $\mathbf{S}$  couples to  $\mathbf{L}$  via the spin-orbit coupling. The components of  $\mathbf{L}$  and  $\mathbf{S}$  along the internuclear axis add to form  $\mathbf{\Omega}$ , which couples with  $\mathbf{N}$  to form resulting total angular momentum  $\mathbf{J}$ . The precession of  $\mathbf{L}$  and  $\mathbf{S}$  is much faster than the rotation of  $\mathbf{\Omega}$  and  $\mathbf{N}$  about  $\mathbf{J}$ . Therefore, the good quantum numbers for this Hund's case are  $\Lambda$ ,  $\mathbf{S}$ ,  $\Sigma$ ,  $\mathbf{J}$  and  $\mathbf{\Omega}$ .

Hund's case (b)  $\mathbf{L}$  precesses rapidly about the internuclear axis with a well-defined component,  $\Lambda$ .  $\Lambda$  couples with  $\mathbf{N}$  to form  $\mathbf{R}$  ( $\mathbf{R} = \Lambda + \mathbf{N}$ ).  $\mathbf{R}$  couples with  $\mathbf{S}$  to form the total angular momentum  $\mathbf{J} = \mathbf{R} + \mathbf{S}$ . The good quantum numbers are  $\Lambda$ ,  $\mathbf{R}$ ,  $\mathbf{S}$ ,  $\mathbf{J}$ . Hund's

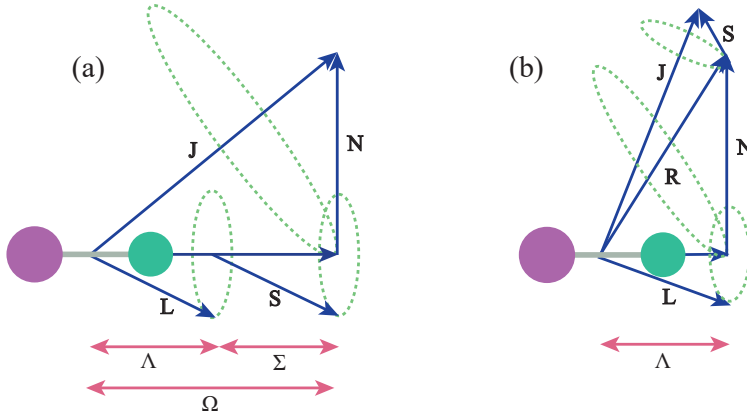


**Figure 2.2** | Illustration of Hund's angular momentum coupling cases (a) and (b).

case (b) is most appropriate when  $\Lambda = 0$  and  $S \neq 0$  because here,  $S$  is not coupled to the internuclear axis and spin-orbit coupling vanishes. Consequently,  $\Omega$  is not defined.

## 2.6. Spin-orbit and spin-rotation, hyperfine structure and $\lambda$ -doubling terms

The ground electronic state in the case of BaF and SrF is  $^2\Sigma$ , an open shell state with spin  $S = 1/2$  and the orbital quantum number  $L = 0$ . The first excited electronic state of SrF is  $^2\Pi$  with spin  $S = 1/2$  and the orbital quantum number  $L = 1$ . However, the first excited state in BaF is  $^2\Delta$  and it is neglected here. The second excited state of BaF,  $^2\Pi$ , which is the same as the first excited electronic state of SrF is discussed. The nuclear spin in the case of SrF and BaF is  $I = 1/2$  due to  $^{19}\text{F}$  nuclear spin. The nuclear spin of  $^{138}\text{Ba}$  and  $^{88}\text{Sr}$  is zero. Molecules, therefore, exhibit additional energy level structure due to coupling of  $I$  and  $S$  quantum number and also to other rotational,  $N$  and orbital quantum number,  $L$ . In  $^2\Sigma$  state,  $L = 0$  and hence  $\lambda = 0$ , so the spin-orbit and lambda-doubling terms are zero, with the dominant contributions from spin-rotation and hyperfine interactions while the energy level structure of  $^2\Pi$  has a dominant contribution from spin-orbit and lambda-doubling terms.

### 2.6.1. Spin-rotation and hyperfine structure in $^2\Sigma$ state

The magnetic moment due to the electron spin ( $S = 1/2$ ,  $\lambda = 0$ ) interacts with the magnetic moment due to the molecular rotation ( $N$ ). The interaction is represented by the term

$$H_{SR} = \gamma_{vN} \mathbf{S} \cdot \mathbf{N}, \quad (2.5)$$

where  $\gamma_{vN}$  is the spin-rotation coupling constant. As a result, the rotational levels in a single vibrational band ( $v$ ) splits into a spin-doublet. Each rotational level in a given vibrational level of  $^2\Sigma$  splits into the spin-doublet  $J = |N \pm S| = |N + 1/2|$  and  $|N - 1/2|$ , with the

corresponding energies

$$\begin{aligned} E_{(N-1/2)} &= B_{\nu}N(N+1) - (1/2)\gamma_{\nu N}(N+1) \\ E_{(N+1/2)} &= B_{\nu}N(N+1) + (1/2)\gamma_{\nu N}N. \end{aligned} \quad (2.6)$$

The first term in both equations is the result of the rotational magnetic moment in the direction of  $\mathbf{N}$ , as already discussed in section 2.4. The second term originates from the orbital angular momentum which precesses at right angles to the internuclear axis. The expectation value of  $\mathbf{L}$  on the internuclear axis is zero, but the spin-orbit coupling still mixes the ground  $\Sigma$  state with  $\Pi$  states, adding additional non-zero magnetic moment in the direction of  $\mathbf{N}$ .

Another important interaction for  $^2\Sigma$  state in a molecule arises from the existence of a nuclear spin. The interaction between the electronic angular momentum and nuclear spin magnetic moment leads to further splitting of states. The interactions split  $\mathbf{J}$  into hyperfine levels  $\mathbf{F}$ , defined as  $\mathbf{F} = \mathbf{J} + \mathbf{I}$ . The hyperfine-energy contribution arises from hyperfine structure Hamiltonian part

$$H_{\text{HFS}} = b_{\nu N} \mathbf{S} \cdot \mathbf{I} + c_{\nu N} (\mathbf{I} \cdot \hat{\mathbf{z}})(\mathbf{S} \cdot \hat{\mathbf{z}}) + C_{1\nu N} \mathbf{I} \cdot \mathbf{N}, \quad (2.7)$$

where  $b_{\nu N}$  is the hyperfine constant,  $c_{\nu N}$  is the dipole-dipole constant and  $C_{1\nu N}$  is the nuclear spin rotation constant. The constant  $C_{1\nu N}$  is negligibly small, and included here only for the sake of completeness. The constants  $b_{\nu N}$  and  $c_{\nu N}$  were defined by Frosch and Foley [170]. The Fermi-contact constant,  $b_{F\nu N}$  is given by [167]

$$b_{F\nu N} = \frac{2}{3} g_s \mu_B g_N \mu_N \mu_o \int \psi^2(r) \delta(r) dr, \quad (2.8)$$

where  $\mu_0 = (\epsilon_0 c^2)^{-1}$ ,  $\mu_B$  is Bohr magneton,  $\mu_N$  is the nuclear magnetic moment,  $g_s$  and  $g_N$  are electron spin  $g$ -factor and nuclear  $g$ -factor, respectively. The Fermi-contact constant is related to the Frosch and Foley parameters by

$$b_{F\nu N} = b_{\nu N} + c_{\nu N}/3, \quad (2.9)$$

where the subscripts  $\nu$  and  $N$  on the parameters indicate that they are functions of these quantum numbers and therefore dependent on the internuclear distance. The Dirac delta function in the expression of  $b_{F\nu N}$  ensures that the unpaired electron has a finite probability around the nucleus. Each resultant quantum state,  $\mathbf{F} = \mathbf{I} + \mathbf{S}$  is composed of  $2F + 1$  projection sublevels labelled  $m_F$ .

### 2.6.2. Spin-orbit and lambda-doubling structure in $^2\Pi$ state

The  $^2\Pi$  state has both electronic orbital ( $\mathbf{L}$ ) and spin ( $\mathbf{S}$ ) angular momentum with well-defined components,  $\Lambda$  and  $\Sigma$  along the internuclear axis. The spin-orbit interaction is given by the Hamiltonian term

$$H_{SO} = A \mathbf{L} \cdot \mathbf{S}, \quad (2.10)$$

where  $A$  is the spin-orbit coupling constant. The spin-orbit interaction term splits the electronic structure into a multiplet of  $2S+1$  components. The associated energy term is given to a first approximation by [171]

$$E_{SO} = A\Sigma\Lambda. \quad (2.11)$$

For  ${}^2\Pi_{1/2}$  state,  $L=1$  and  $S=1/2$ , therefore  $\Lambda=0, \pm 1$ ,  $\Sigma=\pm 1/2$ , so the  $\Omega=\Lambda+\Sigma$  takes values  $-1/2, 1/2, -3/2, +3/2$ . The two values of  $|\Omega|=1/2$  and  $3/2$  correspond to two fine structure states  ${}^2\Pi_{1/2}$  and  ${}^2\Pi_{3/2}$ , with energies  $A/2$  and  $-A/2$  respectively.

Lambda doubling is due to the interaction between the rotation of nuclei and electron orbital angular momentum. This contribution becomes dominant for large rotation speeds and produces a splitting into two components for each  $J$  value in states with  $\lambda \neq 0$ . Generally, the magnitude of splitting is only a fraction of  $\text{cm}^{-1}$ . For large  $J$  values and small  $\Omega$  value, it reaches a few  $\text{cm}^{-1}$ . The contribution of  $\lambda$  doubling to the energy Hamiltonian for  ${}^2\Pi$  state is given by [172]-

$$H_{\lambda_d} = -\frac{1}{2}(p+q)(S_+^2 + S_-^2) - \frac{1}{2}(p+2q)(J_+S_+ + J_-S_-) + \frac{1}{2}q(J_+^2 + J_-^2), \quad (2.12)$$

where  $p$  and  $q$  are  $\lambda$ -doubling parameters and  $S_{+(-)}^2$  is the spin raising (lowering) operator and  $J_{+(-)}$  is the raising (lowering) operator of the total angular momentum. For the case of a  $\Pi$  state, which is close to one particular  $\Sigma$  state and far away from other  $\Sigma$  state and when both  $\Pi$  and  $\Sigma$  state have same angular momentum  $L$  which precesses under two different angles to the internuclear axis in the two states, called the case of pure precession, the  $\lambda$ -doubling parameters  $p$  and  $q$  are given as [171]

$$p = \frac{2AB_e l(l+1)}{\Delta E} \quad (2.13)$$

$$q = \frac{2B_e^2 l(l+1)}{\Delta E}, \quad (2.14)$$

where  $\Delta E$  is the separation of the  $\Pi$  state from the  $\Sigma$  state,  $A$  and  $B_e$  is the fine-structure constant and the rotational constant of  ${}^2\Pi$  state, respectively. For the  ${}^2\Pi$  state conforming with Hund's case (a) coupling, the  $\Lambda$ -doublet splitting is given by [172, 173]

$$\Delta E_{\Lambda_d} = \begin{cases} (p+2q)(J+1/2) & J=1/2 \\ \frac{2B_e q}{A-2B_e}(J-1/2)(J+1/2)(J+3/2) & J=3/2. \end{cases} \quad (2.15)$$

Table 2.2 and Table 2.3 summarises the experimentally extracted values of the main spectroscopic constants of SrF and BaF respectively in the ground electronic state  ${}^2\Sigma^+$  and excited electronic state of interest,  ${}^2\Pi$ . Figure 2.3 shows the schematic structure of low-lying rotational energy levels of  ${}^{138}\text{Ba}{}^{19}\text{F}$  in the  $v=0$  vibrational level of the  ${}^2\Sigma^+$  and  ${}^2\Pi_{1/2,3/2}$  and  ${}^2\Delta_{3/2}$  states, with state symbols and energy values (in  $\text{cm}^{-1}$ ). The transition between electronic states  ${}^2\Sigma^+$  and  ${}^2\Pi_{1/2}$  is used for the detection of BaF molecules. We have also measured the lifetime of the  ${}^2\Pi_{1/2,3/2}$  states in BaF. BaF has an intermediate  ${}^2\Delta_{3/2}$  state, which is shown here for the sake of completeness.

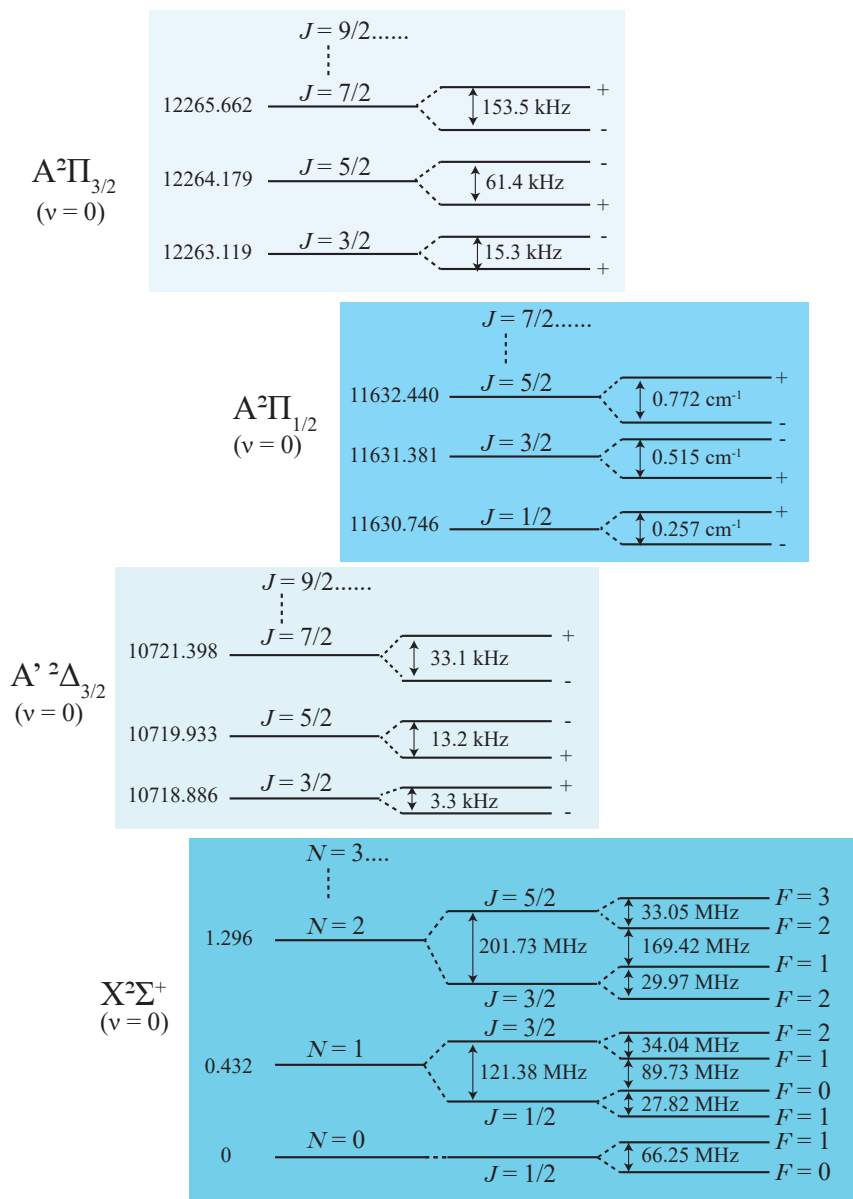


**Figure 2.3** | Energy level structure for the X, A', A states of  $^{138}\text{Ba}^{19}\text{F}$  molecule with energy values specified in units of wavenumbers ( $\text{cm}^{-1}$ , unless stated otherwise). The figure is not drawn to scale. Good quantum numbers and parity (+/-) are indicated for the relevant states. Only three lowest rotational ( $N$ ) states for shown for  $v=0$  vibrational state of  $X^2\Sigma^+$  and three lowest total angular momentum states ( $J$ ) are shown for  $v=0$  vibrational state of  $A^2\Delta_{3/2}$ ,  $A^2\Pi_{1/2}$  and  $A^2\Pi_{3/2}$  electronic states.



Parameter	Label	$X^2\Sigma^+ (\nu = 0)$	$A^2\Pi (\nu = 0)$
Electronic energy [174]	$T_e$	0	15216.34287(47)
Vibrational constant [175, 176, 177]	$\omega_e$	501.96496(13)	509.38
Anharmonicity constant [175, 176, 177]	$\omega_e x_e$	-2.204617(37)	2.18
Rotational constant [174]	$B_e$	0.24975935(23)	0.2528335(37)
Stretching correction [174]	$D_e$	$2.4967(35) \times 10^{-7}$	$2.546(25) \times 10^{-7}$
Spin-rotation [174]	$\gamma_0$	$2.4974(30) \times 10^{-3}$	-
Fine structure coefficient [174]	A	-	281.46138(52)
Nuclear spin-electron spin (MHz) [178]	$b_{00}$	97.6670(10)	-
Nuclear spin-electron spin (dipole-dipole) (MHz)[178]	$c_{00}$	29.846(8)	-
Lambda-doubling constant [174]	p	-	-0.133002(28)
Lambda-doubling constant [174]	q	-	-

**Table 2.2** / Main spectroscopic constants (in  $\text{cm}^{-1}$ , unless stated otherwise) for X and A states in  $^{88}\text{Sr}^{19}\text{F}$ . Values in the parentheses are  $1\sigma$  standard deviation, in units of the last significant digits.

Parameter	Label	$X^2\Sigma^+ (\nu = 0)$	$A^2\Pi (\nu = 0)$
Electronic energy [179]	$T_e$	0	11962.174(64)
Vibrational constant [179]	$\omega_e$	469.4161(19)	437.899(60)
Anharmonicity constant [179]	$\omega_e x_e$	1.83727 (76)	1.854 (12)
Rotational constant [180]	$B_e$	0.2159509(22)	0.2117889(27)
Stretching correction [180]	$D_e$	$1.8476(18) \times 10^{-7}$	$2.0036 (17) \times 10^{-7}$
Spin-rotation [180]	$\gamma_0$	$2.7246(61) \times 10^{-3}$	-
Fine structure coefficient [180]	A	-	632.161(1)
Nuclear spin-electron spin (MHz) [181]	$b_{00}$	63.509(32)	-
Nuclear spin-electron spin (dipole-dipole) (MHz) [181]	$c_{00}$	8.224 (58)	-
Lambda-doubling constant [180]	p	-	-0.257310(17)
Lambda-doubling constant [180]	q	-	$-0.0840(29) \times 10^{-3}$

**Table 2.3** / Main spectroscopic constants (in  $\text{cm}^{-1}$ , unless stated otherwise) for X and A states in  $^{138}\text{Ba}^{19}\text{F}$ . Values in the parentheses are  $1\sigma$  standard deviation, in units of the last significant digits.

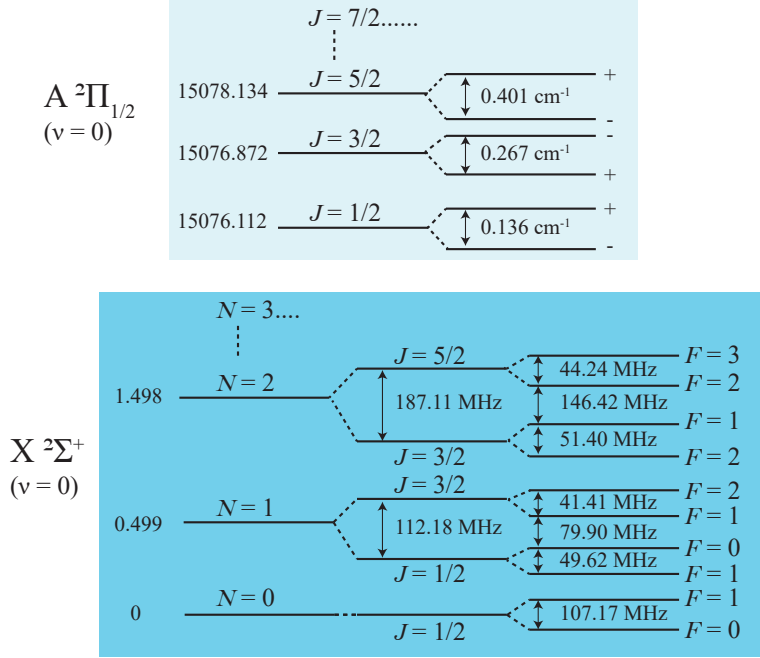


**Figure 2.4** | Energy level structure for the X, A states of  $^{88}\text{Sr}^{19}\text{F}$  molecule which is of relevance for understanding the results presented in this thesis. The energy values are specified in units of wavenumbers ( $\text{cm}^{-1}$ , unless stated otherwise). The figure is not drawn to scale. Only three lowest rotational ( $N$ ) states for  $v=0$  vibrational state of  $X^2\Sigma^+$  electronic state and three lowest total angular momentum states ( $J$ ) are shown for  $v=0$  vibrational state of  $A^2\Pi_{1/2}$  electronic state.

Figure 2.4 shows the schematic structure of low-lying rotational energy levels of  $^{88}\text{Sr}^{19}\text{F}$  in the  $v=0$  level of the  $^2\Sigma^+$  and  $^2\Pi_{1/2}$  state. The laser transition  $A^2\Pi_{1/2}(J=1/2) \leftarrow X^2\Sigma^+(v=0, N=1)$  is used for the detection of SrF.

## 2.7. Selection rules

In this section, the selection rules are discussed for the case of zero electric and magnetic fields. This is of relevance to the rotational spectrum of BaF shown in Chapter-3. The electric dipole transition in the diatomic molecules are determined by the matrix elements of the dipole operator-

$$\mu_e(f, i) = \int \psi_f^* \mu_e(f, i) \psi_i d\tau, \quad (2.16)$$

where  $i$  and  $f$  denote the initial and final state involved in the transition respectively. The  $\mu_e$  arises from the summation over the nuclear and electronic charges-

$$\mu_e = e \left\{ \sum_{\alpha} Z_{\alpha} r_{\alpha} - \sum_i r_i \right\}, \quad (2.17)$$

where  $Z$  is the atomic number,  $r_{\alpha}$  and  $r_i$  is the center of mass position of  $\alpha$ th nuclei and  $i$ th electron respectively, in the molecule-fixed frame. For a component  $\mu_e \cos(\theta)$  along the electric field axis and the total wavefunctions,  $\psi_i = \psi'_e(r_{\alpha}, r_i) \psi'_v(r_{\alpha}) Y_{J', M'}$  and  $\psi_f = \psi_e(r_{\alpha}, r_i) \psi_v(r_{\alpha}) Y_{J, M}$ , corresponding to the product of the rotational, vibrational and electronic wave functions, the equation 1.5 reduces to [167]

$$\begin{aligned} \mu_e(f, i) = \langle J, M | \cos(\theta) | J', M' \rangle \times & \left[ \int_{\alpha} \psi_v^*(r_{\alpha}) \psi'_v(r_{\alpha}) dV_{\alpha} \right] \\ & \times \left[ -e \int_i \psi_e^*(r_i, r_{\alpha}) \sum_i r_i \psi'_e(r_i, r_{\alpha}) dV_i \right], \end{aligned} \quad (2.18)$$

which represents the segregated rotational, vibrational and electronic part. The first term in the product gives the selection rules  $\Delta J = 0, \pm 1$ ,  $\Delta M = 0, \pm 1$  for the associated Legendre polynomials solution for the rotational motion of the nuclei in the diatomic molecule. The second integral describes the overlap of the vibrational functions in the ground and the excited state, its square of this integral is called the Franck-Condon factor, which is calculated using molecule structure calculations. Apart from that, there are no selection rules for the vibrational transitions. Lastly, the electronic part will be non zero only if,  $\psi_e^* r_i \psi'_e$  is symmetric with respect to the space-fixed inversion operator. In other words, the product  $\psi_e^* \psi'_e$  should be antisymmetric, leading to the parity selection rule  $+$   $\leftrightarrow$   $-$ . The allowed electric dipole transitions are the ones between the states of opposite parity.

## 2.8. Field-Molecule interaction

### 2.8.1. Stark effect

In the presence of a strong enough electric field, a molecule acquire an induced electric dipole moment along the external field direction which arises from the superposition of states. This dipole moment of the molecule is not a static dipole moment. When the external electric field ( $\vec{E}$ ), say along the  $\hat{z}$ -direction interacts with this induced dipole moment ( $\vec{d}$ ) in a polar diatomic molecule, the energy levels of the molecule split, known as the Stark effect. The Stark interaction is represented by an effective Hamiltonian given by

$$\mathbf{H}_S = \vec{d} \cdot \vec{E}. \quad (2.19)$$

The energy shift  $\Delta E$  for any state  $|N, M_N\rangle$ , where  $N$  is the rotational quantum number and  $M_N$  is the projection of the rotational quantum number along the electric field axis is calculated using the perturbation theory to be

$$\Delta E = \langle N, M_N | \mathbf{H}_S | N, M_N \rangle + \sum_{N'} \frac{(\langle N', M'_N | \mathbf{H}_S | N, M_N \rangle)^2}{(E_N - E_{N'})}. \quad (2.20)$$

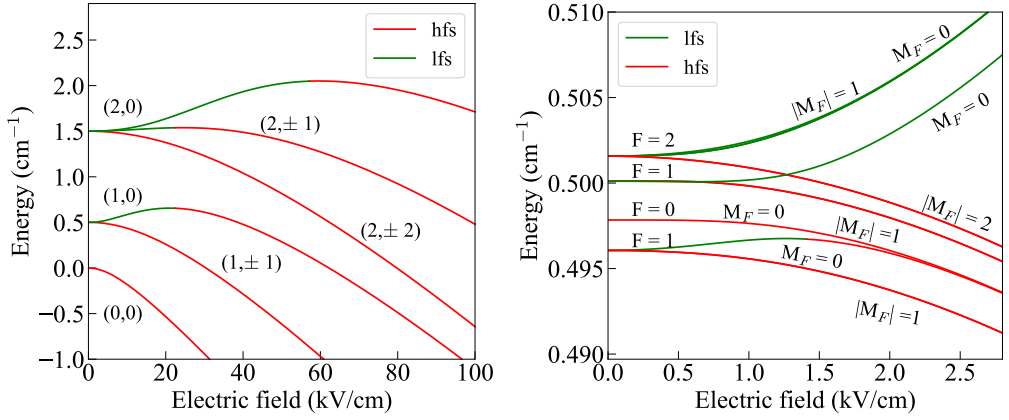


**Figure 2.5** | (a) The Stark shift of the three lowest rotational levels of SrF ( $N, M_N$ ). (b) Resolved Stark shifts for the hyperfine levels ( $F, M_F$ ) in  $N = 1$  rotational level. The states are labelled with zero-field quantum numbers.

The matrix elements in the above expression are given by[167]

$$\begin{aligned} \langle N', M'_N | \mathbf{H}_S | N, M_N \rangle &= -d\mathcal{E}(2N+1)(2N'+1)^{1/2}(-1)^{M'-M} \\ &\times \begin{pmatrix} N & 1 & N' \\ -M_N & 0 & M_N \end{pmatrix} \begin{pmatrix} N & 1 & N' \\ -\Lambda & 0 & \Lambda \end{pmatrix} \end{aligned} \quad (2.21)$$

where  $\lambda$  is the component of the electronic angular momentum along the internuclear axis. Now for BaF and SrF in their ground state  $^2\Sigma^+$ , the value of  $\Lambda$  is zero. 3j-symbol is only non-zero if  $M = M'$  and  $N = N \pm 1$ . Hence, the first-order Stark shift is zero. The electric field mixes each rotational level ( $N$ ) with the adjacent rotational levels ( $N \pm 1$ ). The Stark shift can thus be represented by the following truncated  $3 \times 3$  matrix [167], where  $B$  is the rotational constant. This  $3 \times 3$  matrix is an approximation because in reality the stark matrix is infinite and the accuracy depends on the number of rotational states taken into consideration.

	$ N-1\rangle$	$ N\rangle$	$ N+1\rangle$
$\langle N-1 $	$BN(N-1)$	$-d\mathcal{E}\left\{\frac{N^2-M_N^2}{(2N-1)(2N+1)}\right\}^{1/2}$	0
$\langle N $	$-d\mathcal{E}\left\{\frac{N^2-M_N^2}{(2N-1)(2N+1)}\right\}^{1/2}$	$BN(N+1)$	$-d\mathcal{E}\left\{\frac{(N+1)^2-M_N^2}{(2N+1)(2N+3)}\right\}^{1/2}$
$\langle N+1 $	0	$-d\mathcal{E}\left\{\frac{(N+1)^2-M_N^2}{(2N+1)(2N+3)}\right\}^{1/2}$	$B(N+1)(N+2)$

An expression for the second-order Stark energy can be derived using the above matrix

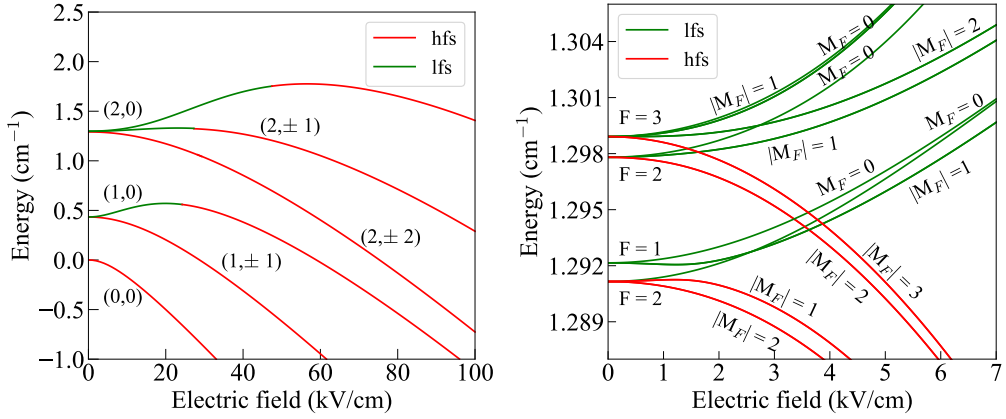


**Figure 2.6** | (a) The Stark shift of the three lowest rotational levels of BaF ( $N, M_N$ ). (b) Resolved Stark shifts for the hyperfine levels ( $F, M_F$ ) in  $N = 2$  rotational level. The states are labelled with zero-field quantum numbers.

elements and is as follows [167]

$$\Delta E(N, M_N) = \begin{cases} \frac{d^2 \mathcal{E}^2}{2B} \left\{ \frac{N(N+1) - 3M_N^2}{N(N+1)(2N-1)(2N+3)} \right\} & |N, M_N\rangle \neq |0, 0\rangle \\ \frac{d^2 \mathcal{E}^2}{6B} & |N, M_N\rangle = |0, 0\rangle. \end{cases} \quad (2.22)$$

The Stark shift of the different rotational states in the electronic ground state,  $\Delta E(0, 0) = \frac{d^2 \mathcal{E}^2}{6B}$  due to mixing with  $|1, 0\rangle$ ,  $\Delta E(1, 0) = \frac{d^2 \mathcal{E}^2}{10B}$  due to mixing with  $|0, 0\rangle$  and  $|2, 0\rangle$ , and  $\Delta E(1, 1) = -\frac{d^2 \mathcal{E}^2}{20B}$  due to mixing with  $|2, 1\rangle$  state.

Figure 2.5(a) shows the stark shift of  $N = 0, 1, 2$  rotational states in the electronic ground state of SrF and Figure 2.5(b) shows a zoom-in of the Stark shifts in the  $N = 1$  rotational state for all hyperfine states calculated using PGOPHER. The value of the permanent electric dipole moment of SrF in the ground electronic state used for the calculation of this Stark curve is  $3.4676(10)$  D [182].

In our experiment, we detect the SrF molecules decelerated in the  $N=1$  rotational state of the ground electronic state of SrF. The  $X^2\Sigma^+$  ( $\nu = 0, N = 1, M_N = 0$ ) state is low field seeking upto an electric field of 21 kV/cm [182]. For our decelerator geometry, this correspond to a maximum voltage amplitude of 5 kV applied to the ring electrodes in the traveling-wave decelerator. For the NL-eEDM experiment, we plan to decelerate the BaF molecules in the  $N = 2$  rotational state because this rotational state has a larger stark shift. Currently, we are in the process of the voltage upgrade of our decelerator from 5 kV to 10 kV, which would correspond to the electric fields of 42 KV/cm inside the decelerator rings, which is close to the turning point of the electric field in the  $N = 2$  rotational state of BaF which is 55 kV/cm [183]. Figure 2.6(a) shows the stark shift of  $N = 0, 1, 2$  rotational states in the ground state

of BaF and Figure 2.6(b) shows a zoom-in of the Stark shifts in the  $N = 2$  rotational state for all hyperfine states calculated using PGOPHER. An induced electric dipole moment of 3.170(3) D [181] is used for the calculation of this Stark curve.

### 2.8.2. Zeeman effect

A particle with a magnetic moment, associated with the spin of electrons and nuclei and orbital angular momentum will experience an energy shift in the presence of the external magnetic field ( $\mathcal{B}$ ). The effective Zeeman Hamiltonian is given by

$$H_z = \mu_{\text{eff}} \cdot \mathcal{B}, \quad (2.23)$$

where

$$\mu_{\text{eff}} = (g_L \mathbf{L} + g_S \mathbf{S}) \mu_B. \quad (2.24)$$

Here,  $g_L = 1$  and  $g_S$  is approximately 2. The Hamiltonian does not include the anisotropic correction or the rotational or nuclear Zeeman interactions. These are typically three orders of magnitude smaller than the electronic term and can be neglected. The magnetic field shift the levels of  $X^2\Sigma^+$  state in SrF and BaF. For the  $A^2\Pi_{1/2}$  state,  $g \sim 0$  and hence this state do not experience any Zeeman shifts. For a magnetic field aligned along the z-axis, the Zeeman shift is given by the expectation value of the Hamiltonian ( $\vec{L} = 0$ ) for  $^2\Sigma^+$  state

$$\langle H_z \rangle = g_s \mu_B \mathcal{B} \langle \hat{S}_z \rangle. \quad (2.25)$$

First we consider the case of the weak magnetic field, when the Zeeman shift is smaller than the hyperfine splitting. We consider the coupled basis  $|N, S, J, I, F, m_F\rangle$ . To calculate  $\langle S_z \rangle$ , we apply the projection theory to account for the angular momentum couplings. The zeeman shift is given by

$$\begin{aligned} \langle H_z \rangle &= g_s \mu_B \mathcal{B} \langle \hat{S}_z \rangle \\ &= g_s \mu_B \mathcal{B} \frac{\langle \hat{S} \cdot \hat{J} \rangle}{J(J+1)} \langle \hat{J}_z \rangle \\ &= g_s \mu_B \mathcal{B} \frac{\langle \hat{S} \cdot \hat{J} \rangle \langle \hat{J} \cdot \hat{F} \rangle}{J(J+1)F(F+1)} \langle \hat{F}_z \rangle \\ &= g_F \mu_B \mathcal{B} m_F, \end{aligned} \quad (2.26)$$

where

$$g_F = g_s \frac{S(S+1) + J(J+1) - N(N+1)}{2J(J+1)} \frac{F(F+1) + J(J+1) - I(I+1)}{2F(F+1)}. \quad (2.27)$$

The value of  $g_F$  calculated for  $F = 1^-, 0, 1^+, 2$  states in  $N = 1$  rotational state is -0.33, 0, 0.833 and 0.5 respectively. The values calculated using the full Hamiltonian is -0.47, 0, 0.97 and 0.5 for  $F = 1^-, 0, 1^+, 2$  hyperfine level in the SrF respectively. The difference in the  $g_F$  values for  $1^-$  and  $1^+$  is because these states are not states with pure  $J$ , but are instead mixtures of  $J = 1/2$  and  $J = 3/2$ . The Zeeman shift of the electronic ground state  $^2\Sigma^+(N = 1)$  of SrF and BaF is shown in Figure 2.7 (a,b).

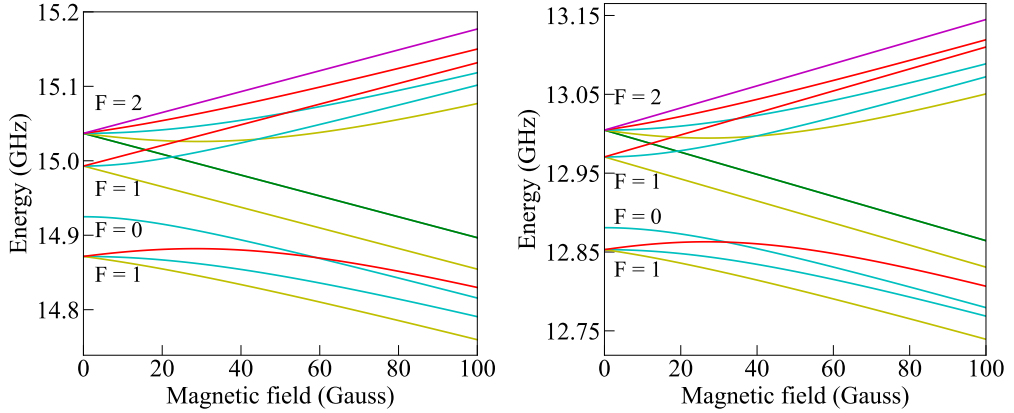


**Figure 2.7** | Zeeman splitting for the four hyperfine levels ( $F$ ) in  $X^2\Sigma^+(N=1)$  state with respect to  $X^2\Sigma^+(N=0, F=0)$  for (a) SrF and (b) BaF. The energy levels are labeled by their  $m_F$  value at zero field with  $m_F = 2$  (magenta),  $m_F = 1$  (red),  $m_F = 0$  (cyan),  $m_F = -1$  (yellow),  $m_F = -2$  (green). The levels which increase in energy as the magnetic field increases are low field seeking (lfs) and the levels whose energy decreases are high field seeking (hfs).

For large magnetic fields, when the Zeeman shift is larger than the hyperfine splitting, the calculation of the expectation value of Hamiltonian is done in the uncoupled basis  $|N, M_N\rangle |S, M_S\rangle |I, M_I\rangle$ . The Zeeman shift is then given by

$$\langle H_z \rangle = g_s \mu_B \mathcal{B} m_s. \quad (2.28)$$

The  $m_s = 1/2$  states are weak field-seeking and  $m_s = -1/2$  states are strong field-seeking. The Zeeman shift is linear with the magnetic field both in the case of weak and strong fields. A magnetic field is generally applied to the molecules for the purpose of remixing the dark states.

## 2.9. Conclusions

This chapter discusses the energy level structure of the electronic ground state and low-lying excited electronic states;  $X^2\Sigma^+$ ,  $A'^2\Delta$  and  $A^2\Pi$  states in BaF and  $X^2\Sigma^+$  and  $A^2\Pi$  states in SrF. Further, the splitting of the energy levels of the ground electronic state,  $X^2\Sigma^+$  in SrF and BaF is discussed in the presence of electric and magnetic fields.





# 3

## A supersonic laser ablation beam source of SrF and BaF molecules\*

Nothing happens until something moves.-Albert Einstein

Supersonic expansion is a proven method to produce beams of molecules with a small velocity spread and low translational and rotational temperature resulting in relatively high population of the lowest energy states [94, 184]. A small velocity spread is desirable for high-resolution spectroscopy [185, 186, 187], collision experiments [188, 189] and also for efficient deceleration of molecules in a Stark decelerator [105, 115, 190]. This is because it reduces Doppler broadening, ensures good resolution of the collision energy in collision experiments and facilitates good phase-space matching at the entrance of the Stark decelerator.

The smallest relative velocity spread and lowest temperatures have been achieved in the expansion of helium through a pulsed nozzle at high pressures [95]. Beams of stable molecules were produced by expansion of molecules seeded in light carrier gases like beams of nitric oxide and aniline seeded in helium [191, 97] with rotational temperatures of order 1 K. The coldest translational temperatures can be achieved when the seeded molecules completely thermalize with the carrier gas. However, for the production of some molecular species, laser ablation is needed which sometimes leads to a larger velocity spread [192]. The ablation technique was originally used to generate clusters of atoms where a high energy laser beam vaporizes the material of interest which is then entrained in a supersonically expanding gas flow [193, 194, 195]. Later, metal-atom beams were produced in which the products of laser-ablation of the corresponding solid target were entrained in neutral gases expanding supersonically from pulsed valves for crossed beam experiments [196, 197, 198]. Beams of

---

\*The results presented in this chapter are published in P. Aggarwal et al., Rev. Sci. Instrum. 92, 033202 (2021)

metal compounds are now also produced through the reactions of ablation products with impurity gases added to the carrier gas. For example, beams of SrF [177], CoF [199], YF [200], YbF [98], HfF<sup>+</sup>[201] and BaF [192, 202] were produced by adding SF<sub>6</sub> as an impurity gas.

In the present study, a combination of an Even-Lavie valve [203] with laser ablation is presented. Such a valve can produce short ( $\sim 25 \mu\text{s}$ ) and dense pulses with relatively low operating currents in comparison with other valves, which prevents the heating of the gas pulse. It can also be operated at high backing pressures which leads to a large pressure gradient, thereby reducing the kinetic temperature of the gas pulse. Such a combination has previously been used to produce beams to study reaction dynamics [204, 205] and collision experiments between atoms and molecules in a magnetic and a static quadrupole trap [206, 207]. Droplets of helium have also been produced by expansion through a pulsed Even-Lavie valve to which lithium atoms are doped by ablation [208]. This combination has been used here for the production of supersonic beams of two alkaline-earth metal fluorides, SrF and BaF. These relatively heavy molecules are considered as target probes to test fundamental symmetry violation beyond the Standard Model [90, 209]. We demonstrate the small velocity spread of the produced beams of SrF and BaF and compare our results with other ablation sources for metal fluorides [98, 202, 192].

### 3.1. Experimental setup

Our experimental setup for the production of the molecules is shown in Figure 3.1. An Even-Lavie valve [96] creates pulses of carrier gas argon seeded with 2% SF<sub>6</sub> with a gate length set to  $\sim 35 \mu\text{s}$ . The metal of interest in our case barium or strontium is mounted in the form of a 3 mm thick disk with a diameter of 56 mm inside a vacuum chamber at a distance of 4 mm along the line of expansion and 5 mm in the direction transverse to the beam. The transverse distance of 5 mm has been optimised to obtain maximum molecular flux, with the beam collapsing for a distance less than 2 mm (shown in section 3.4.3). The target is rotated by a vacuum compatible Picomotor actuator with a rotating shaft (Newport 8341-V). Laser light pulses of 10 ns length, 20 mJ energy, 4 mm spot size, at a wavelength of 532 nm, from a Nd:YAG laser ablate the metal target at the 3 mm thick surface of the disk. The spot size of the ablation pulse is slightly larger than the maximum 3 mm wide region on the side of the target disk which can be ablated. The ablation products are entrained in the expanding carrier gas. The molecules formed are thermalized by undergoing collisions with the corresponding noble gas atoms. A skimmer of diameter 5 mm (Beam Dynamics, Model 2) mounted at distance 28 cm from the exit of the valve selects the central part of the beam. The molecules are detected 58 cm downstream of the valve exit. The source is operated at a repetition rate of 10 Hz.

The whole setup is housed inside a total of three CF150 vacuum chambers. The beam expands and cools in the first two chambers collectively referred to as the source chamber. The detection of the beam takes place in the third chamber. Two 700 l/s turbopumps evacuate the three vacuum chambers. During the operation of the source, the residual gas pressure in the source chamber and the detection chamber is  $3 \times 10^{-6}$  and  $1.2 \times 10^{-7}$  mbar, respectively. When the source is not operating, the background pressure is  $1.5 \times 10^{-7}$  and

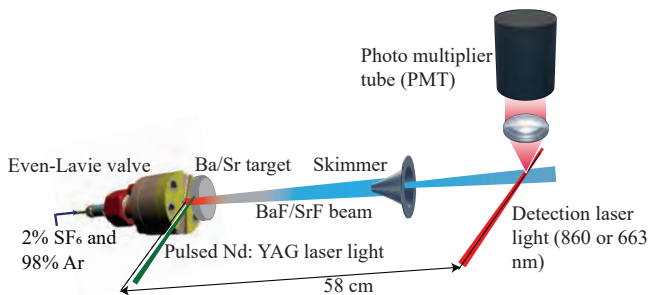


**Figure 3.1** | Experimental setup of the supersonic source. An Even-Lavie valve produces short pulses of carrier gas consisting of 98% Ar and 2% SF<sub>6</sub>. A high-energy Nd:YAG laser light pulse ablates the metal of interest which is then entrained in the supersonically expanding carrier gas. The molecules in the  $X^2\Sigma^+$  ( $\nu = 0$ ,  $N=1$ ) state are detected by laser-induced fluorescence light which is collected on a photo-multiplier tube cathode. Only the collection lens is shown in the figure.

$9 \times 10^{-8}$  mbar in the source and detection chamber, respectively.

## 3.2. Lasers

We employ a total of three lasers in our experiment. The first is the ablation laser (Continuum, Inlite II-20). This is a pulsed Nd:YAG laser which emits 5 ns long pulses of  $\sim 6$  mJ at a wavelength of 532 nm, running at a repetition rate of 10 Hz. The other two lasers are used to detect SrF and BaF respectively, by exciting the molecules from the ground electronic state to the excited electronic state,  $A^2\Pi_{1/2}$  ( $\nu = 0$ ,  $J = 1/2$ )  $\leftarrow X^2\Sigma^+$  ( $\nu = 0$ ) at wavelengths of 663 nm and 860 nm, respectively.

A home-built external cavity diode laser (ECDL) (Thorlabs, HL6545MG) with a maximum output laser power of 50 mW is used to drive the transition in the molecule around 663 nm wavelength. A beam-splitter splits the light from the ECDL, a part of which is sent to the scanning Fabry Perot cavity (Thorlabs, SA200-5B) to lock the detection laser frequency relative to a commercially stabilised He-Ne laser (Thorlabs, HRS015B). Another part is sent to the electro-optical modulator (EOM) (Jenoptik, PM660) which is driven by a sinusoidal signal frequency 42 MHz and at modulation index 2.6. The EOM is used to produce sidebands to address the hyperfine structure of the  $N = 1$  rotational state in the electronic ground state  $X^2\Sigma^+$  ( $\nu = 0$ ). The output from the EOM is then passed through a semiconductor optical amplifier (Toptica Photonics, BoosTA) before it is sent to the experiment via a single-mode optical fiber as shown in Fig. 3.2.

A commercial Ti:sapphire laser (Coherent, MBR-10) with maximum power output 300 mW is employed to drive the BaF molecular transition. The laser light has a linewidth of order 100 kHz and is pumped by light at 532 nm from a solid-state laser (Coherent Verdi, V10). There are no sidebands added to the 860 nm laser light for addressing the hyperfine structure of the  $N = 1$  rotational state. Part of the 860 nm laser light is sent to a wavelength meter

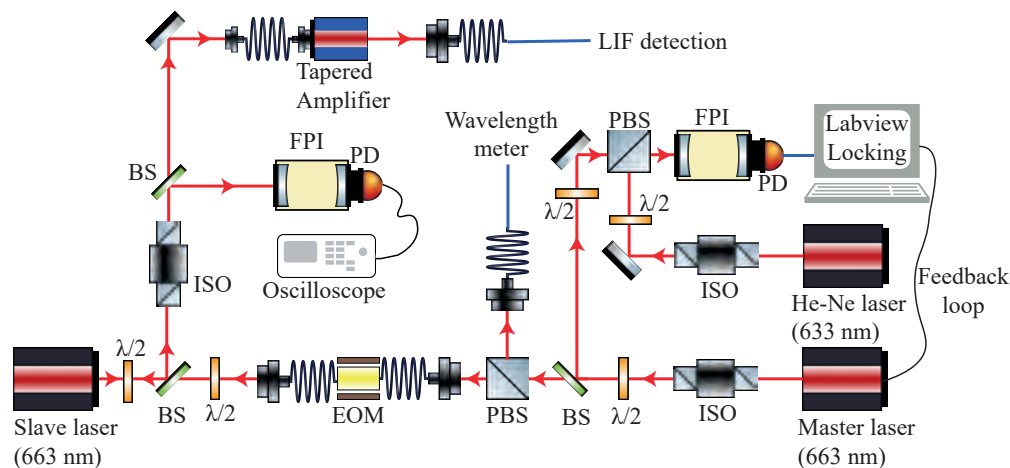


**Figure 3.2** | Optical setup for the detection laser light at a wavelength of 663 nm, showing the locking of the laser in reference to a commercially stabilized He-Ne laser, creation of the sidebands to address the hyperfine structure in  $N = 1$  rotational state and the amplification of the light via a tapered amplifier.

(HighFinesse, WS6) for locking the detection laser frequency. Another part of the laser light is sent through an acousto-optic modulator (AOM, Brimrose TEM-200-50). For the results presented in this chapter, the zero-order diffracted beam from the AOM which is continuous wave (cw) light, is coupled to a single-mode fiber and transported to the experiment. For the lifetime measurements of the excited electronic state in BaF (see chapter-4), pulses are created from this cw-light by selecting the first-order diffracted light beam from an AOM powered at a radio frequency (rf) of 200 MHz. The pulse structure and the amplitude are controlled by switching the rf (Mini Circuits ZASWA-2-50-DR+) to obtain pulses which then interact with the BaF molecular beam. The first order diffracted light is then coupled to a single-mode fiber and sent to the experiment site and the zeroth order light is dumped as shown in Figure 3.3.

### 3.3. Data Acquisition System

The trigger signal applied to drive the valve driver and the ablation laser is generated by a 8-channel delay/pulse generator (BNC Model 575). A photo-multiplier tube is used to collect the laser-induced fluorescence (LIF) signal from the molecules. We use two different PMTs (Hamamatsu H7422P-40 and H7422P-50) for light collection at the wavelengths 663 nm and 860 nm, respectively. The quantum efficiency of these PMTs at 663 nm and 860 nm are 0.39 and 0.13 respectively. The photons arriving on the active area (photocathode) of the PMT (5 mm  $\times$  5 mm) are detected with a probability corresponding to the quantum efficiency of the respective devices. Each detected photon generates an electronic pulse. These electrical signals are sent to a single-pulse discriminator and a logic-level converter and further goes as a TTL to a time-to-digital converter (TDC) (Signadyne, TDC-H3344). The TDC is

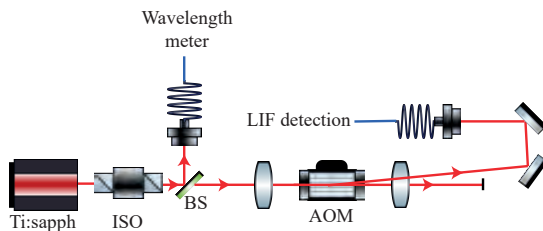


**Figure 3.3** | Optical setup for the detection laser light at a wavelength of 860 nm. A part of the light is sent to the wavelength meter to lock the detection laser frequency at 860 nm and the other part is allowed to pass through an acousto-optic modulator (AOM). The first-order diffracted light from the AOM powered at a radio frequency of 200 MHz is coupled to a single-mode fiber and transported to the experiment site. The zeroth-order light from the AOM is sent to a beam dump.

synchronised to the pulse generator using the 10 MHz reference out from the BNC. The TDC records the timestamps of the input signal. Two channels of the TDC are used to acquire the time stamps for the molecular pulse and from the PMT. The data is processed online using a home-built LabView program and saved for offline analysis using the PCI eXtensions for Instrumentation (PXI)(National Instruments) standard. The data presented in this thesis has been analysed using a Python-based script. We obtain time-of-flight profiles which are one-dimensional binned histograms.

## 3.4. Results

### 3.4.1. Time of flight profile

In the detection chamber, the molecules SrF and BaF are detected by laser-induced fluorescence by exciting the molecules from the ground electronic state  $X^2\Sigma^+$  ( $v = 0$ ,  $N = 1$ ) to the first electronically excited state  $A^2\Pi_{1/2}$  ( $v = 0$ ,  $J = 1/2$ ) by laser light at a wavelength of 663 nm for SrF detection and by light at a wavelength of 860 nm for BaF detection respectively, from the laser systems discussed in the previous section. The hyperfine levels in the ground state of SrF are approximately covered by frequency sidebands to the laser light frequency, which were created by passing the laser light through an electro-optic modulator (see Figure 3.2). For the detection of BaF, we did not use frequency sidebands, therefore the hyperfine structure in the ground state of BaF is not covered and the detection laser light is tuned to the strongest signal when probing the  $N = 1$  level. The fluorescence emitted by BaF and SrF molecules is collected by a 2-in. achromatic lens of 75 mm focal length (65.7 mm back focal length) in the upward direction and 1-in. achromatic lens of 35 mm focal length (27.3 mm back focal length) in the upward and downward direction, respectively (see Fig 3.4, 3.5). The 663 nm wavelength light is further imaged with a 1-in. biconvex lens of 60 mm focal length onto a photo multiplier tube (PMT) with a total magnification of the entire lens assembly equal to 1.7. The 860 nm wavelength light is imaged onto the PMT, using a 2-in. achromat lens and a 1-in. biconvex lens of 25.4 mm focal length with a total

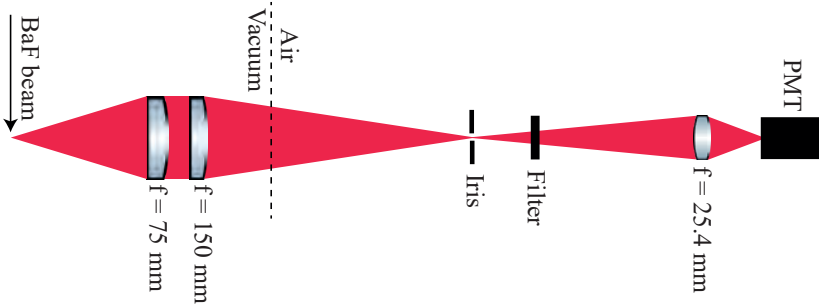


**Figure 3.4** | Collection optics assembly for detection of BaF molecular beam (rotated by  $90^\circ$  in the clockwise direction from the actual vertical configuration of the PMT in the experimental setup). The fluorescence emitted by the BaF molecules on exciting them on the transition  $A^2\Pi_{1/2} (\nu = 0, J = 1/2) \leftarrow X^2\Sigma^+ (\nu = 0, N = 1)$ , at a wavelength of 860 nm is collected from the upward direction by a 2-in. achromat lens of focal length 75 mm. The light is then imaged onto the PMT (Hamamatsu H7422P-50) via a combination of a 2-in. achromat lens of focal length 150 mm and 1-in. lens of focal length of 25.4 mm. To cut off the background light, a fluorescence filter centered around the transition wavelength 860 nm is placed along the path of the laser light. The entire lens assembly has a resultant magnification of 0.5.

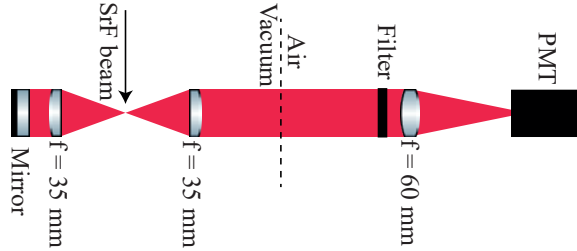


**Figure 3.5** | Collection optics assembly for detection of SrF molecular beam (rotated by  $90^\circ$  in the clockwise direction from the actual vertical configuration of the PMT in the experimental setup). The fluorescence emitted by the SrF molecules on exciting them on the transition  $A^2\Pi_{1/2} (\nu = 0, J = 1/2) \leftarrow X^2\Sigma^+ (\nu = 0, N = 1)$ , at a wavelength of 663 nm is collected both in the upward and downward direction by a 1-in. achromat lens with a focal length of 35 mm. The fluorescence is imaged onto a PMT (Hamamatsu H7422P-40) with a 1-in. biconvex lens of focal length 60 mm. A fluorescence filter cuts off the light far away from the resonant light.

magnification of the entire lens assembly equal to 0.5. A narrow band-pass filter with transmission of 99% (60%) at the wavelength of 663(10) nm [860(10) nm] is placed in front of the PMT to discriminate the fluorescence photons corresponding to the exciting transition from background room light. The detection chamber is blackened inside with paint (AZ Technology MLS-85-HB) to reduce the background counts from scattered laser light. The

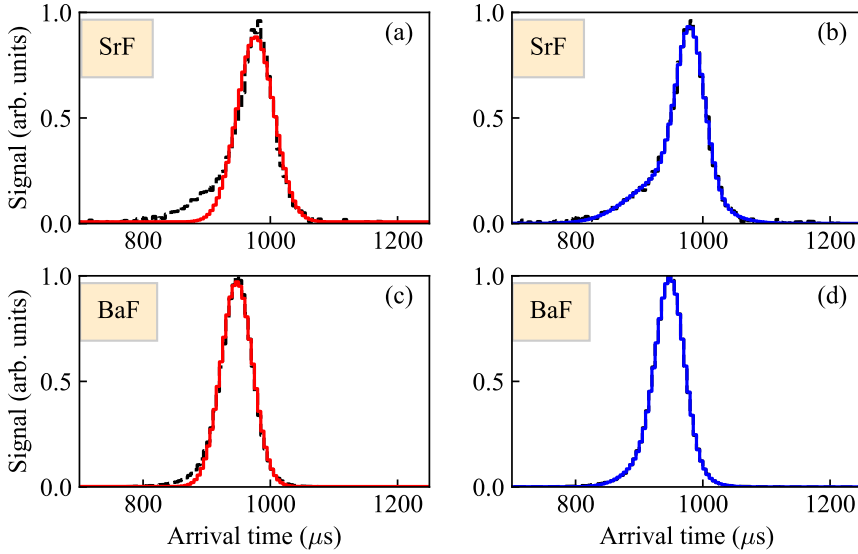


**Figure 3.6** | Time-of-flight profile of SrF (a,b) and BaF (c,d) molecular beam at a backing pressure of 8 bar obtained by laser-induced fluorescence detection on the transition  $A^2\Pi_{1/2} (\nu = 0, J = 1/2) \leftarrow X^2\Sigma^+ (\nu = 0, N = 1)$  shown with dotted black line. The solid red line depicts a single Gaussian profile fitted to the data and the solid blue line depicts a fit with two Gaussian profiles. The SrF and BaF molecules travel 58.0 cm distance in 983(7)  $\mu$ s and 951(6)  $\mu$ s, respectively.

chamber contains copper aperture rings with knife edges along their inside diameter in the detection laser light path to avoid scattering of light.

The time-of-flight profiles for SrF and BaF molecules taken at backing pressure of 8 bar is shown in Figure 3.6 (dotted black line). The time-of-flight profile is shown over the time frame 700-1250  $\mu$ s with a bin size of 5  $\mu$ s where  $t = 0$  corresponds to time of ablation of the metal target with the pulsed Nd: YAG laser operating at a repetition rate of 10 Hz. The arrival time of the SrF and BaF molecular beam is 983(7)  $\mu$ s and 951(6)  $\mu$ s respectively. The velocity distribution of the molecules with central velocity  $v_0$  and with longitudinal velocities in the interval  $v$  to  $v+dv$  can be expressed as

$$f(v) dv = Av^3 \exp(-m(v - v_0)^2/2k_B T) dv, \quad (3.1)$$

where  $A$  is a normalisation constant,  $m$  is the mass of the molecule and  $T$  is the translational temperature [210, 211]. Distribution in Equation 3.1 can be converted to a time-of-flight (TOF) distribution by substituting  $t = L/v$  and  $t_0 = L/v_0$ ,

$$g(t) dt = \frac{CL^4}{t^5} \exp\left(-\frac{mL^2}{2k_B T} \left(\frac{t - t_0}{t t_0}\right)^2\right) dt. \quad (3.2)$$

Here we take into account that the molecules start from a very short pulse. The above

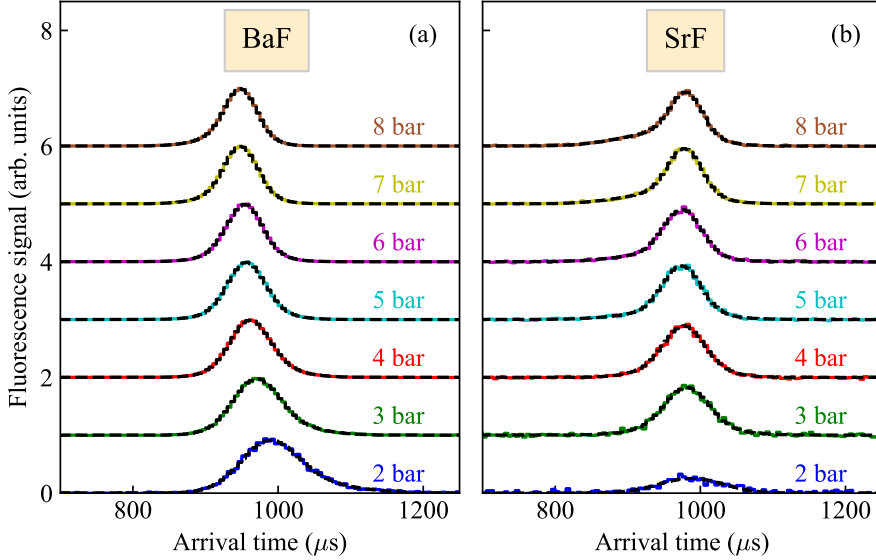


**Figure 3.7** | Time-of-flight profiles of BaF (panel (a)) and SrF (panel (b)) molecular beams at different backing pressures in the range 2-8 bar obtained by laser-induced fluorescence detection on the transition  $A^2\Pi_{1/2} (\nu = 0, J = 1/2) \leftarrow X^2\Sigma^+ (\nu=0, N = 1)$ . The dashed black line superimposed on different TOF profiles depicts the two Gaussian fit to the time-of-flight profiles of BaF and SrF. We have added an offset to the different time-of-flight profiles for the purpose of clarity.

distribution resembles a Gaussian profile on using the approximation,  $t \approx t_0$ :

$$g(t) dt = \frac{CL^4}{t_0^5} \exp\left(-\frac{mL^2}{2k_B T} \frac{(t - t_0)^2}{t_0^4}\right) dt \quad (3.3)$$

Therefore, fitting a Gaussian profile to the time-of-flight profile is a heuristic way of approximating the data, to extract the properties of the beam. The result of a single Gaussian shape to the data are shown by solid red line in Figure 3.6 (a,c). Apparently, a single Gaussian does not describe all the data, notably for SrF, which has excess signal counts at the leading edge of the TOF profile. This is observed mostly for higher backing pressure conditions in case of SrF, and we interpret that it is a part of the molecular beam which is not well thermalized with the carrier gas. To quantify the non-thermalized part, we fit two Gaussian profiles to our TOF profile (shown by solid blue line in Figure 3.6(b,d)). The broader pedestals under the narrower TOF peaks contain 43% and 29% of the observed molecules for SrF and BaF respectively (see Figure 3.6).

In Figure 3.7, we fit two Gaussian profiles to SrF and BaF time-of-flight profiles at different backing pressures. The reduced  $\chi^2$ , where two Gaussian profiles are used, of the 14 fits in Figure 3.7 vary between 0.90 and 1.17. The broader pedestal under the main peak



contributes between 26%-43% to the arrival-time histogram for SrF with their contribution increasing with higher backing pressure. The broader Gaussian structure contributes 25%-31% to the time-of-flight histogram of BaF without any specific trend with the backing pressure.

The further analysis is based only on the narrow feature in the time-of-flight profile.

### 3.4.2. Relative velocity spread

The velocity of SrF and BaF molecular beam is calculated to be 590(4) m/s and 610(4) m/s respectively. The time-spread (FWHM) of the time-of-flight profile of SrF and BaF is given by  $2\sqrt{2 \ln(2)} \sigma$  where  $\sigma$  is the width of the Gaussian fit. The time variances of the SrF and BaF beam at a backing pressure of 8 bars are calculated to be 52.4(5)  $\mu$ s and 51.2(4)  $\mu$ s respectively. The corresponding velocity spread  $\Delta v$  is calculated to be 31.5(3) m/s and 32.9(2) m/s for SrF and BaF, respectively, by assuming that the molecules start from a very short pulse, and hence  $v = L/t$ . The relative velocity spread  $\Delta v/v$  is a representation of the cooling process and gives a measure of the translational degrees of freedom. We compare our relative velocity values with those obtained in other supersonic beam sources for metal fluorides in Table 3.2. Using,  $\Delta v(\text{FWHM}) = \sqrt{8k_B T \ln 2 / m}$  [212], the translational temperature of SrF and BaF is calculated to be 2.3(1) K and 5.2(1) K respectively.

The typical velocity of argon in a supersonic expansion from an Even-Lavie valve at room temperature is 570 m/s with a small velocity spread of 56 m/s at 5 bars backing pressure [213, 214]. The velocity spread of the two molecular beams, SrF and BaF with argon as the carrier gas at 5 bar backing pressure, is 36.8(6) m/s and 37.2(2) m/s, respectively. The velocity spread of the BaF and SrF is very similar despite the fact that the mass of BaF is 1.46 times higher than SrF. This means that the velocity of the molecular beams appears to be determined completely by the thermalization process by the carrier gas.

### 3.4.3. Optimisation of the beam

There are a few critical parameters that govern the intensity of the beam: the energy of the ablation laser beam, the timing between the valve opening and the Nd: YAG Q-switch firing, the target position and the backing pressure of the carrier gas. These optimisation scans were done on the SrF molecular beam from the source.

Fig 3.8(a) shows the fluorescence signal plotted versus the Nd:YAG laser light ablation energy. The signal has a maximum for ablation energy of around 35 mJ. For a spot size of 4 mm in a 10 ns long pulse, this corresponds to an intensity of 28 mW/cm<sup>2</sup>. For energies below 15 mJ, no signal is produced because the energy of the laser is not enough to ablate the target. Too much YAG energy causes a reduction in the signal, as the gas pulse can only capture a critical density of ablation products and beyond which the more metal ablation products only damage the gas pulse.

Fig 3.8(b) shows the fluorescence signal as a function of the timing between the valve and Q-switch trigger. The optimum value for this parameter was found to be 110  $\mu$ s. This time-delay depends on the distance of the metal target from the valve opening which was ~

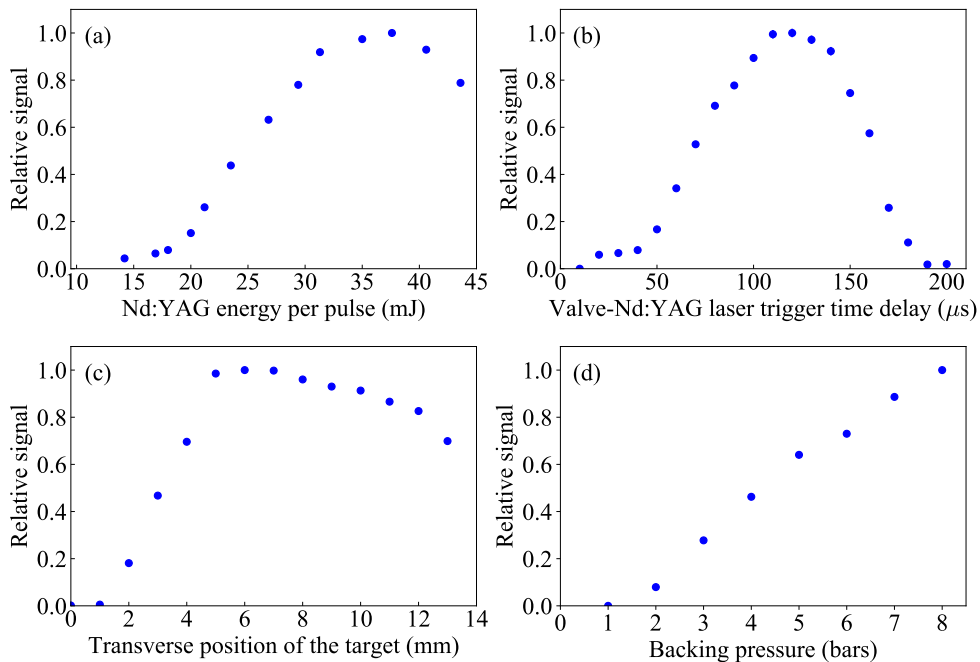


**Figure 3.8** | Relative SrF signal detected on exciting the molecules on the transition  $A^2\Pi_{1/2} (\nu = 0, J = 1/2) \leftarrow X^2\Sigma^+ (\nu = 0, N = 1)$  as a function of (a) Nd:YAG laser light ablation energy, (b) Timing delay between valve and Nd: YAG laser trigger, (c) position of the target perpendicular to the molecular beam axis and (d) backing pressure of the carrier gas. The statistical errors are plotted with the data points, but are very small to be visible.

4 mm in our case.

Fig 3.8(c) shows the SrF fluorescence signal as a function of position of the target in a direction transverse to the beam axis. The optimum transverse distance of the target from the valve opening is  $\sim 5$  mm. In the figure, 0 mm corresponds to the position when the target blocks the beam completely and destroys the gas pulse leading to no beam.

Fig 3.8(d) shows the SrF fluorescence signal as a function of carrier gas stagnation pressure. The signal intensity increases with the increase in the stagnation pressure, with the maximum pressure applied limited to 8 bar due to the limitation of the pressure reducer. The effects of the increase of the backing pressure on the properties of the beam will be discussed in detail in the following section 3.4.4.

All these optimisation scans have been done for a relatively new target. So, these parameters were only meant to be the starting point for producing an intense beam out of the source, specifically the optimised value for the ablation laser powers. On the time-scale of minutes or hours, the optimal ablation energy increases because the target starts deteriorating. Increasing the ablation laser energy increases the signal at the expense of an increase in the

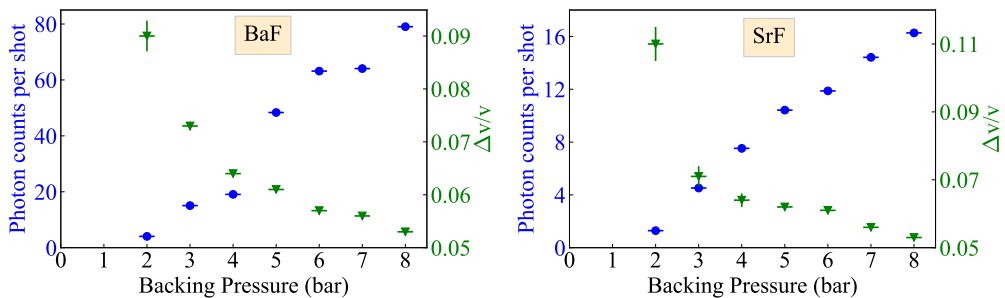


**Figure 3.9** | Average photon counts detected per shot on exciting the (a) BaF and (b) SrF molecules on the transition  $A^2\Pi_{1/2}$  ( $\nu = 0$ ,  $J = 1/2$ )  $\leftarrow X^2\Sigma^+$  ( $\nu = 0$ ,  $N = 1$ ) (blue circles) and the relative velocity spread (green triangles) as a function of backing pressure.

temperature of the beam because products ablated off the metal target surface are hotter.

In addition to these parameters, we also varied the percentage of  $\text{SF}_6$  seeded in the carrier gas. We figured out that we need to seed very little  $\text{SF}_6$  into the carrier gas to produce an intense beam of SrF, with the optimum value varying between (0-2)%. We, once evacuated the entire carrier gas bottle and refilled it only with Ar (without any  $\text{SF}_6$ ). We, however, still detected a signal for SrF molecules, perhaps due to the  $\text{SF}_6$  gas sticking to the walls of the gas bottle.

#### 3.4.4. Backing pressure variation

The relative velocity spread of the molecular beam typically depends strongly on the backing pressure. This is studied by varying the backing pressure from 2 bars to 8 bars, as shown in Figure 3.9. The average photon counts per shot, which is defined as the difference of signal counts and background counts divided by the total number of shots, increases with increasing backing pressure both for SrF and BaF up to 8 bars, which is the maximum pressure applied to our gas supply line. The increase in the photon counts per pulse with increased backing pressure is due to an increase in the number of BaF and SrF molecules. The increase in the BaF and SrF molecules can, in turn, be attributed to an increase in the barium and strontium atoms, respectively entrained in the carrier gas flow at the high backing pressures. The velocity spread of the BaF beam  $\Delta v$  reduces to the minimum value of 32.9(2) m/s corresponding to a relative velocity spread  $\Delta v/v$  of 0.054(9) at a backing pressure of 8 bars. The relative velocity spread for SrF is also lowest at our applied highest backing pressure of 8 bars, with a velocity spread and relative velocity spread of 31.5(3) m/s and 0.053(11), respectively.

#### 3.4.5. Rotational temperature

The rotational spectrum for the transition from the lowest rotational levels of the  $X^2\Sigma^+$  ( $\nu = 0$ ) state to the first electronically-excited state  $A^2\Pi_{1/2}$  ( $\nu = 0$ ) in BaF is obtained by scanning the laser frequency from (11630.38 to 11631.00)  $\text{cm}^{-1}$  (Figure 3.10). The spectrum

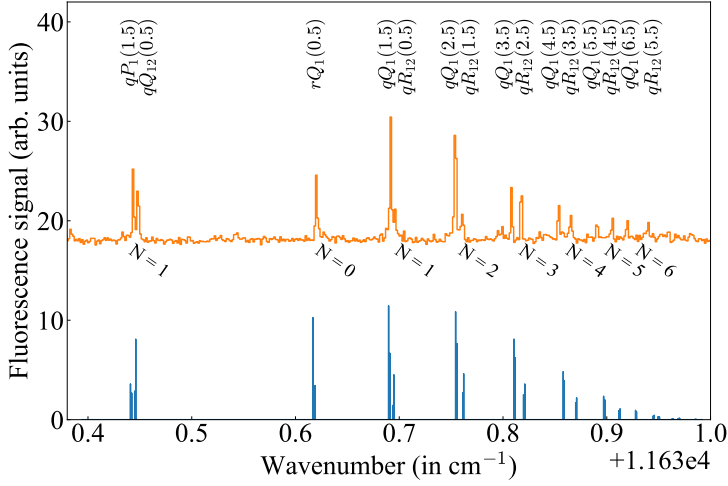


**Figure 3.10** | Rotational spectrum for the transition from  $X^2\Sigma^+(v=0)$  to  $A^2\Pi_{1/2}(v=0)$  state in BaF. The upper trace (orange) is a measured spectrum at a backing pressure of 7 bar. An offset has been added to the upper trace for the purpose of clarity. The lower trace (blue) is given for reference and it has been calculated using program PGOPHER [215] with  $T_{rot} = 3.5$  K.

taken at backing pressure 7 bars is the upper trace and the stick spectrum below is simulated by program PGOPHER [215] using the molecular constants of the  $A^2\Pi_{1/2}$  state [180, 187].

The simulated spectrum corresponds to a rotational temperature of 3.5 K and it is similar in the intensity ratios of the rotational levels to the experimental spectrum. The highest molecule population is in the  $N = 1$  rotational state, followed by  $N = 2$  and  $N = 0$ . Below the rotational temperature of 3 K, the molecule population in  $N = 2$  is lower than the population in  $N = 0$  and above the rotational temperature of 4 K, the molecule population in  $N = 2$  is larger than the population in  $N = 1$ . Hence, the rotational temperature of the BaF beam is estimated to be 3.5(5) K.

### 3.4.6. Number of molecules

The number of molecules in the beam after the skimmer can be estimated using the formula below

$$N = \frac{S}{QE \times T \times (\Omega/4\pi) \times n} \times \frac{\pi \times (\Delta y/2)^2}{w \times \Delta y} \times \frac{M \times \Delta y}{a}, \quad (3.4)$$

where  $S$  is the maximum signal photons counts per shot detected by the PMT,  $QE$  is the quantum efficiency of the PMT at the specific wavelength,  $T$  is the transmission of the fluorescence collection lenses and filter,  $\Omega$  is the collection solid angle,  $n$  corresponds to the average number of photons that are scattered by a single molecule calculated from the hyperfine branching ratios [216, 217]. The second term in the multiplication denotes the fraction of molecules detected by the laser beam in the transverse direction where  $\Delta y$  is the

transverse spread of the molecule beam, and  $w$  is the spot size of the detection laser beam. The third term in the multiplication takes into account the fraction of the fluorescence imaged onto the active area of the PMT, where  $M$  is the magnification of the collection optics and  $a = 5$  mm is the size of the active area of the PMT. All these parameters for the detection of SrF and BaF beams are specified in Table 3.1.

The collection solid angle,  $\Omega$  for a lens of radius,  $r$  placed at a distance,  $d$  from the LIF point can be calculated to be

$$\Omega = 2\pi \left( 1 - \frac{d}{\sqrt{r^2 + d^2}} \right). \quad (3.5)$$

The solid angle in the case of BaF and SrF is therefore calculated to be 0.42 (from upward direction) and 1.17 (from upward and downward direction).

Parameter	SrF	BaF
$S/pulse$	50	100
$QE$	0.39	0.13
$T$	0.73	0.35
$n$	5	1
$\Delta y$ (mm)	10.4	10.4
$w$ (mm)	1	1
$r$ (mm)	12.7	25.4
$d$ (mm)	27.3	65.7
$\Omega$	1.17	0.42
$M$	1.7	0.5
$N/pulse$	$1 \times 10^4$	$6 \times 10^5$
$N/pulse/sr$	$1 \times 10^7$	$6 \times 10^8$

**Table 3.1** | The value of the detection parameters for SrF and BaF involved in the calculation of the number of molecules.

Substituting the detection parameter values for SrF and BaF from Table 3.1 into Equation 3.4, we calculate that we have  $\sim 6 \times 10^5$  BaF molecules per pulse and  $\sim 1 \times 10^4$  SrF molecules per pulse in the  $X^2\Sigma^+$  ( $v = 0$ ,  $N = 1$ ) state in the respective molecular beams after the skimmer accurate to within a factor of 2. The uncertainty on the molecule numbers is mostly due to the uncertainty on the numbers of photons scattered per molecule. The molecules per pulse per steradian can be calculated with respect to the nozzle exit, which is at a total distance of  $R = 58$  cm from the LIF detection point.

The molecules per pulse is divided by a total factor of  $4\pi (\Delta y/2)^2/R^2$ , to give  $6 \times 10^8$  and  $1 \times 10^7$  BaF and SrF molecules per pulse per steradian in the  $X^2\Sigma^+$  ( $v = 0$ ,  $N = 1$ ) state accurate to within a factor of 2, respectively. This state for BaF, like for SrF [126, 123], can be laser cooled and Stark decelerated.

The observed difference in the density between BaF and SrF is surprising, given that barium and strontium are chemically very similar. The measurements on BaF were performed after

the SrF measurements. We attribute the difference to the fact that we have put more effort in optimizing the BaF source than the SrF source. This difference is likely caused by differences in target ablation conditions, which were not completely optimised for SrF.

Further, more barium metal ablation products seem to be entrained in the expanding carrier gas of the BaF molecular beam in comparison to the SrF beam at higher backing pressures. The barium ablation products add energy to the expanding gas, which is evident from an increase in the translational velocity of the BaF beam at high backing pressures in Fig 3.7 [218]. The translational velocity of both BaF (604(4) m/s) and SrF (592(4) m/s) molecular beams is also larger than the velocity of the pure argon from a supersonic expansion (570 m/s) for a backing pressure of 5 bars. This fits with the higher density of BaF observed in the molecular beam in comparison to SrF. Another possible explanation for the discrepancy in the molecule numbers between SrF and BaF may be due to the difference in the mass ratio of the molecule and the carrier gas. Heavier molecules tend to bunch near the axis in supersonic expansion, which has been seen in the separation of gas mixtures [219]. A carrier gas with a different mass might change this discrepancy in the molecule number density of BaF and SrF.

### 3.5. Comparison with other work

Molecule with reference	Carrier gas (in K)	Rotational temperature (in K)	Relative velocity spread ( $\Delta v/v$ )
YbF [98]	Xe	3	0.082
BaF [202]	Ar	30	0.070
BaF [192]	Ar	20-50	-
AlF [220]	Ar/Ne	10	-
BaF [this work]	Ar	3.5(5)	0.054(9)
SrF [this work]	Ar	-	0.053(11)

**Table 3.2** | Comparison of supersonic beam parameters for YbF, BaF, AlF and SrF beams from different supersonic sources.

Table 3.2 provides a comparison of the beam properties from this source to other ablation sources used to produce molecular beams of metal fluorides. The relative velocity ratio obtained in our case is lower than that reported for other sources [202, 192, 98]. Two of these other BaF sources also produce beams with much higher rotational temperature (20-50) K (see Table 3.2) in comparison with our BaF source where we have achieved 3.5(5) K rotational temperature. The YbF source has a 3 K rotational temperature, which is comparable to the value obtained in our source [98]. The YbF source uses xenon as the carrier gas, while argon is used for all BaF sources. The beam density of SrF and BaF in this work also compares well with the intensity of the YbF source at a value of  $1 \times 10^9$  molecules per steradian per pulse in a single rotational state. BaF beams have also been created using cryogenic buffer gas sources, resulting in beams with higher intensities in comparison with the beams from supersonic sources but with lower average velocity and larger velocity spread [221, 222]. A total of  $3 \times 10^{11}$  molecules per pulse have been produced for a beam of ThO

molecules from a cryogenic source in the  $X^1\Sigma^1(v=0, N=0)$  state [92, 223].

### 3.6. Outlook

We have demonstrated that with the combination of a pulsed gas beam jet from an Even-Lavie valve with laser ablation of metal atoms, beams of alkaline-earth monofluoride molecules can be produced with a low velocity spread and low rotational temperatures. The velocity spread achieved here is among the lowest measured for SrF and BaF. Despite the difference in mass of SrF and BaF, the relative velocity spread achieved for these two molecules is similar and lower than the relative velocity spread for pure argon in a supersonic expansion. This shows that the molecular beam has completely thermalised with the carrier gas. It reaches the lower limit of motional temperature that can be achieved with this carrier gas. A similar velocity spread might be obtained for even heavier molecules.





# Lifetime measurements of the $A^2\Pi_{1/2}$ and $A^2\Pi_{3/2}$ states in BaF\*

How wonderful that we have met with a paradox. Now we have some hope of making progress.-Niels Bohr

## 4.1. Introduction

Molecular systems, including barium monofluoride (BaF), have received significant attention in the context of experimental investigations of nuclear-spin-dependent parity violation effects [202] and searches for electric dipole moments (EDMs) [82, 84, 209, 38, 90]. For this reason, activity has commenced on molecular structure calculations of BaF [224, 217, 225, 165]. A relevant and experimentally accessible property is the radiative lifetime of electronically excited states. The measurement of lifetimes in cesium [226, 227] for example, in combination with atomic structure calculations, has impacted the interpretation of atomic-parity violation [228]. We present a study of lifetimes in BaF, confirming a significant discrepancy between previous experimental results [229, 230] and a recent calculation [165].

Previous measurements on radiative lifetimes in the BaF molecule have been performed in a resistance furnace using pulsed dye laser light [231, 229, 230]. These measurements were limited by contributions from collisions and background which are not related to the time-dependent fluorescence from molecules. We present a method to determine lifetimes using improved control over pulse length and timing accuracy made possible by current technology, combined with an intense and cold supersonic molecular beam.

---

\*This chapter is based on P. Aggarwal et al., Phys. Rev. A. 100, 052503(2019)

We demonstrate a nearly background-free method for the determination of excited state radiative lifetimes, which are sensitive to the entire spatial extent of the wave functions. In particular, we investigate the  $A^2\Pi_{1/2}(v=0)$  and  $A^2\Pi_{3/2}(v=0)$  states in BaF, which govern the possibility of laser cooling of this molecular system [224, 217, 232, 165]. Our results underline the significance of the observed discrepancy between state-of-the-art calculations and experimentally measured lifetimes and will thus serve as a benchmark for future molecular structure calculations. In addition to the excited states of BaF, this also holds for SrF and CaF molecules, which are prototype species for laser cooling of molecules [126, 128, 129, 91], where similar discrepancies between experimental and calculated lifetimes were found [165].

The measurement is performed on a fast internally cold supersonic molecular beam in vacuum conditions. The molecules are excited by short pulses of resonant laser radiation. Laser-induced fluorescence (LIF) is detected by a photomultiplier tube (PMT) with sub-nanosecond time resolution with respect to the excitation pulse. The accuracy of the timing for the laser pulses and the detection is derived from a GPS-stabilized reference clock. A detailed study of systematic biases is possible in our experiment due to a low rate of background photons in the detection systems and due to simultaneous measurement of the PMT response. The analysis shows that these biases can be controlled to a level of  $10^{-3}$  on the yielded lifetimes.

## 4.2. Method

Metal fluoride molecules, such as BaF, can be produced efficiently in a supersonic beam source [98, 187, 123, 192]. The molecules are excited to the higher electronic state by short laser pulses (see Fig. 4.1). The mean lifetime value of the molecules in the excited state is extracted from the fluorescence decay after the laser pulses.

The supersonic ablation source operates at a repetition rate of 10 Hz. An Even-Lavie valve [96] creates short ( $\sim 35 \mu\text{s}$ ) pulses of carrier gas, which is a mixture of 98% argon (Ar) and 2% sulphur hexafluoride ( $\text{SF}_6$ ). The disc-shaped barium metal target is mounted inside the vacuum chamber at a distance of 6 mm perpendicular to the supersonic beam. Barium atoms are ablated by 10 ns long pulses from a Nd:YAG laser, with an energy of 20 mJ at a wavelength of 532 nm. The ablation products are entrained in the carrier gas and react with  $\text{SF}_6$  to form BaF molecules which cool in the supersonic expansion. The molecular beam then passes through a skimmer of diameter 4 mm, located 28 cm downstream of the valve, and enters a second chamber where the molecules are detected by LIF.

The detection laser light is generated from the continuous wave (CW) output of a Ti-Sapphire laser. Pulses are created from this light by selecting the first order diffracted beam from an acousto-optic modulator (AOM, Brimrose TEM-200-50) powered by radio frequency (RF) at 200 MHz. The pulse structure and amplitude are controlled by switching the RF (Mini-Circuits ZASWA-2-50-DR+) to obtain pulses which are synchronized to interact with the passing molecular pulse. The fraction of the first-order diffracted light beam in the fundamental Gaussian mode is coupled into a 50 m long single-mode optical fibre, before sending it to the supersonic beam setup.

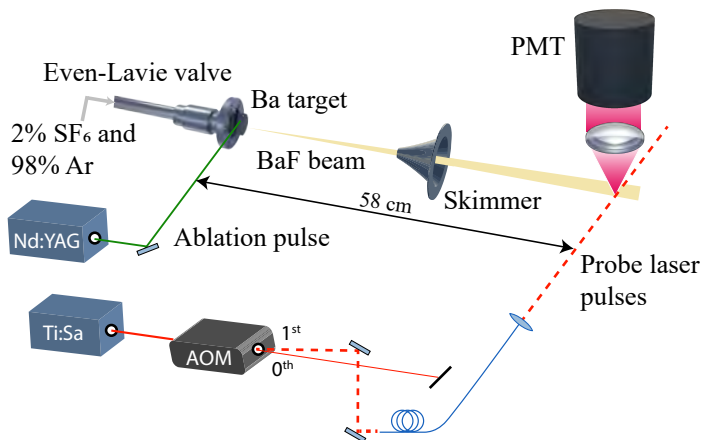


**Figure 4.1** | Schematic overview of the experimental setup. BaF molecules are produced in a supersonic source and pass through a skimmer into the interaction region. Pulses are generated from the CW light of a Ti-Sapphire (Ti:Sa) laser using the first-order diffracted beam from an acousto-optic modulator (AOM). The light from the Ti:Sa laser is delivered to the molecular beam via a 50 m single-mode optical fibre.

The laser pulses intersect with the molecular beam perpendicularly, exciting molecules on the  $A^2\Pi_{1/2}$  ( $\nu = 0$ ,  $J = 1/2$ )  $\leftarrow X^2\Sigma^+$  ( $\nu = 0$ ) (860 nm) or  $A^2\Pi_{3/2}$  ( $\nu = 0$ ,  $J = 3/2$ )  $\leftarrow X^2\Sigma^+$  ( $\nu = 0$ ) (815 nm) electronic transition. The fluorescence emitted is collected by a 2 inch diameter achromatic lens with a focal length of 75 mm, which focuses the light onto an infrared-sensitive PMT (H7422-50 Hamamatsu) with an active area of 5 mm diameter. A narrow bandpass filter with 60% transmission at the resonance wavelength selects fluorescence photons. The detection chamber is internally blackened with paint that absorbs infrared light (AZ Technology MLS-85-SB) in order to reduce the background count rate. The cooled PMT has a count rate of about  $30 \text{ s}^{-1}$  from thermionic emission and of  $2000 \text{ s}^{-1}$  for CW laser light of power 1 mW passing through the interaction zone.

A pulse train is generated with a period of  $2 \mu\text{s}$ , a duty cycle of 2%, and a pulse length of 40 ns. Since the duration of the excitation pulse is comparable to the lifetime of the excited state, the Fourier-limited bandwidth of the pulses is comparable to the linewidth of the employed transitions.

The 100 ms time period between two molecular pulses is split into 50 ms with the pulse train and 50 ms without laser light. The former permits the determination of the laser pulse parameters, while the latter determines the dark count rate of the PMT. The molecules arrive at the interaction region around 1 ms after the laser ablation pulse (Fig. 4.2(a)). On timescales of tens of nanoseconds the response to excitation laser pulses (Fig. 4.2(c)) and the molecular fluorescence (Fig. 4.2(b)) is observed. The arrival time of each photon is recorded by a multihit-capable time to digital converter (Signadyne, SD-TDC-H3344-PXIe). Accurate timing synchronization is achieved by referencing all timing units to a GPS disciplined

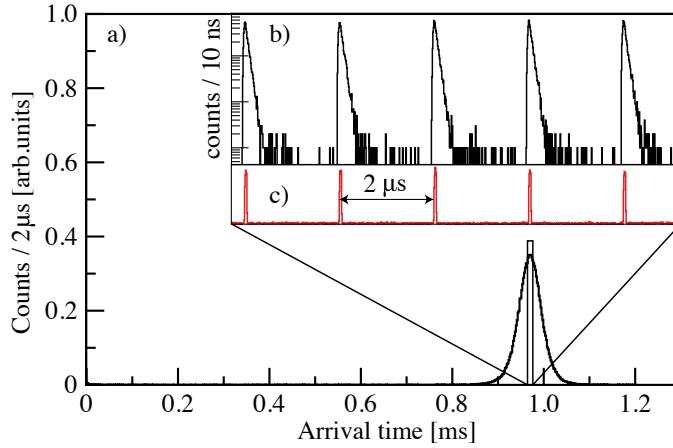


**Figure 4.2** | Time-of-flight profile showing the accumulated fluorescence of the BaF molecular beam following excitation on the  $A \leftarrow X$  transition. The histogram in panel a) shows the arrival-time distribution of the molecular beam fluorescence, binned at  $2 \mu\text{s}$ . Panel b) shows the decay of the fluorescence following excitation by  $40 \text{ ns}$  laser pulses [shown in panel c)] at repetition rate of  $500 \text{ kHz}$ , reflecting the lifetime of the  $A^2\Pi_{1/2}$  state.

$10 \text{ MHz}$  Rubidium Frequency Standard ( $\Delta\nu = 10^{-12}$  in  $2000 \text{ s}$ , FS725 Stanford Research Systems).

The molecular beam has a velocity of  $(594 \pm 18) \text{ ms}^{-1}$  corresponding to a travel of  $60 \mu\text{m}$  in  $100 \text{ ns}$ . Up to  $100$  photons per ablation shot are detected with cw detection laser light with a power of  $2 \text{ mW}$  and a  $1/e^2$  diameter of  $\leq 4 \text{ mm}$ . The vast majority of the molecules are therefore excited in a volume small compared with the detection volume (set by the PMT active area of  $5 \text{ mm}$ ). A systematic bias on the measured lifetime due to molecules traveling out of (or into) the detection volume is therefore negligible.

The timing parameters of the laser pulses are measured simultaneously with the same data acquisition system as the molecular signal. The fall time (between  $90\%$  and  $10\%$  of the amplitude) of the laser pulses is additionally measured with a fast photodiode ( $2 \text{ GHz}$  bandwidth) on an oscilloscope to be  $11(1) \text{ ns}$ . The ratio of the light intensity during the laser pulse to the intensity in the following several hundred nanoseconds, is determined to be larger than  $1000:1$ .

### 4.3. Results

In single-photon counting with PMTs, each pulse has  $\sim 1\%$  probability to be followed by a second pulse (afterpulse) [233, 234, 235]. These afterpulses cause the main systematic bias in our low-background experiment. The employed multihit-capable data acquisition system permits quantitative recording of the time distribution of these pulses (see Fig. 4.3) throughout all data taking periods for the lifetime measurements. The distribution of these

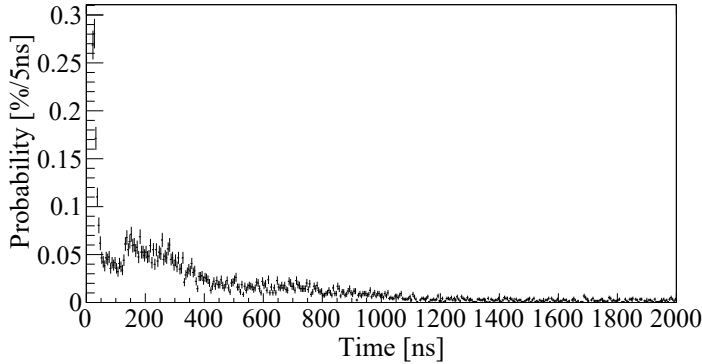


**Figure 4.3** | Time distribution of the probability of a second photon in a time window of 2000 ns. This spectrum is extracted from the same dataset as the fluorescence data for the determination of state lifetimes.

pulses ranges over timescales of microseconds with a structure comparable to the LIF signal. This contribution, although small, is taken into account in the determination of the excited state lifetimes.

The time distribution  $N(t)$  of the number of photons recorded at time  $t$  after the trailing edge of the excitation laser pulse is described by

$$N(t) = \frac{A}{\tau} e^{-t/\tau} + B(t) + C, \quad (4.1)$$

where  $A$  is the number of photons recorded in the exponential decay,  $\tau$  is the lifetime of the excited state,  $B(t)$  is the convolution of the distribution of afterpulses (Fig. 4.3) with the distribution  $N(t)$ , and  $C$  is a constant offset due to background counts. The uncertainties on the counts per channel arise from Poissonian statistics.

A maximum likelihood fitting procedure of the function given in Eq. 4.1 to the experimental data yields a value of  $\tau_{\Pi_{1/2}} = 57.1(3)$  ns for the lifetime (Fig. 4.4). The contribution of the time dependent term  $B(t)$  is 1.6 % of the total statistics. Not taking  $B(t)$  into account leads to a bias of 1.6 ns on the lifetime, which is five times larger than the statistical uncertainty.

On average, three photons per molecular pulse ( $\bar{n} = 3$ ) were recorded. For a quarter of these molecular pulses, exactly 1 photon ( $n = 1$ ) was recorded. In this subset of the data, there is no contribution from afterpulses. The resulting spectrum is therefore analyzed with the model function Eq. 4.1 with the contribution  $B(t)$  set to zero (see Fig. 4.5). For the  $A^2\Pi_{1/2}$  state, the lifetime  $\tau_{\Pi_{1/2}, n=1} = 57.1(5)$  ns. This number is in excellent agreement with the result obtained with the full dataset. The same analysis method applied to the recorded time spectra for the  $A^2\Pi_{3/2}(\nu = 0)$  state yields the lifetime  $\tau_{\Pi_{3/2}, n=1} = 47.9(6)$  ns (see Fig. 4.5).

The magnetic field in the measurement region has been determined to be  $< 50\mu\text{T}$ . It is directed vertically, coinciding with the observation line of the PMT. The excitation laser light was elliptically polarized. In such a geometry, modulation of the fluorescence from the

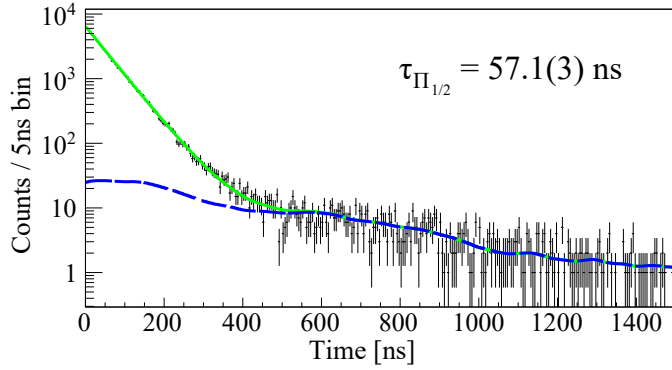


**Figure 4.4** | Accumulated spectrum for the time distribution  $N(t)$  for the  $A^2\Pi_{1/2}(\nu=0)$  state. A maximum-likelihood fit of Eq. 4.1 to the data is shown by the solid (green) line. The dashed (blue) line indicates the contribution of the time-dependent background  $B(t)$ . A value for the lifetime of  $\tau_{\Pi_{1/2}} = 57.1(3)$  ns is obtained.

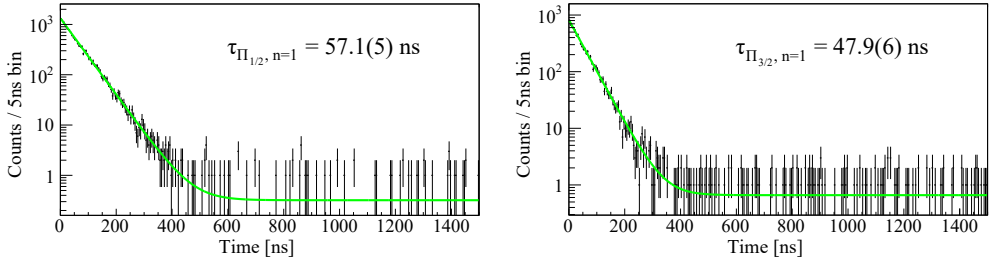


**Figure 4.5** | Accumulated spectrum of the time distribution  $N(t)$  for the  $A^2\Pi_{1/2}$  state (left) and  $A^2\Pi_{3/2}$  state (right), selecting events with one photon per molecular pulse. The yielded lifetimes are  $\tau_{\Pi_{1/2}, n=1} = 57.1(5)$  ns and  $\tau_{\Pi_{3/2}, n=1} = 47.9(6)$  ns.

excited state due to Zeeman quantum beats [226] is strongly suppressed. The estimated periods of the quantum beats are  $0.9 \mu\text{s}$  and  $3.3 \mu\text{s}$  for the  $A^2\Pi_{3/2}$  and the  $A^2\Pi_{1/2}$  state, respectively.

Systematic bias on the measurement due to the excitation light pulse parameters was checked by variation of the duty cycle between 1% and 20% and of the repetition period between  $1 \mu\text{s}$  and  $10 \mu\text{s}$ . From a systematic scan of the start time for the fitting procedure in Fig. 4.4, we find that the variation of the lifetime value is one order of magnitude smaller than the statistical uncertainty. Similar size contributions are observed for subsets of the data with different excitation probabilities due to a change in laser power or drift of the excitation laser frequency.

The measured lifetime values are listed with previous experimental work [229, 230] and recent quantum chemistry calculations [165, 224] in (Table 4.1). The lifetimes of the excited states of BaF were calculated using the multireference configuration interaction approach in

a nonrelativistic framework (NR-MRCI) [224], thus yielding the same result for the  $A^2\Pi_{1/2}$  and the  $A^2\Pi_{3/2}$  states. In a more recent investigation [165], we used relativistic MRCI, where the traditional 4-component Dirac-Coulomb (DC) Hamiltonian was replaced by the exact 2-component Hamiltonian (X2C-MRCI) [236, 237]. In both works, experimental level energies were used along with calculated transition dipole moments to determine the lifetimes. The X2C-MRCI results reproduce the lifetime ratio very well, as a result of the accurate treatment of spin-orbit effects. However, the predicted lifetimes underestimate the experimental values by about 30%, due to the shortcoming of the MRCI approach in the treatment of the transition dipole moments (TDMs). The quality of the calculated TDMs is highly sensitive to the level of treatment of electron correlation, and a multireference coupled-cluster approach, such as the Fock-space coupled cluster (FSCC)[238] is expected to yield higher-accuracy results. An implementation that will allow use of FSCC for TDM calculations is presently under way.

Method	Lifetime [ns]	
	$A^2\Pi_{1/2}$	$A^2\Pi_{3/2}$
Supersonic beam (this work)	57.1(3)	47.9(6)
Resistance furnace	56.0(9) [230]	46.1(9) [229]
X2C-MRCI	40.4 [165]	34.7 [165]
NR-MRCI	37.8 [224]	

**Table 4.1** | Experimental and theoretical values for the lifetime of the  $A^2\Pi_{1/2}$  and  $A^2\Pi_{3/2}$  states. The theoretical values were obtained in the framework of NR-MRCI and X2C-MRCI methods.

The main decay channel of the investigated excited states is an electric dipole transition to the  $X^2\Sigma^+(\nu = 0)$  ground state. In this case, scaling of lifetimes is expected to be proportional to the third power of the fluorescence wavelength ( $\lambda^3$ ) ( $\lambda = 859.79$  nm and  $\lambda = 815.45$  nm for the  $A^2\Pi_{1/2}$  and  $A^2\Pi_{3/2}$  states, respectively). We compare the ratio of the lifetimes of the two excited states with the previously measured experimental work [229, 230], the X2C-MRCI theoretical calculations, and the expected value from  $\lambda^3$ -scaling. Within the experimental accuracy, our experimental result is in agreement with this scaling (Table 4.2).

Method	Lifetime ratio
This work	0.839(14)
$\lambda^3$ -scaling	0.8531
Resistance furnace [229, 230]	0.823(25)
X2C-MRCI [165]	0.859

**Table 4.2** | Comparison between the ratios of the lifetimes  $\tau_{\Pi_{3/2}}/\tau_{\Pi_{1/2}}$  obtained in this work, previously measured experimental work [229, 230], and the X2C-MRCI theoretical calculations with the expected value from  $\lambda^3$ -scaling of the transition wavelengths.

## 4.4. Conclusion

A measurement of the lifetimes of the low lying electronically excited  $A^2\Pi_{1/2}$  and  $A^2\Pi_{3/2}$  states in the BaF molecule was performed in the context of the experimental search for a permanent electric dipole moment of the electron (NL-eEDM) [90]. The statistically limited accuracies on the lifetimes of the  $A^2\Pi_{1/2}$  and  $A^2\Pi_{3/2}$  states are 0.5% and 1.3%, respectively. The main systematic uncertainty arises from the imperfection of photomultipliers in photon counting mode, in particular their afterpulses. By measurement of the afterpulse spectrum of the employed PMT, the relative contributions to the measured lifetime values could be reduced to the  $10^{-3}$  level. Methods which permit identification and control of systematic effects are crucial in precision measurements and their interpretation. Careful design of the experimental procedure and the use of state-of-the-art technology enables the execution of such measurements with low sensitivity to systematic bias.



# 5

## Deceleration of SrF molecules in a 4 m long decelerator

What we usually consider as impossible are simply engineering problems... there's no law of physics preventing them.-Michio Kaku

Over the last two decades, there has been immense progress in the production, deceleration and trapping of molecules. This progress is motivated by a wide range of significant applications [239]. Cold molecules have been used to test fundamental physics [228, 240], studying collision at low energies [241, 242], simulating many-body quantum systems [243], processing quantum information [244] and studying quantum chemistry [245]. The production of cold molecules can be mainly categorised in indirect and direct methods. In the indirect approach, the molecules are assembled from ultracold atoms using electric, magnetic and optical fields, a technique restricted to the production of cold bi-alkali molecules [246]. In the direct approach, the controlled interaction with external electric, magnetic and optical fields are used to produce translationally cold and slow molecular beams. This has been achieved with the techniques of cryogenic buffer gas cooling, laser cooling, Stark and Zeeman deceleration.

In a conventional Stark decelerator, a spatially inhomogeneous electric field distribution acts as an effective trap for the molecules. At a given time, the even-numbered electrode stages inside the decelerator are switched to high voltage and the odd-numbered stages are grounded. Molecules in the low field seeking states approaching the plane of the first electrode experience the increasing electric field as a potential hill and lose kinetic energy on the upward slope of the potential hill. To avoid the acceleration of the molecules on the downward slope of the potential hill, the voltages on the first electrode are switched off and on the adjacent electrode is switched to high voltage (see section 1.5.2, Chapter-1 for details). The first molecule to be decelerated from a supersonic source in a Stark decelerator were CO molecules in 1999 [105]. Since then, this technique has been applied to several neutral molecules [114, 115] (see section 1.5.2). Deceleration of beams of O<sub>2</sub> [117], CH<sub>3</sub> [118] and

He<sub>2</sub> [119] was later demonstrated in a Zeeman decelerator. Stark and Zeeman deceleration require the molecule to have a non-zero electric or magnetic moment, respectively, with a favourable Stark/Zeeaman curve.

Recently, the production of beams with a relatively lower longitudinally velocity in comparison to supersonic beams was achieved by collisions with a cold buffer gas in a cell in a cryogenic buffer-gas source [101]. The combination of buffer gas cooling and laser cooling has been effective in decelerating molecules to a standstill. However, laser cooling can only be applied to a handful of molecules with favourable Frank Condon factors. In 2012, slowing and trapping of a cryogenically-cooled beam of SrF were demonstrated using radiation pressure [127]. Since then, YO and CaF molecules have also been slowed and trapped in a MOT [129, 247, 130, 135] with a similar combination.

A cryogenic source, so far, has not yet been combined with a Stark decelerator. Only beams of light molecules from supersonic sources with a high longitudinal velocity (350-600) m/s have been decelerated in Stark decelerators. This chapter will cover the results of the guiding and deceleration of SrF molecules produced in a cryogenic source using a 4 m long traveling-wave Stark decelerator (TWSD). In a TWSD, we use truly three-dimensional electric field traps to decelerate the molecules, which is in contrast to a conventional Stark decelerator [120].

## 5.1. Operational principle of a traveling-wave Stark decelerator

This section gives a brief account of the operational principle of the TWSD. A detailed description can be found in [120, 248, 249, 121]. A spatial sine-modulated electrostatic potential is applied to an array of ring electrodes to create an electric field distribution on the inside of the array with two on-axis minima in the field magnitude per spatial period. These minima act as truly three-dimensional traps for polar molecules in a low field seeking state. The required potential on the individual electrodes is given by the following expression:

$$V_n(t) = V_0 \sin \left( \phi(t) + \frac{2n\pi}{N} \right), \quad (5.1)$$

where  $V_0$  is the amplitude of the waveform applied and  $n = 1, 2, \dots, N$  for the set of  $N$ -ring electrodes and  $\phi(t)$  is the time-dependent phase offset. The electrode-dependent shift is determined by the periodicity  $N$  of the specific array. In our decelerator,  $N = 8$ , which corresponds to an effective shift of  $\pi/4$  between adjacent electrodes. When  $\phi(t)$  is constant, there is a static array of electric field minima on the molecular beam axis. This potential can be moved along the axis of the ring electrodes by varying  $\phi(t)$  linearly with time. On increasing the  $\phi(t)$  linearly with time, the traps are moved at a constant speed along the decelerator axis. The time-dependence of the phase offset is given by:

$$\phi(t) = 2\pi \int_0^t f(\tau) d\tau \quad (5.2)$$

where  $f(\tau)$  is the modulation frequency of the voltage on each individual electrode. The modulation frequency can be linked to the instantaneous velocity of the traps as  $Lf(\tau)$

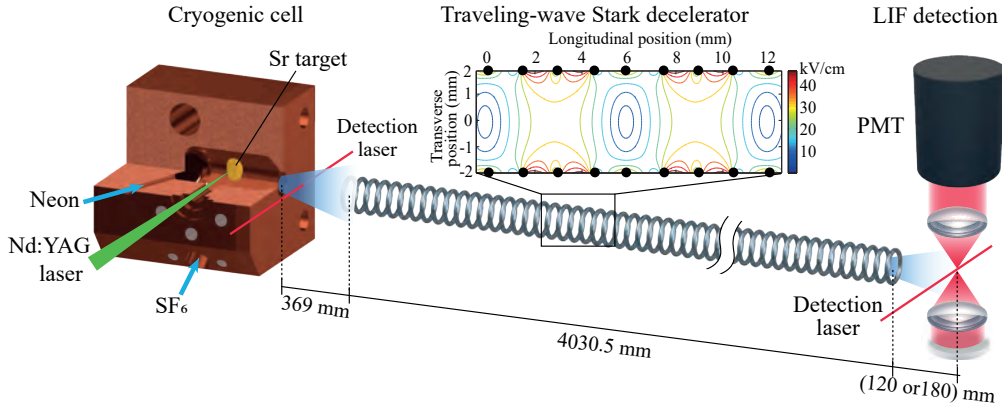


**Figure 5.1** | *Experimental setup.* The SrF molecules are produced in a cryogenic buffer gas source. A high-energy pulsed Nd:YAG laser ablates strontium from the metal target. The molecules react with SF<sub>6</sub> gas to produce SrF, which is then cooled by collisions with cold neon gas inside the cell. After exiting from the cell, some of the molecules enter the TWSD, which is positioned at a distance of 36.9 cm from the molecular source exit. The molecules leaving the decelerator are detected by laser-induced fluorescence at a distance of 12/18 cm from the last ring electrode in the TWSD.

where  $L$  is the period length. A constant  $f(\tau)$  can be used to guide the molecules trapped in the electric field minima at a selected velocity through the decelerator. Chirping  $f(\tau)$  leads to acceleration or deceleration of the traps.

## 5.2. Experimental set-up

The experimental setup consists of three sections: the molecular source, the 4 m long Stark decelerator and the laser-induced fluorescence (LIF) detection system as shown in Figure 5.1.

### 5.2.1. Molecular source

SrF molecules are produced in a pulsed cryogenic buffer gas source which operates at a repetition rate of 10 Hz. This technique has already been used for the production of many other molecules [250, 251, 92, 252]. This source was developed by another Ph.D. student while I was working on the supersonic source. A detailed account of the source can be found in [253]. Here, I give a brief account of the source. The SrF molecules are produced inside a copper cell, which is cooled using a pulse-tube cryocooler to an adjustable temperature in the range of (17-20) K. The design of the cell is adopted from [252]. The strontium metal target mounted inside the cell is ablated by a pulsed Nd:YAG laser in the presence of the SF<sub>6</sub> gas. The target mounted inside the cell is rotated to provide a fresh spot for ablation. SF<sub>6</sub> flows inside the cell continuously at a flow rate of 0.5 sccm. Neon gas also flows into the cell through a copper tube which is connected to the cryocooler, which cools the gas to 20K. The flow rate of neon inside the cell is (8-12) sccm. The SrF molecules produced

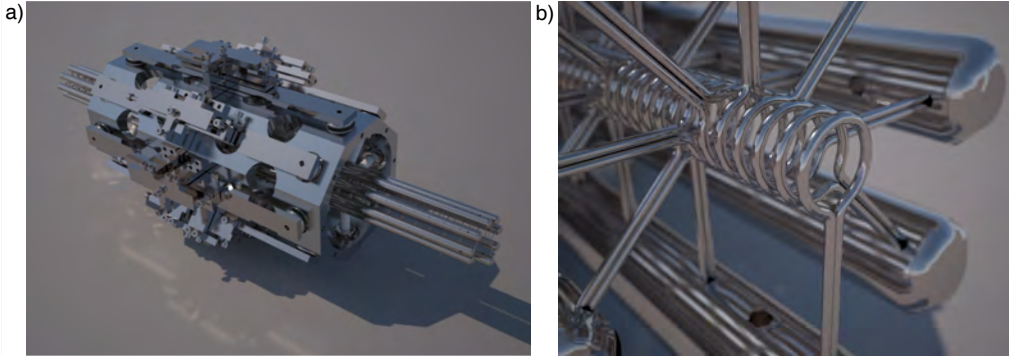


**Figure 5.2** | (a) A 3D computer rendered image of one TWSD module with the alignment mechanism. (b) A magnified image of the ring electrodes at the end of the last module.

inside the cell thermalise by undergoing collisions with the cold neon gas. The thermalised molecules then exit the cell via a 5 mm wide aperture. The cell is surrounded by a copper and an aluminium cylinder on the outside to prevent the thermal radiation to heat the cell.

### 5.2.2. Design of Traveling-wave Stark decelerator

Our Stark decelerator consists of modules, each of which contains a total of 336 ring-electrodes made of tantalum. One of the modules and its magnified image is shown in Figure 5.2. Each module consists of eight rod electrodes arranged in an octahedral fashion. Each rod electrode holds 42 ring electrodes which are equally spaced by 12 mm. Each ring electrode has a diameter of 4 mm and a thickness of 0.6 mm. The periodicity of the ring electrodes from the eight rod-electrodes leads to a total separation of 1.5 mm between the ring electrodes. The results presented in this chapter are for the guiding and deceleration of cryogenically buffer gas cooled beam of SrF molecules in a 4-m long decelerator with a total of 8 modules, each 0.54 m long, connected electrically and mechanically.

The sine-wave potential applied on each ring-electrode is generated by an 8-channel arbitrary waveform generator (AWG Acquittek DA8150) with a sampling frequency of 10 MHz. The voltage amplitude, frequency, phase offset of the waveform can be controlled separately by tweaking these parameters in an input text file to the AWG. The amplitude of the voltage amplitude along with the convolution of the Stark shift determines the effective depth of the trap for molecules in a specific energy level. We apply an input sine-wave potential from the AWG generator with a maximum amplitude of  $\pm 5$  V which is amplified using high-voltage (HV) amplifiers developed by Trek Inc. (model PD10039). The amplifiers have a voltage gain of 1000 to amplify the sine-waveform from the AWG, after passing it first through a linear pre-amplifier.

The SrF molecules in the  $\nu = 0$ ,  $N = 1$ ,  $M_N = 1$  are low-field seeking for an electric field lower than 21 kV/cm which corresponds to an electric potential of 5 kV for our design of the decelerator. The HV amplifiers have to deliver the voltage to the rod electrodes as a function of time. The required radial frequency for guiding a cryogenic beam with a typical

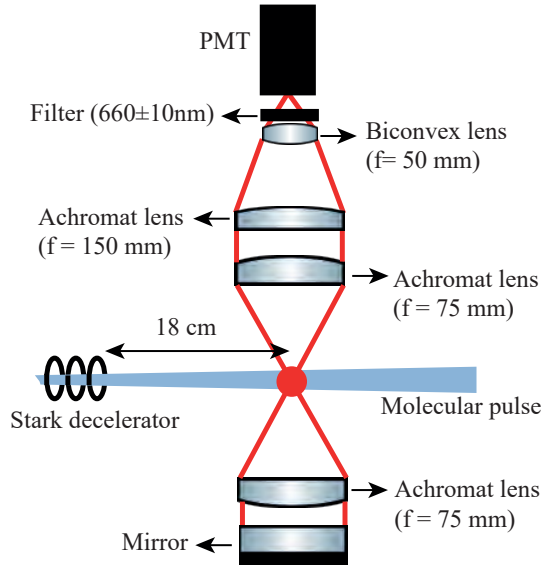


**Figure 5.3** | The optics assembly for the fluorescence light collection. The red dot in the center represents the direction of the detection laser light, which is directed into the plane of the paper. The detection laser light with a spot size of 3.5 mm and a power of 5 mW excites the SrF molecules on the transition  $A^2\Pi_{1/2} (\nu = 0, J = 1/2) \leftarrow X^2\Sigma^+ (\nu = 0, N = 1)$  for LIF detection.

velocity of 190 m/s is  $2\pi \times 16.6$  kHz. For decelerating a beam from an initial velocity of 190 m/s down to 0 m/s, the frequency of the sine-waveform applied to the decelerators has to be chirped down from 16.6 KHz to DC. These amplifiers can deliver a sine-wave up to a bandwidth of 30 kHz. The signal amplified by the HV-amplifiers is applied to the electrodes via vacuum electrical feedthroughs. The signal can be monitored through the control and voltage monitors on each HV-amplifiers.

### 5.2.3. Detection system

The molecules coming out of the decelerator are detected by laser-induced fluorescence detection. A continuous-wave laser beam with a wavelength of 663 nm excites the molecules from the ground electronic state to the first excited electronic state,  $A^2\Pi_{1/2} (\nu = 0, J = 1/2) \leftarrow X^2\Sigma^+ (\nu = 0, N = 1)$ . The hyperfine structure of  $N = 1$  rotational state in the electronic ground state  $X^2\Sigma^+ (\nu = 0)$  is covered by adding sidebands to the detection laser light (see section 3.2). The molecules decay back to the ground state and emit fluorescence, which we collect and detect.

The detection laser light with a power of 5 mW enters the chamber at a right angle to the molecular beam axis at a distance of 12/18 cm from the last ring-electrode of the TWSD. The spot size ( $I/I_0 = 1/e^2$ ) of the detection laser light from the optical fiber is increased by

a factor of 5 to 3.5 mm using a telescope. The fluorescence from the molecules is collected as depicted in Fig. 5.3 in a direction perpendicular to both the molecular beam and the detection laser beam direction by a 2-inch achromat lens with a focal length of 75 mm (back focal length 61.8 mm) in the upward and downward direction. The parallel rays in the downward direction are directed by a plane-mirror back in the upward direction. The total solid angle is 0.93 steradian, corresponding to a collection efficiency of 7.4%. The solid angle is calculated using the formula specified in Equation 3.5, Chapter-3. Another achromat lens with a focal length of 150 mm (back focal length 162 mm) placed after the collection lens, focuses the emitted fluorescence at a point outside the detection chamber from where it is re-focused on a photo-multiplier tube by a 1-inch lens of focal length 50 mm for a virtual object distance of -80 mm. The total magnification of the lens assembly is  $\sim 1$ . A single-band interference filter (Semrock FF01-661/20-25) with a frequency centered on 660 nm with a bandwidth of 20 nm prevents the light other than the resonant light from entering the PMT (active area = 5 mm  $\times$  5 mm) preventing an increase in the background counts due to the room light. More details on the PMT used for the detection is discussed in section 3.3, Chapter-3.

## 5.3. Results

In this section, we present the absorption signal corresponding to the SrF beam from a cryogenic source. This will be followed by the experimental results for the guiding and deceleration of a beam of SrF molecules from a cryogenic source in a 4 m long TWSD. The decelerator data presented as time-of-flight profiles have been analysed using a python-based script and represented in the form of time-of-flight profiles which are one-dimensional binned histograms.

### 5.3.1. Absorption signal of SrF beam from the cryogenic source

Figure 5.4 shows an absorption signal for SrF molecules detected via a photodiode at a distance of 5 mm from the cell exit by exciting the molecules on the 663 nm transition  $A^2\Pi_{1/2} (\nu = 0, J = 1/2) \leftarrow X^2\Sigma^+ (\nu = 0, N = 1)$ . The  $t = 0$  represents the time when a light pulse from the ablation laser ablates the target. The detection laser light used for this absorption measurement had a spot size of 1 mm and a power of 80  $\mu$ W. The signal was measured for a cell temperature of 17 K, neon and SF<sub>6</sub> gas flow rate of 8 sccm and 0.5 sccm, respectively. The hyperfine structure in the  $N = 1$  rotational state of the ground electronic state  $X^2\Sigma^+(\nu = 0, N = 1)$  is addressed by adding sidebands to the detection laser. The molecules are detected 250  $\mu$ s after the ablation of the target. This includes the time for the production of the molecules in the cell, their thermalisation with the neon gas and the time taken by molecules to fly a distance of 5 mm till the detection laser beam. The average longitudinal velocity of the beam from the cryogenic source was calculated to be  $\sim 190$  m/s [253]. We can also estimate the number of molecules in a specific rotational state  $X^2\Sigma^+(\nu = 0, N = 1)$ , which exit the cell using the formula

$$N_a = \frac{A v_{||}}{\Delta x \sigma_D} \int \ln \left[ \frac{P_O}{P_T} \right] dt, \quad (5.3)$$

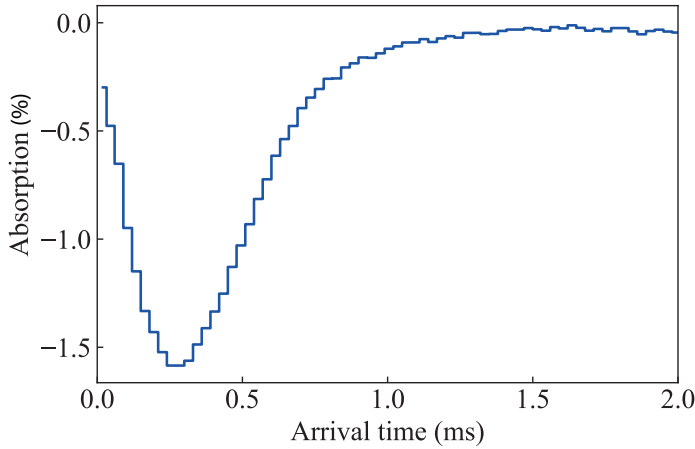


**Figure 5.4** / A typical absorption signal (averaged over 6000 ablation shots) of SrF molecules obtained by exciting them on the transition  $A^2\Pi_{1/2} (\nu = 0, J = 1/2) \leftarrow X^2\Sigma^+ (\nu = 0, N = 1)$  detected at a distance of 5 mm downstream of the cold cell in the cryogenic buffer gas source.

where  $A$  is the cross-sectional area of the molecular beam detected at a distance of 5 mm from the cell exit,  $v_{||}$  is the average longitudinal velocity of the SrF beam,  $\Delta x$  is the absorption path length in the direction of propagation of the detection laser beam,  $\sigma_D$  is the doppler broadened absorption cross-section [254],  $P_T/P_O$  is the ratio of the transmitted power to the initial power of the detection laser beam. The term in the integral is calculated from the absorption signal shown in Figure 5.4. The doppler broadened absorption cross-section can be calculated using the formula [254]

$$\sigma_D = 2\pi\alpha\omega_{ge}|\hat{D}_{ge}|^2 \left[ \frac{\gamma^2}{\Delta^2 + (\gamma/2)^2} \right], \quad (5.4)$$

where  $\alpha$  is the fine-structure constant,  $\omega_{ge}$  is the resonant frequency,  $\hat{D}_{ge}$  is the dipole matrix element for the transition from the  $A^2\Pi_{1/2} (\nu = 0, J = 1/2) \leftarrow X^2\Sigma^+ (\nu = 0, N = 1)$  (in units of Bohr radius,  $a_0^2$ ),  $\Delta = \omega - \omega_{ge}$  is the detuning of the detection laser beam and  $\gamma$  is the spontaneous emission rate and is equal to  $2/\tau$  ( $\tau$  is the lifetime of the excited state) for our energy level structure. The doppler broadened absorption cross-section is calculated to be  $1.4 \times 10^{-15}$  using the detuning ( $\Delta$ ) corresponding to the transverse velocity spread of 80 m/s [216], the lifetime of the excited state equal to 24.1 ns [231] and the dipole matrix element equal to 6 (in units of  $a_0^2$ ) [231].

The typical absorption signal for the data presented in this thesis has maximum amplitude in the range (0.5-2)% as shown in Figure 5.4, which corresponds to a value of the integral in Equation 5.3 varying between  $(2-8) \times 10^{-6}$ . We further assume that the molecular beam has a diameter ( $d$ ) of 4.5 mm (the opening of the cell, a conservative estimate) at a distance of 5 mm from the cell exit. Substituting the velocity of the molecular beam ( $v_{||} = 190$  m/s), the cross-sectional area of the molecular beam ( $A = \pi(d/2)^2 = 1.6 \times 10^{-5}$ ) and absorption path length ( $\Delta x = d = 4.5$  mm) in Equation 5.3, we calculate that the number of molecules

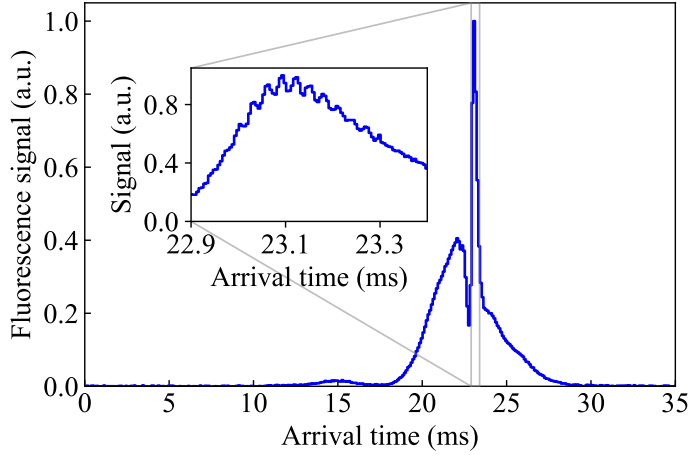


**Figure 5.5** | Experimental time-of-flight profile (integrated over 6000 shots, amplitude normalised, binsize = 100  $\mu$ s) of SrF molecules for 4 m of ac-guiding at a velocity of 190 m/s and at a voltage amplitude of 3 kV. SrF molecules in the  $X^2\Sigma^+$  ( $v = 0, N = 1$ ) energy state are detected at a distance of 18 cm from the last ring electrode. The inset shows a zoom-in of the guided peak (binsize = 5  $\mu$ s). An additional peak substructure is visible which corresponds to the SrF molecules guided in different electric traps of the decelerator. An additional fast component of the guided beam is also visible at an arrival time of 15 ms.

produced by the source lies between  $(1-3) \times 10^9$  per pulse. Limited by the phase-space acceptance of the decelerator and the divergence of the beam after a free-flight distance of 37 cm between the source and the decelerator, only a small fraction of the total molecules enter the decelerator. The fraction of molecules entering the decelerator is estimated later in sections 5.4, 6.2.2. For the current experimental setup, the phase-space acceptance of the decelerator is underfilled.

### 5.3.2. Guiding

The guiding mode of operation is achieved when the electric field traps move with a constant velocity  $v$ , which is selected to match the average longitudinal velocity of the initial distribution from the cryogenic source. Fig. 5.5 shows the normalised time-of-flight (TOF) histogram (binsize = 100  $\mu$ s) of SrF molecules in the rotational state  $N = 1$ ,  $M_N = 0$  at a guiding velocity of 190 m/s and at a voltage amplitude of 3 kV integrated over 6000 shots. The  $t = 0$  corresponds to the time of the laser ablation of the strontium metal target by the Nd:YAG laser in the cold cell. The central narrow peak corresponds to the molecules which are within the longitudinal and transverse acceptance of the decelerator. The two adjacent wings are due to the molecules which are within the transverse acceptance but outside of the longitudinal acceptance of the decelerator. The longitudinal velocity spread of the entire molecular beam packet moving with an average longitudinal velocity of 190 m/s is  $\sim 100$  m/s, calculated from the time spread of the packet of  $\sim 12$  ms, as can be seen in



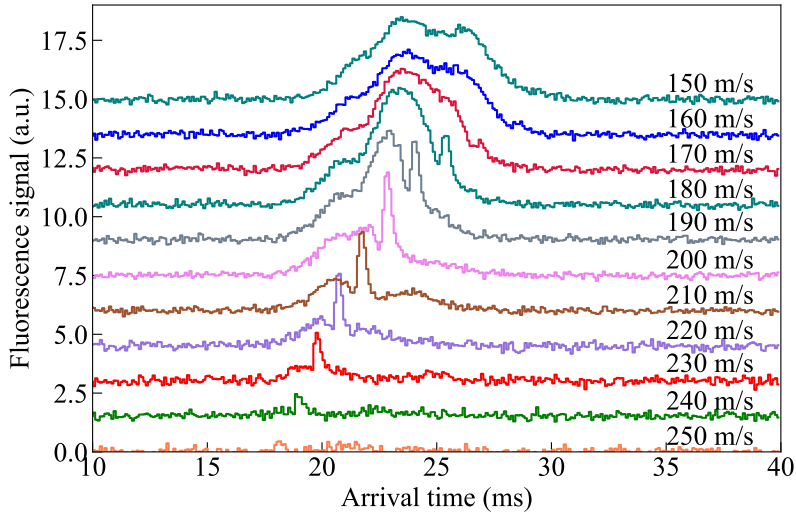


**Figure 5.6** | The time-of-flight profile of SrF molecules (binsize =  $100 \mu\text{s}$ ) guided at different velocities for a maximum voltage amplitude of 3.0 kV applied to the electrode rings. The molecules are detected by exciting them on the transition  $A^2\Pi_{1/2} (\nu = 0, J = 1/2) \leftarrow X^2\Sigma^+ (\nu = 0, N = 1)$  at a wavelength of 663 nm. Each profile is integrated for 3000 shots. The molecules are detected at a distance of 12 cm from the last ring electrode of the decelerator. A vertical offset is added for the sake of clarity.

the time-of-flight profile. The inset of Fig. 5.5 shows a zoom-in of the guided peak, which further has a substructure. The multiple peaks represent the molecules guided along the length of the decelerator in different traps, separated by a distance of 6 mm. The guided molecular packet extends to  $\sim 60$  mm corresponding to the 10 multiple peaks visible in the inset of Fig. 5.5. The individual peaks are not separated well, due to the long free-flight time (18 cm) from the last ring electrode of the decelerator till the point of the LIF detection. The free flight time for molecules in adjacent traps increases by about  $\sim 40 \mu\text{s}$  on average after the electric fields inside the decelerator are switched off.

#### Guiding of SrF at different guiding velocities and voltage amplitudes

Fig 5.6 shows the time-of-flight profile of SrF molecules (accumulated over 3000 shots) when different velocities are selected for guiding. The guiding peak has the maximum amplitude for the guiding velocities between 190-210 m/s. The average longitudinal velocity of the molecular packet can be varied between this range by changing the cryogenic cell source parameters. We, therefore, choose 190 m/s as the guiding velocity for the optimisation of the cryogenic source parameters to get the maximum area under the guided peak at this velocity. The low average longitudinal velocity of the molecules is also desirable, as it will facilitate the deceleration of molecules at low deceleration strengths applied in the decelerator. Simulations were performed in our group to investigate the optimum coupling of a cryogenic source with a Stark decelerator. It was found out the optimum coupling is for a longitudinal velocity of the molecular beam at 190 m/s [255]. The guiding peak is not

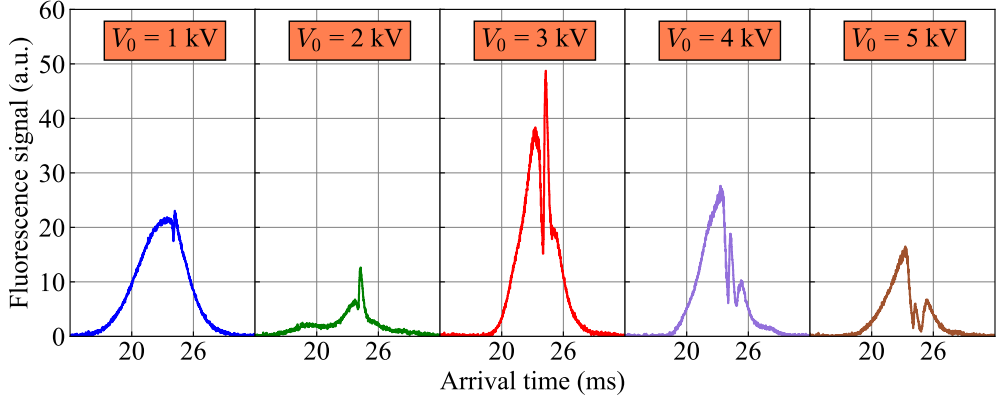


**Figure 5.7** | The time-of-flight of SrF molecules (binsize = 20  $\mu$ s) guided at a velocity of 190 m/s for different maximum voltage amplitudes applied to the ring electrodes. The molecules are detected by exciting them on the transition  $A^2\Pi_{1/2}$  ( $v = 0, J = 1/2$ )  $\leftarrow X^2\Sigma^+$  ( $v = 0, N = 1$ ) at a wavelength of 663 nm. Each profile is integrated for 6000 shots. The molecules are detected at a distance of 18 cm from the last ring electrode of the decelerator.

visible for a guiding velocity below 150 m/s and above 250 m/s, which confirms that the longitudinal velocity spread of the beam is 100 m/s, as was already determined from the time-of-flight profile.

The area under the signal region in the time-of-flight profiles is maximum for the case of guiding velocity of 150 m/s. This can be explained as follows: The voltages on the ring electrodes are switched off when the molecules with the guiding velocity reach the end of the decelerator. For the case of 150 m/s, for the full range of the velocities in the molecular packet (150-240) m/s, the electric fields inside the decelerator are non-zero. For the case of guiding velocity of 240 m/s, the voltages on the ring electrodes are switched off when the molecules with velocity of 240 m/s reach the end of the decelerator. As a result, for molecules with a velocity below 240 m/s, the free-flight distance to the detection point increases. Due to the divergence of these molecules away from the detection point, they are not detected and hence only the synchronous molecules are detected in the time-of-flight profile at a guiding velocity of 240 m/s.

Fig 5.7 shows the time-of-flight profile of SrF molecules at a guiding velocity of 190 m/s for different voltage amplitudes applied to the ring electrodes integrated over 6000 shots. The central guiding peak has maximum amplitude for a voltage amplitude of 2 kV and 3 kV. We would expect the guiding of the molecules to be most effective at the highest voltage amplitude which could be applied in our decelerator (5 kV) which leads to deeper trap potential. However, the area under the central guiding peak is maximum for a voltage amplitude of 3 kV. A similar trend was observed in our group for guiding of a supersonic beam in a TWSD and was later investigated by Monte-Carlo simulations [256].

The exact reason for this trend is not known. It could be due to the change in transverse

focusing and de-focussing of the beam guided in the decelerator at the detection point at different voltage amplitudes. The deceleration of the molecules was, however, most efficient at the highest voltage amplitude [256]. In the subsequent section, we investigate the effect of the cryogenic source parameters on the guiding of SrF molecules for a chosen guiding velocity of 190 m/s and voltage amplitude of 3 kV applied to the ring electrodes of the decelerator.

### **Optimisation of the source parameters for the deceleration measurements**

We tune the cryogenic source parameter values to obtain a SrF molecular beam from the cryogenic source with a high intensity and a low average longitudinal velocity. The low initial longitudinal velocity of the molecular beam leads to a reduction of the deceleration strengths needed to decelerate the beam. The three main operational parameters which govern the intensity and average longitudinal velocity of the beam from a cryogenic source are the temperature of the cell, the power of the ablation laser beam and the flow rate of the neon. In Fig 5.8, we see an effect of the variation of these three parameters on the time-of-flight profiles for a guiding velocity of 190 m/s and at a maximum voltage amplitude of 3.0 kV of sine-potential applied to the ring electrodes.

In Fig 5.8(a), we investigate the effect of the power of the light from the Nd:YAG ablation laser on the guiding signal of SrF molecular beam by varying the power between (26-240) mJ\*. The cell temperature and the neon flow rate was set to 17 K and 10 sccm, respectively. We observe that the maximum area under the central guided peak is for the ablation powers in the range (43-91) mJ. For ablation powers greater than 91 mJ, the average longitudinal velocity of the molecular beam increases which is not conducive for our deceleration measurements. The time-of-flight profiles taken at relatively higher ablation powers of (158-240) mJ even has a double peak structure with an additional peak at an arrival time of 15 ms of the molecules. Most of the deceleration data is therefore taken for the ablation powers close to 26 mJ which also prolongs the lifetime of our strontium target.

In Fig 5.8(b), we study the effect of the cell temperature on the time-of-flight profiles for guiding of SrF inside the decelerator. The cell temperature is varied in the range of (17-31) K. The power of the ablation laser light and the neon flow rate was set to 67 mJ and 10 sccm, respectively. The total area under the guided signal peak and also the area under the entire signal region of the arrival of the molecular beam is highest at the lowest temperature. The minimum operating temperature is 17 K. Below this temperature, the neon freezes inside the cell and also on the copper and the aluminium shields surrounding the cold cell. A high temperature of the cell should ideally result in a higher flux of the molecular beam and as a result large intensity of the beam out of the cell. This is also observed in the detailed measurements of the source optimisation done in our group, where the density of the molecular beam increases up to cell temperatures of ~30 K [253]. The reason for the large amplitude of the central guiding peak at the lowest cell temperature of 17 K is therefore surprising.

---

\*To investigate the effect of ablation laser powers on the guiding signal, we change the flash lamp voltages in the Nd:YAG laser in equal steps, which in turn result in these corresponding power values.

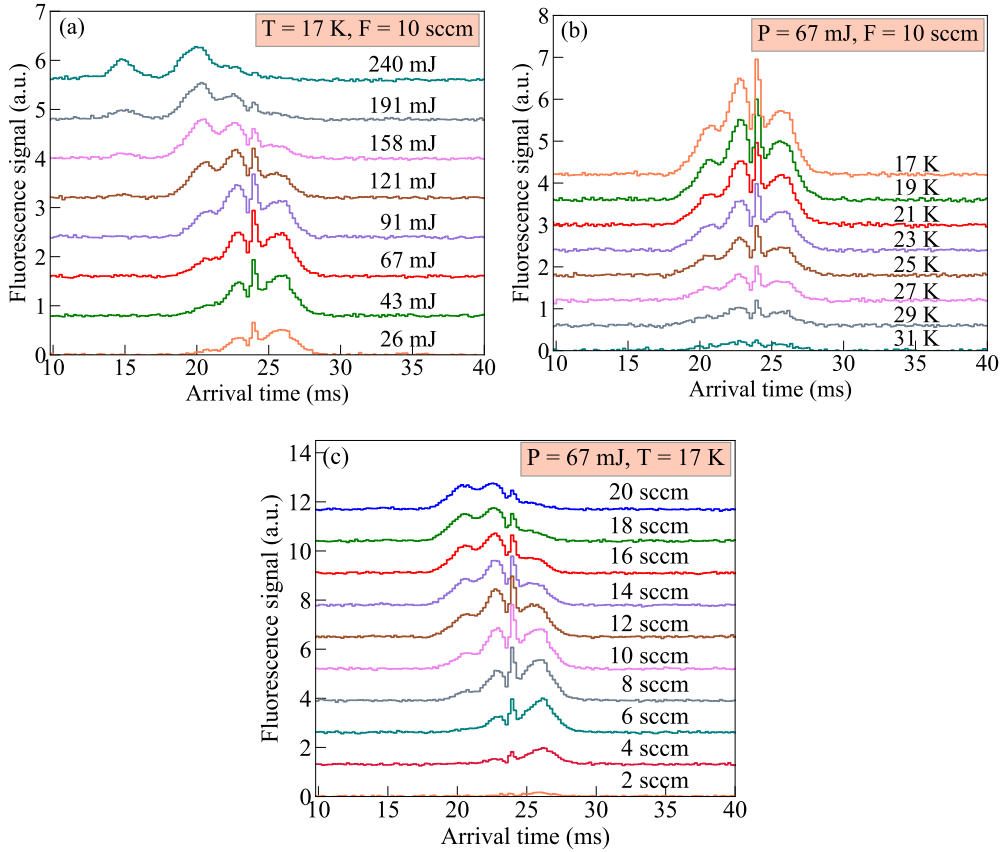


**Figure 5.8** | Time-of-flight profile of SrF molecules (binsize =  $200 \mu\text{s}$ ) guided at a velocity of  $190 \text{ m/s}$  for a voltage amplitude of  $\pm 3 \text{ kV}$  applied to the ring electrodes for (a) different ablation laser powers (accumulated over 3000 shots), (b) different cell temperatures (accumulated over 6000 shots) (c) different neon flow rates (accumulated over 6000 shots). The fixed values of the other two parameters are labelled by  $P$  (ablation power),  $T$  (cell temperature),  $F$  (neon flow). The molecules are detected at a distance of  $12 \text{ cm}$  from the last ring electrode. A vertical offset is added to the individual TOFs for the sake of clarity.

In Fig 5.8(c), we study the effect of the neon flow rate inside the cell on the guiding signal. The power of the ablation laser light and the cell temperature was set to  $67 \text{ mJ}$  and  $17 \text{ K}$  respectively. The area under the signal region and the amplitude of the central guiding peak is highest for neon flow rate between  $(8\text{--}14) \text{ sccm}$ . The molecular beam has an average longitudinal velocity lower than  $190 \text{ m/s}$  at the flow rate values below  $8 \text{ sccm}$ , which is good for the deceleration measurements. However, the intensity of the beam is also lower in comparison to the guiding signal at neon values between  $(8\text{--}14) \text{ sccm}$ . For neon flow larger than  $14 \text{ sccm}$ , the average beam velocity is higher and the intensity is also lower. The optimised source parameters for deceleration measurements are cell temperature at  $17 \text{ K}$ ,

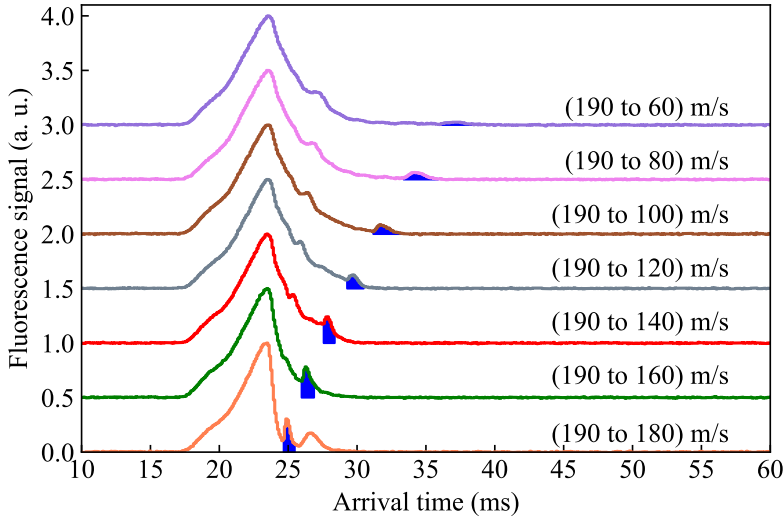


**Figure 5.9** | Experimental time-of-flight profile (absorption  $\sim 2\%$ ) for decelerated beam of SrF molecules (binsize =  $10 \mu\text{s}$ ) at a voltage amplitude of  $\pm 5 \text{ kV}$  from an initial velocity of  $190 \text{ m/s}$  to final velocities of  $(180, 160, 140, 120, 100, 80 \text{ and } 60) \text{ m/s}$  in  $4 \text{ m}$  length of the decelerator. They are detected by collecting the fluorescence emitted by the molecules on exciting them on the transition  $A^2\Pi_{1/2} (\nu = 0, J = 1/2) \leftarrow X^2\Sigma^+ (\nu = 0, N = 1)$ .

the ablation laser power between  $(43\text{-}91) \text{ mJ}$  and the neon flow between  $(8\text{-}14) \text{ sccm}$ . These optimisation parameters hold only for a very definitive objective of obtaining maximum area under the guided peak at a guiding velocity of  $190 \text{ m/s}$ .

### 5.3.3. Deceleration measurements

The molecules are decelerated by chirping down the velocity of the electric traps inside the decelerator. Fig 5.9 shows the time-of-flight profile with a binsize of  $10 \mu\text{s}$  for deceleration of molecules at a voltage amplitude of  $5 \text{ kV}$  from an initial velocity of  $190 \text{ m/s}$  to final velocities of  $(180, 160, 140, 120, 100, 80, 60) \text{ m/s}$ . The time-of-flight profiles have been accumulated over 6000 shots corresponding to 10 minutes. The broad signal distribution in the arrival time range of  $(17\text{-}28) \text{ ms}$  corresponds to the SrF molecules which were confined only transversally (referred to as the non-decelerated part of the signal). The narrow decelerated peak (fill colour blue) corresponds to the photons collected from the molecules confined longitudinally and transversally (referred to as the decelerated part of the signal). The decrease in the amplitude of the decelerated peaks at lower velocities is due to the combined effect of the decrease in the total phase-space acceptance at the entrance of the decelerator at higher deceleration strengths and increased divergence of the beam. The increase in the divergence of the beam also reduces the detection efficiency of the molecules decelerated to lower velocities.

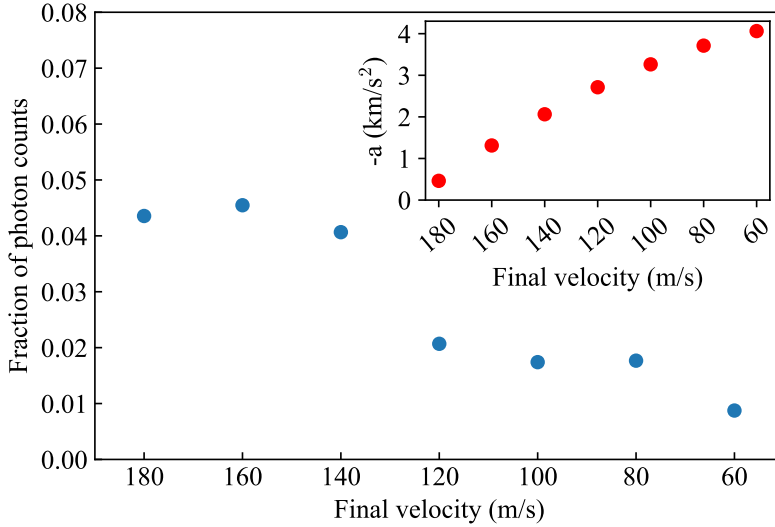


**Figure 5.10** | The fraction of total photon counts per shot detected by the PMT which corresponds to the decelerated SrF molecules are shown by blue dots. The inset shows the deceleration strength applied to the molecules for deceleration to the corresponding final velocities from an initial velocity of 190 m/s.

The fraction of the total photons counts detected per shot which corresponds to the molecules decelerated to different final velocities is shown in Fig 5.10. This fraction is defined as the ratio of the integrated areas under the decelerated peak and the area under the whole TOF profile. The decelerated peak corresponding to the final velocities of (180, 160 and 140) m/s is still within the broad molecular distribution. The fraction of photons counts per shot corresponding to the molecules at these final velocities is calculated by defining the region under the decelerated peak as shaded in blue. In the dearth of clear segregation of the decelerated peak from the non-slowed distribution, the extracted values might be slightly overestimated for these final velocity values. The deceleration strength increases from (0.5 to 4.0) km/s<sup>2</sup> (see inset of Fig 5.10) between deceleration to 180 and 60 m/s and the fraction of photons shots corresponding to the decelerated molecules decreases from 4% to 1%.

## 5.4. Number of molecules

We can estimate the range of the total number of molecules which reach the end of the decelerator from the number of signal photon counts (S) detected by the PMT per shot (see Table 5.1). The total number of molecules ( $N_{mol}$ ) can be calculated by using the same formula that was used in section 3.4.6 (Chapter-3):

$$N_{mol} = \frac{S(\text{decelerated peak}) \times 4\pi}{QE \times T \times \Omega \times n} \times \left( \frac{\pi \times (\Delta y/2)^2}{\Delta y \times w} \right) \times \frac{M \times \Delta y}{a}, \quad (5.5)$$

Average velocity (m/s)	Deceleration strength (km/s <sup>2</sup> )	Photon counts S(total)	Photon counts S(decelerated peak)
180	0.5	870.1(5)	38.28(2)
160	1.3	875.1(6)	39.38(3)
140	2.1	1035.7(6)	42.43(2)
120	2.7	893.3(5)	18.76(1)
100	3.3	993.1(5)	16.88(1)
80	3.7	986.9(5)	17.76(1)
60	4.1	796.4(4)	6.93(1)

**Table 5.1** | Number of photon counts per shot (absorption  $\sim 2\%$ ) detected by the laser-induced fluorescence around the arrival time of the SrF molecules at the detection point for their deceleration to different final velocities. The quoted uncertainties are statistical only. The systematic uncertainties arising from the fluctuations in the number of molecules produced in the source, long term detection laser frequency drifts, are primarily common to all measurements and are estimated to be below 20%.

where  $S(\text{decelerated peak})$  is the signal photons counts per shot in the decelerated peak,  $QE$  is the quantum efficiency of the PMT,  $T$  is the transmission of the optics,  $\Omega$  is the collection solid angle of the fluorescence light,  $n$  is the number of photons scattered per molecule,  $\Delta y$  is the transverse spread of the molecular beam (in mm) after a free flight till the LIF detection point,  $w$  is the spot size of the detection laser beam,  $M$  is the magnification of the collection optics assembly and  $a = 5$  mm is the dimension of the active area of the PMT perpendicular to the beam direction.

Firstly, we state the parameters which are relatively well known. The collection solid angle is 0.94 steradian (see section 5.2.3). The quantum efficiency ( $QE$ ) of the photo-multiplier tube at the detection wavelength of 663 nm is 0.39 and the transmission of the optics ( $T$ ) is 0.75. The spot size ( $w$ ) of the detection laser beam is 3.5 mm. The magnification of the optics assembly shown in Figure 5.3 is  $\sim 1$ . Substituting all these values in equation 5.5, we obtain the following

$$N_{mol} \approx 2 \times \frac{S(\text{decelerated peak})}{n} \times (\Delta y)^2, \quad (5.6)$$

The remaining two parameters in Equation 5.6 are more difficult to determine accurately with the current experimental setup. The number of photons scattered by a single molecule ( $n$ ) on exciting the molecule by a linearly polarised light on the saturated transition  $A^2\Pi_{1/2}$  ( $\nu = 0$ ,  $J = 1/2$ )  $\leftarrow X^2\Sigma^+$  ( $\nu = 0$ ,  $N = 1$ ) (with hyperfine structure of the  $N = 1$  state in the ground electronic state covered) is 9 calculated from the hyperfine branching ratios [216]. In our detection system, the transition on which the molecules are excited for the LIF detection was not saturated and the polarisation of the laser beam might not be completely linear. Hence, for the calculation of the number of molecules, we assume a range of the possible values of  $n$ , between 1-9. The value of  $n$  is limited by the decay of the molecules to the states not addressed by the laser beam and not by the interaction time of the molecules with the detection laser beam. Based on the scattering rate of the molecules on the detection transition, with all the vibrational and rotational levels addressed by the laser beam and

the interaction time with the detection laser beam, the molecules with a velocity between (190 to 60) m/s should be able to scatter  $> 1000$  photons.

The value of transverse spread ( $\Delta y$ ) depends on the final velocity to which the molecules are decelerated at the end of the decelerator. We calculate the resultant position spread of the beam at the LIF detection point by using the free flight distance, the initial transverse position and velocity spread values at the exit of the decelerator from Monte-Carlo simulations (see Table 6.3, Chapter-6). The initial transverse position spread is about  $\sim 1.0(2)$  mm and the initial velocity spread is  $2.2(3)$  m/s at the plane of the last ring electrode. During the deceleration, we switch off the fields inside the decelerator when the synchronous molecules reach the end of the decelerator. The free-flight distance for the molecules with the velocity equal to or larger than the velocity of the synchronous molecules is 18 cm. For molecules with a velocity lower than the synchronous molecules, the free flight distance can be larger due to a finite size of the packet, (6-10) cm as described in section 5.3.2 (also see section 6.2.1, Chapter-6). We, therefore, take an average value of free flight distance to be 23 cm for the entire molecular beam packet. The total transverse position spread of the beam at the detection point for different final velocities is tabulated below (Table 5.2).

v (m/s)	180	160	140	120	100	80	60
$\Delta y$ (mm)	3.0(2)	3.3(2)	3.8(3)	4.3(3)	5.2(3)	6.4(4)	8.5(5).

**Table 5.2** | Transverse position spread (FWHM) calculated for the SrF molecular beam decelerated to different final velocities.

Substituting the range of  $n$  values and  $\Delta y$  in Equation 5.6, an estimated range of the total number of molecules per shot decelerated to different final velocities can be calculated. The number of molecules broadly lie in the range 75-1500 (absorption signal  $\sim 2\%$ ) for all final decelerated velocities assuming the molecules are in near perfect resonance with the detection laser. The uncertainty on the molecule numbers is largely due to the uncertainty in the value of the photons scattered per molecule.

### Estimate of the expected number of molecules

In this section, we estimate the total phase space acceptance of the molecules from the source into the decelerator for a perfect coupling between the source and the decelerator. The longitudinal velocity spread of the molecular packet is about 100 m/s (see section 5.3.2). We assume that the transverse velocity spread is the same as the longitudinal velocity spread, i.e 100 m/s. Molecules with a maximum longitudinal velocity spread of  $\pm 5$  m/s, i.e a total of 10 m/s around the central guiding velocity and a transverse velocity spread of  $\pm 5$  m/s are accepted into the decelerator [257]. The resultant velocity acceptance is therefore given by:

$$\text{Velocity acceptance} = \frac{10}{100} \left( \frac{10}{100} \right)^2 \sim \times 10^{-3}. \quad (5.7)$$

To estimate the transverse position acceptance, we take into account the spot size of the cell exit (4.5 mm) and the diameter of the ring electrode (4 mm). Further, for the calculation of



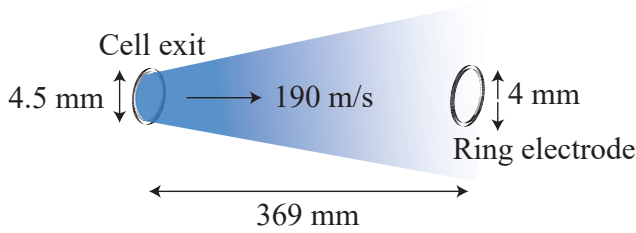


**Figure 5.11** | Free flight of the SrF molecular beam from the cryogenic cell exit till the first ring electrode of the decelerator.

the longitudinal position acceptance, we use the information that the molecules are spread to a maximum distance of 3 mm (for guiding) in the electric field traps of the decelerator separated by a distance of 6 mm (See Reference [257]). The total position acceptance is obtained by multiplying the longitudinal and transverse position acceptance.

$$\text{Position acceptance} = \left( \frac{4}{4.5} \right)^2 \frac{3}{6} \sim 4 \times 10^{-1}. \quad (5.8)$$

The total phase space acceptance of the molecules from the source into the decelerator for the case of perfect coupling is therefore given by multiplying Equations 5.7, 5.8 to be  $4 \times 10^{-4}$  for the guiding mode of the decelerator. The coupling of the source and the decelerator is however not perfect due to a free flight distance of 369 mm between the source and the decelerator (see Figure 5.11). The free-flight time of the beam with an average longitudinal velocity of 190 m/s from the cell exit to the first ring electrode of the decelerator is  $\sim 2$  ms. As a result, only molecules with a transverse velocity of  $\pm 1$  m/s (transverse spread of 2 m/s) can make it into the 4 mm diameter of the ring electrode (see Figure 5.11). So, a factor of 25 is lost in the velocity acceptance. This gives a total acceptance of the molecules into the decelerator for the guiding mode equal to  $2 \times 10^{-5}$ . A similar number for the acceptance has been obtained from the simulations for low deceleration strengths comparable to the guiding mode calculated here (See Table 6.1, Chapter-6).

The number of the molecules in the beam produced from the source is estimated to be around  $\sim 10^9$  molecules per shot (see section 5.3.1). Based on the phase-space acceptance, we expect to be able to guide on the order of 20,000 molecules per shot. The estimated number of molecules from LIF measurements is at least a factor of 15 less than the expected number which might be due to imperfect resonance of the SrF molecules with the detection laser light or due to the saturation parameter ( $I/I_{sat}$ ) value below 1.

Further, in the calculation of the phase-space acceptance, we assumed that the molecules could occupy a distance of 4 mm in the transverse direction, limited by the diameter of the ring electrode. But it was found later (in Chapter-6) that the molecular packets in the electric field traps only occupies a maximum distance of  $\sim 2$  mm (see Table 6.3, Chapter-6) instead of 4 mm as assumed in Equation 5.8 which might reduce the position phase space acceptance by a factor of 4. As a result, the molecules only with a transverse velocity of

+0.5 m/s might be accepted into the decelerator instead of +1 m/s, assumed earlier. This might cause an additional decrease in the velocity acceptance by a factor of 4 as well. The combined phase space acceptance, therefore, might be a factor of 16 lower than what we calculated earlier, which will resolve the discrepancy between the expected and measured numbers. Potential ways to increase the molecule numbers obtained in our measurements are discussed later in section 6.5, Chapter-6.

## 5.5. Conclusion

We have reported on the deceleration of SrF molecular beam from a cryogenic source with an average velocity of 190 m/s down to a velocity of 60 m/s. For this specific case, the molecules were decelerated at a deceleration strength of  $4 \text{ km/s}^2$ . For the case of deceleration strengths larger than  $4 \text{ km/s}^2$ , the signal peak corresponding to the decelerated molecules was not visible anymore. Previously in our group, we have demonstrated the deceleration of SrF molecular beam from a supersonic source from an initial velocity of 290 m/s to a final velocity of 120 m/s at a deceleration strength of  $8.7 \text{ km/s}^2$  [123]. The inability to detect the molecules below a final velocity of 60 m/s can be attributed primarily to the fact that the beam spreads out significantly during the free flight distance of 18 cm from the last ring electrode when it is traveling at 60 m/s, although the number of molecules is very similar at all velocities. In the following chapter, we present the results of the deceleration of the SrF molecules in a 4.5 m long decelerator, where molecules are detected at a distance much closer to the last ring electrode, at about 1 cm. As a result, we can detect the molecules decelerated down to a final velocity of 10 m/s. Refining the rough estimate of the expected number of decelerated molecules presented in this chapter, we also compare our 4.5 m deceleration results in the following chapter with the Monte-Carlo simulations for a more insightful understanding.

# 6

## Trapping of SrF molecules in a 4.5 m long decelerator\*

Measure what can be measured, and make measurable what cannot be measured.-Galileo  
Galilei

Slow beams and trapped samples of heavy diatomic molecules are highly interesting as probes of fundamental physics, specifically for the measurement of the electron's electric dipole moment (as already discussed in Chapter-1) [82, 84, 209, 38, 90], and to study the parity violation [202]. However, it is challenging to obtain trapped samples of suitable molecules, which are key to achieve increased precision in spectroscopy [258].

The technique of Stark (and Zeeman) deceleration is a successful technique to trap beams of molecules [106, 259, 260, 142, 261, 111, 262, 263, 206]. However, until now, CH<sub>3</sub>F (34 amu) [263] and O<sub>2</sub> [206] (32 amu) are the heaviest molecules to have been trapped following Stark and Zeeman deceleration, respectively. In this chapter, we will discuss results for the guiding, deceleration and trapping of a cryogenic beam of SrF in a 4.5 m long decelerator and compare our results to 3-D Monte-Carlo simulations. This is the first time that a relatively heavy molecule like SrF (106 amu) has been decelerated to zero velocity. Our result demonstrates a factor three increase in the molecular mass that has been Stark-decelerated and trapped. We discuss the position and velocity spread of the decelerated beams and estimate the number of molecules that have been decelerated to different final velocities.

### 6.1. Experimental setup recap

The experimental setup (cryogenic source, traveling-wave Stark decelerator (TWSD) and laser-induced fluorescence detection system) used to obtain the results presented in this chapter is identical to the one described in the previous chapter except for an additional

---

\*This chapter is based on P. Aggarwal et al., arXiv:2103.07968 (2021)

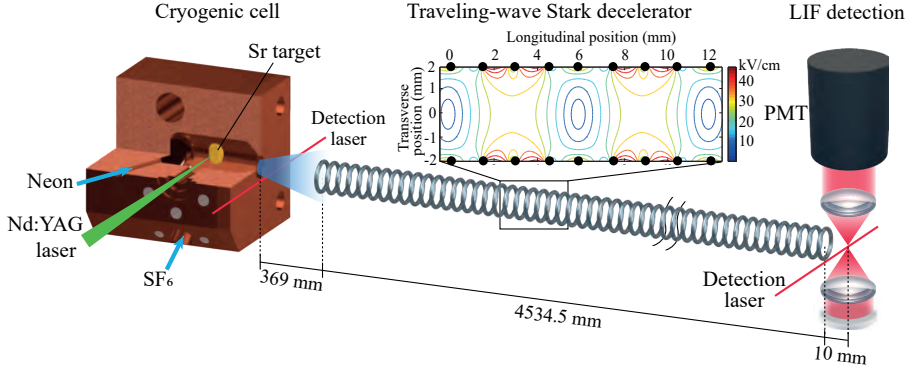


**Figure 6.1** | Experimental setup: The SrF molecules are produced in a cryogenic buffer gas source. A high-energy pulsed Nd:YAG laser ablates strontium from the metal target. The molecules react with SF<sub>6</sub> gas to produce SrF, which is then cooled by collisions with cold neon gas inside the cell. After exiting from the cell, some of the molecules enter the 4534.5 mm long traveling-wave Stark decelerator, positioned at a distance of 36.9 cm from the molecular source exit. The molecules travel through the decelerator in the guiding or the deceleration mode. The molecules leaving the decelerator are then detected at a distance of 1 cm from the last ring electrode of the decelerator.

module added to the Stark decelerator, increasing the length of the decelerator by 504 mm to a total length of 4534.5 mm. The free-flight time of the molecules from the last ring electrode of the Stark decelerator is 1 cm in comparison to the 18 cm free-flight distance for the 4 m deceleration results. The setup is shown in Figure 6.1.

A continuous-wave diode laser beam with a diameter of 0.7 mm and a laser power of 0.5 mW interacts perpendicularly with the molecular beam and excites the molecules on the transition  $A^2\Pi_{1/2} (\nu = 0, J = 1/2) \leftarrow X^2\Sigma^+ (\nu = 0, N = 1)$  at a wavelength of 663 nm. The hyperfine structure of  $N = 1$  rotational state in the electronic state  $X^2\Sigma^+ (\nu = 0)$  is covered by adding sidebands to the detection laser light. The exact details of the laser system can be found in section 3.2 (Chapter-3). The spot size of the detection laser beam is kept small to avoid the scattering of the light due to the proximity of the LIF detection point to the last ring electrode (about 10 mm), and to the last rod electrode (about 5 mm) of the decelerator.

The fluorescence emitted by the molecules is then collected and imaged onto a photomultiplier tube (PMT) by a combination of three 2-inch achromat lenses and a mirror. The achromat lens of focal length 75 mm (back focal length 62 mm) collects the fluorescence in the upward and downward direction (see Figure 6.2). The fluorescence in the downward direction is reflected upward with a mirror. The light in the upward direction is imaged on the PMT using another 2-inch achromat lens of focal length 150 mm (back focal length 167 mm) onto the PMT with an active area of 5 mm × 5 mm. The collection solid angle is 0.94 steradian.

The electrical signal from the PMT is then sent to a single pulse discriminator and a logic

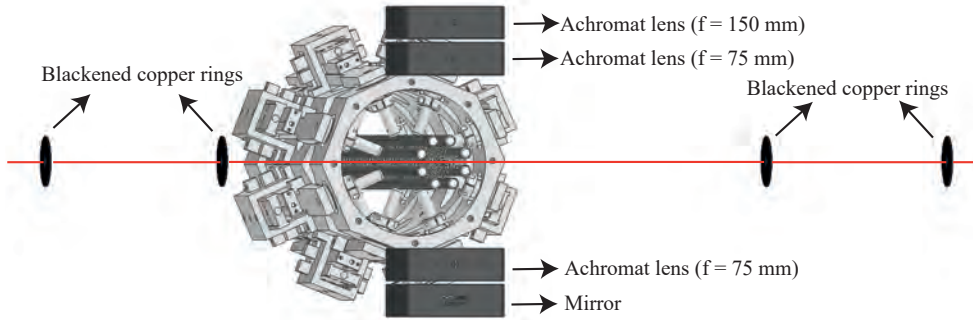


**Figure 6.2** | Fluorescence light collection: SrF molecules traveling through the (black) ring electrodes is detected at a distance of 1 cm from the last decelerator module (grey). The detection laser light (red) excites the SrF molecules on the transition  $A^2\Pi_{1/2} (\nu = 0, J = 1/2) \leftarrow X^2\Sigma^+ (\nu = 0, N = 1)$ . The fluorescence emitted by the molecules is collected in the upward and downward direction by a 2-inch achromat lens (shown in a lens holder). The light in the downward direction is reflected upward by a mirror and is then imaged onto the PMT via a 2-inch achromat lens of focal length 150 mm. Blackened copper rings (inner diameter 7 mm) are mounted along the path of the detection laser beam to reduce background photon counts. The glass windows along the detection laser light for the entrance and exit of the laser beam into the chamber are moved away from the main chamber by adding extension arms (which hold blackened copper rings) to the detection cube.

level converter and then finally to a time-to-digital (TDC) converter. The TDC records the timestamps of the input voltage signal with a time resolution of 320 ps. Triggered with the same timing as the ablation Nd:YAG laser, the molecular time-of-flight (TOF) signal is recorded by making a histogram of the fluorescence photon counts with respect to the arrival time of the molecules.

### Reduction of the background counts

On moving the detection volume closer to the last module of the decelerator, there was an unwanted increase in the background photon counts. The detection laser light directed into the detection volume underwent multiple scatterings inside the chamber contributing to an increase in the background counts. As a result, we used a detection beam with a very small spot size (0.7 mm). We also used blackened copper rings along the path of the detection laser beam into the detection chamber with an inner diameter of 7 mm as shown in Figure 6.2. We added extension arms to the detection cube chamber to move the glass windows, through which the laser beam enters and exit the chamber, further away from the main chamber. We also rolled blackened copper foils on the inside of the extension arms.

The procedure employed for the blackening of copper foils and rings is similar to the one discussed in [264]. A black cupric oxide (CuO) layer was grown on the surface of oxygen-free

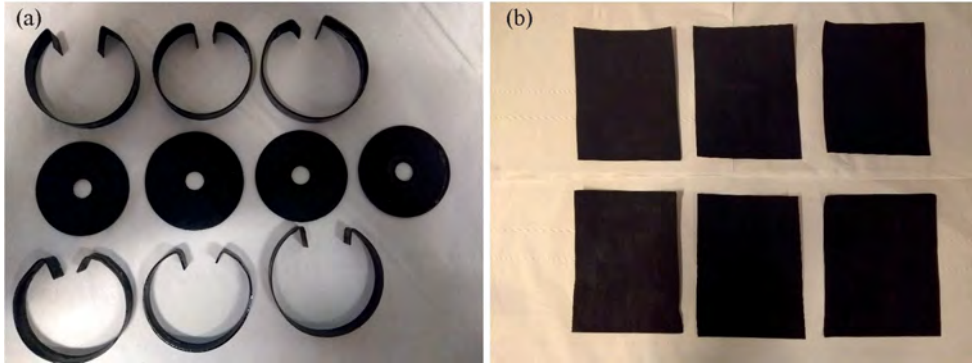
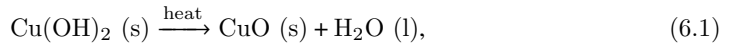


**Figure 6.3** | Copper blackened parts (a) rings and clamps (b) sheets to be rolled along the extension arm of the detection cube.

high conductivity (OFHC) copper parts. The copper parts were first rubbed with sandpaper to get an even surface for the growth of CuO and further cleaned and rinsed properly in an ultrasonic bath containing distilled water. The parts were then immersed in the solution prepared by adding equal parts of NaOH and NaClO<sub>2</sub>, say 100 g each per liter of deionised water. The chemical reaction involved in the blackening of the copper metal is shown below



where s and l corresponds to the solid and liquid state of the substances respectively. The temperature of the mixture was stabilised between 95°C and 100°C before immersing the parts. We also used a magnetic stirrer to minimise the thermal and concentration gradients in the solution and obtain an evenly grown layer of CuO. Parts were left in the solution for about 5 minutes. After the blackening, the parts were rinsed gently with fresh distilled water and allowed to dry in the oven. The blackened copper rings, clamps and the blackened copper sheets are shown in Figure 6.3. Different options for the blackening of vacuum parts were explored in our group. More details on that can be found in [265].

## 6.2. Results

### 6.2.1. Guiding of SrF molecules

In this section, we demonstrate the guiding and deceleration of SrF molecules from a cryogenic source in the TWSD. To guide or decelerate molecules efficiently, it is essential to determine the central velocity of the molecular beam from the source, so that we can set the corresponding guiding velocity or the initial velocity for the deceleration mode of the decelerator. We determined this central velocity by guiding the molecules at different speeds and comparing the strengths of the LIF signals. The optimal guiding velocity which yields the highest guiding signal was figured out to be 190 m/s (also see section 5.3.2, Chapter-5).

Figure 6.4(b) shows the TOF profile of SrF molecules (normalised with respect to the am-

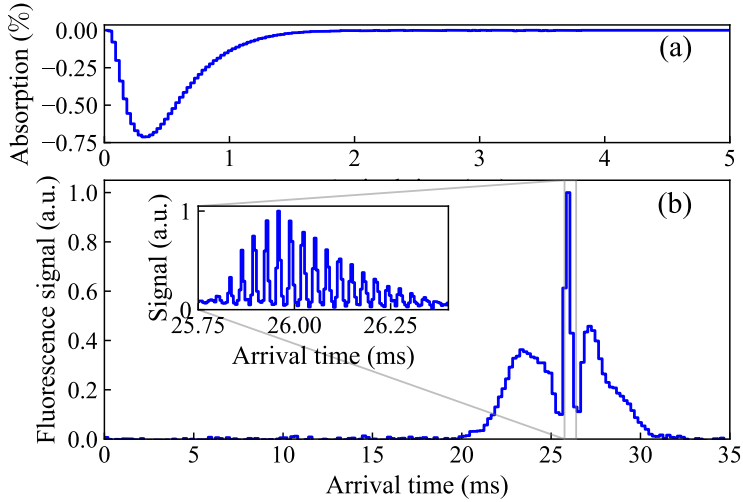


**Figure 6.4** | (a) Typical absorption signal (accumulated over 12000 shots) of the SrF molecular beam measured at a distance of 5 mm from the cell exit and detected by exciting the molecules on the transition  $A^2\Pi_{1/2}$  ( $\nu = 0$ ,  $J = 1/2$ )  $\leftarrow X^2\Sigma^+$  ( $\nu = 0$ ,  $N = 1$ ). (b) The experimental TOF profile measured by exciting the SrF molecules on the same electronic transition as the absorption detection, plotted with a binsize of 200  $\mu\text{s}$ , shows the guiding of the SrF molecular beam at a velocity of 190 m/s at a maximum voltage amplitude of 5.0 kV applied to the ring electrodes of the TWSD. Inset: Zoom-in of the guided peak with a binsize of 5  $\mu\text{s}$ , which shows the individual electric field traps filled by the molecules inside the TWSD.

plitude of the broad distribution) with a binsize of 200  $\mu\text{s}$  guided at a velocity of 190 m/s and at a voltage amplitude of 5.0 kV applied to the ring/rod electrodes of the TWSD. The corresponding absorption signal from the SrF molecules detected at a distance of 5 mm from the cell exit in the cryogenic source is shown in Figure 6.4(a). The LIF signal has been integrated for 12000 molecular shots. As can be seen from the Figure 6.4(b), there is a narrow, high-intensity peak at an arrival time of about 26 ms, which corresponds to the molecules that are confined within both the longitudinal and transverse phase-space acceptance of the decelerator and can thus be guided till the end of the TWSD. The left and right wings on the sides of the guided peak correspond to the molecules that are outside the longitudinal acceptance of the TWSD but within the transverse one, so these molecules can be confined transversely and make it to the end of the TWSD.

The inset of Figure 6.4(b) shows a zoom-in of the guided peak with a binsize of 5  $\mu\text{s}$ , where we can see that there are multiple peaks within the main peak, corresponding to the molecules in multiple electric traps inside the TWSD. There are about 17 distinct peaks corresponding to SrF molecules guided in 17 multiple traps. The total length of the guided molecular packet is 102 mm, for a distance of 6 mm between two adjacent traps inside the decelerator.

### 6.2.2. Deceleration of SrF molecules

#### Experimental results

Figure 6.5 shows the TOF profiles (binsize = 200  $\mu$ s) for the deceleration of SrF molecules, from an initial velocity of 190 m/s of the molecular packet down to different velocities between 170 m/s and 10 m/s in steps of 20 m/s. Every profile in this figure has been integrated for 12000 shots. For all the TOF profiles, we see a broad peak between the arrival time of 20-30 ms and a narrow peak at a later arrival time. The broad peak, similar to the guiding case, corresponds to the molecules that fail to be confined longitudinally in the electric traps but can still go through the TWSD due to the transverse confinement, while the narrow peak, which arrives at a different later time depending on the different final velocities, corresponds to the molecules that are confined both longitudinally and transversely inside the electric traps while being decelerated in the TWSD. The amplitude of the decelerated peaks reduces for lower final velocities, as a result of increased divergence and reduced phase-space acceptance at higher deceleration strengths. The latter is an inherent characteristic of any Stark decelerator.

#### Simulation results

To extract the molecular beam properties and to understand the variation of the longitudinal and transverse acceptance of the decelerator as a function of deceleration strength, we compare the experimental results to numerical trajectory simulations.

Our decelerator consists of 3024 ring electrodes in total. The solution of the electric potential due to a single ring electrode is obtained by solving the Laplace equation numerically in COMSOL Multiphysics using the Dirichlet and Neumann boundary conditions. A linear combination of the solutions of electric potential due to single ring electrodes then gives the solution of the electric potential for any combination of electrode potentials. The solution of the electric potential along with the information of the voltages applied to the electrodes as a function of time gives the electric field distribution. For the case of guiding of the molecules in the decelerator, with a constant velocity  $v$ , the electrode potentials are considered as copies of the same periodic function shifted in phase. The velocity is considered to be a function of time for the decelerating traps. The electric potentials are then differentiated to obtain the spatial and temporal derivatives of the electric field.

The Stark energy  $U(E)$  of the SrF molecule in a specific molecular state (in our case  $N = 1$  rotational state of the electronic and vibrational ground state  $X^2\Sigma^+(v = 0)$ ) is approximated by the 12th order Taylor expansion of the Stark shift obtained by inputting the experimentally measured SrF molecular constants (see Table 2.2, Chapter-2) into the program PGOPHER [215]. The magnitude of the resultant stark force experienced by the molecules inside the decelerator is given by  $F = -\nabla U(E) = -\frac{dU(E)}{dE} \nabla E$ , pointing along the direction of the electric field minimum. By using the resulting Stark force, the equations of motion of a molecule with mass  $m$  moving adiabatically in a Stark potential can be solved numerically, combined with a proper boundary condition.

We use a fifth-order Runge-Kutta-Dormand-Prince algorithm, which evaluates the Stark force once in time step of 1  $\mu$ s. Numerical integration routines from the Odient C++ library were used. A more detailed description of the simulation package can be found in [266]. The



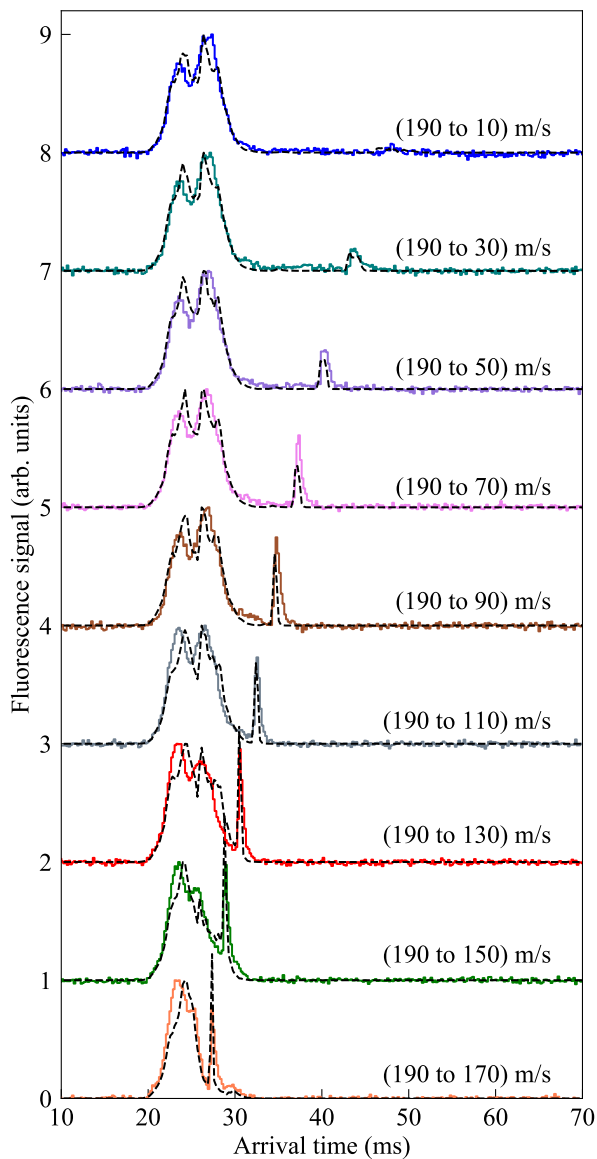


**Figure 6.5** | Experimental (solid coloured lines) and simulated (dashed black lines) TOF profiles (binsize = 200  $\mu$ s) of SrF molecules, decelerated from 190 m/s to different final velocities at a maximum voltage amplitude of 5 kV applied to the ring electrodes of TWSD. The molecules are detected by exciting them on the transition  $A^2\Pi_{1/2}$  ( $v = 0, J = 1/2$ )  $\leftarrow X^2\Sigma^+$  ( $v = 0, N = 1$ ) and imaging the fluorescence emitted on the PMT. A vertical offset has been added to different plots for clarity.

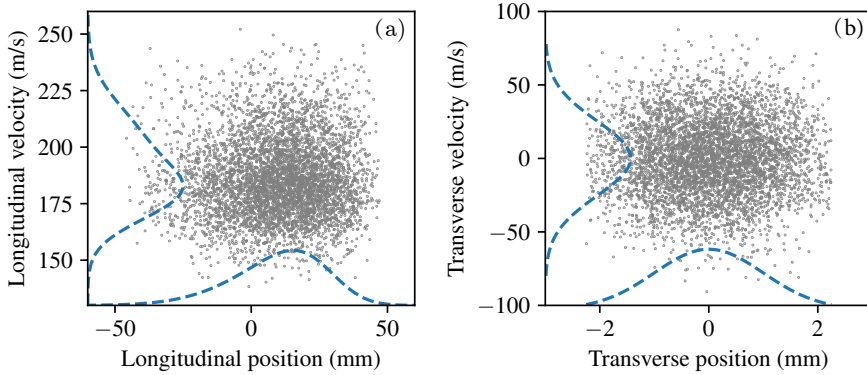


**Figure 6.6** | Initial phase-space distribution of SrF molecules in the simulations, (a) longitudinal position vs. longitudinal velocity, (b) transverse position vs. transverse velocity. Dashed lines represent projections of the corresponding parameters. The longitudinal velocity components distributions are modelled by a sum of two-Gaussian distributions to emulate the skewed profile of the absorption signal measured at a distance of 5 mm from the cell exit (see Figure 6.4). The central velocity and velocity spread (FWHM) of the two-Gaussians functions are (202 m/s and 34 m/s) and (179 m/s and 19 m/s), respectively. The transverse velocity distribution is modelled by a single Gaussian function with a velocity spread (FWHM) of 60 m/s. The transverse position distribution is a truncated standard normal distribution with the truncated range of  $[-2.25 \text{ mm}, 2.25 \text{ mm}]$ , as our cell aperture has a diameter of 4.5 mm. The longitudinal position distribution is generated by choosing values from the range  $[-47.5 \text{ mm}, 47.5 \text{ mm}]$  according to the relative weights to reproduce the typical absorption signal profile.

time-of-flight profile for the deceleration of SrF molecules shown by the dashed black line in Figure 6.5 is obtained by random sampling the initial 3D phase-space distribution of the molecules. We have used a Cartesian coordinate system throughout the simulations, where the z-axis is the direction of propagation of the molecular beam, the x-axis points straight up and the y-axis points to the right on looking along the z-axis. The properties of the initial source distribution in the simulation, such as the initial longitudinal velocity and the velocity spread of the molecules in the longitudinal direction are optimized so that the TOF profile matches the experimental signal.

Figure 6.6 shows the initial source distribution at the exit of the cold cell in the cryogenic source corresponding to the simulation results shown in Figure 6.5. We have assumed the detection volume for obtaining the time-of-flight profile in simulations, corresponding to a detection laser beam of diameter 0.7 mm exciting the molecules from the  $N = 1$  rotational state of  $X^2\Sigma^+(v = 0)$  electronic state. To match the longitudinal arrival time distribution of a SrF molecular beam visible in the absorption signal (see Figure 6.4(a)), the longitudinal velocity components distributions are modelled by the sum of two Gaussian functions and the transverse velocity components in the x and y directions are both modelled by a single Gaussian distribution (see Figure 6.6).

Average velocity $v$ (m/s)	Decelerated molecules/Total molecules ( $\times 10^{-6}$ )
170	20 (4)
150	23 (6)
130	17 (5)
110	13 (3)
90	12 (2)
70	10 (1)
50	10 (1)
30	9 (2)
10	7 (1)

**Table 6.1** | Fraction of the molecules from the cryogenic source that enter and reach the end of the decelerator calculated from the simulations for a total of 1.3 million molecules, for different deceleration strengths. These numbers take into account a free-flight distance of  $\sim 37$  cm between the source and the decelerator.

The fraction of molecules from the source that enters the decelerator and reach the last ring electrode of the decelerator for different final velocities can be obtained from the simulations and is tabulated in Table 6.1. The fraction of molecules accepted into the decelerator entrance at a deceleration strength of  $4 \text{ km/s}^2$  for deceleration to  $10 \text{ m/s}$  is a factor of three lower than the molecules accepted for deceleration to  $170 \text{ m/s}$  at a deceleration strength of  $0.8 \text{ km/s}^2$ . In the current setup, the transverse phase-space acceptance of the decelerator is underfilled due to the large free-flight time ( $\sim 37 \text{ cm}$ ) between the source and the decelerator (see section 5.4, Chapter-5).

The fraction of photon counts detected in the detection volume corresponding to the SrF molecules decelerated to different velocities, which we define as the ratio of the integrated areas of the decelerated peak in the TOF profile and the area under the whole TOF profile, is shown in Fig. 6.7, where we also include the simulation results. We can see that for the case of experimental measurements for deceleration to  $170 \text{ m/s}$  and  $10 \text{ m/s}$ , the fraction of photon counts detected corresponding to the decelerated molecules follows a downward trend from  $13.1(2)\%$  to  $1.4(1)\%$ . This decrease is due to a combined effect of a decrease in the phase space acceptance and a decrease in detection efficiency due to the divergence at low velocities. For the case of simulations, the fraction of photon counts reduces from  $11.2(2)\%$  for deceleration to  $170 \text{ m/s}$  to  $2.1(1)\%$  for deceleration to  $10 \text{ m/s}$ .

### 6.2.3. Analysis of the peak substructure for the calculation of longitudinal position and velocity spread

A zoom-in of the TOF showing decelerated molecules at different final velocities is shown in Fig. 6.8(a) with a binsize of  $5 \mu\text{s}$ . Multiple peaks correspond to molecules that are confined in several consecutive electric traps inside the TWSD.

We can compare the peak structure corresponding to different final velocities from two different perspectives. Firstly, the peaks are generally broader for slower molecules than for

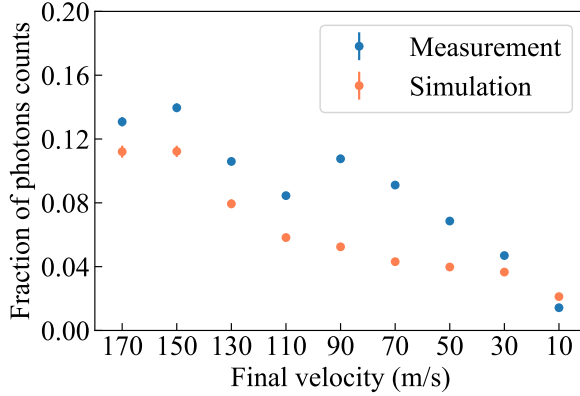


**Figure 6.7** | Fraction of the total photon counts per shot detected corresponding to the decelerated molecules at different final velocities between 170 m/s and 10 m/s from a starting velocity of 190 m/s, at a maximum voltage amplitude of 5 kV applied to the ring electrodes in TWSD, obtained from measurements and simulations.

the faster ones, which is because when the molecule packets exit the TWSD, the slower ones have a longer free-flight time before arriving at the LIF detection point and the packet of molecules thus expands more. As a result, for slower molecules, we also detect fewer molecular packets due to a finite transverse spread of the beam. There are about 17 molecular packets detected for final velocities between (170-90) m/s, whereas only 6 packets are detected at a final velocity of 30 m/s. No peak substructure is visible in the deceleration peak corresponding to the final velocity of 10 m/s. Secondly, within the peak substructure for a certain final velocity, the consecutive peaks have different time spread: the ones which arrive later are broader than the ones coming earlier. This is because when all molecule packets are released simultaneously from the multiple neighbouring electric wells, the molecules in the electric traps behind the trap of the synchronous molecules have longer free-flight time till the detection laser light interaction point and thus expand in space more before being detected. The peak labelled (\*) in Figure 6.8(a) represents the synchronous molecules. When these synchronous molecules reach the last ring electrode, the voltages on the ring electrodes are switched off. The time to ramp down the voltages on the ring electrodes is 260  $\mu$ s.

From the difference in the widths of the peak in the substructure corresponding to a certain velocity in Fig. 6.8 (a), we can derive the longitudinal position spread and the longitudinal velocity spread. The width of the first few peaks is primarily due to the position spread of the molecules in the traps, especially for the higher final velocities. The increment in the widths of the adjacent peaks can be attributed to the velocity spread of the molecular packet.

We can obtain the widths of all the sub-peaks in the decelerated signal at different final velocities by fitting a Gaussian function to all the sub-peaks. The Gaussian fits are shown in the dashed black line in Figure 6.8(a). The full-width-at-half-maximum (FWHM) in units of distance of all the adjacent peaks for deceleration to (170, 150, 130, 110, 90, 70, 50 and

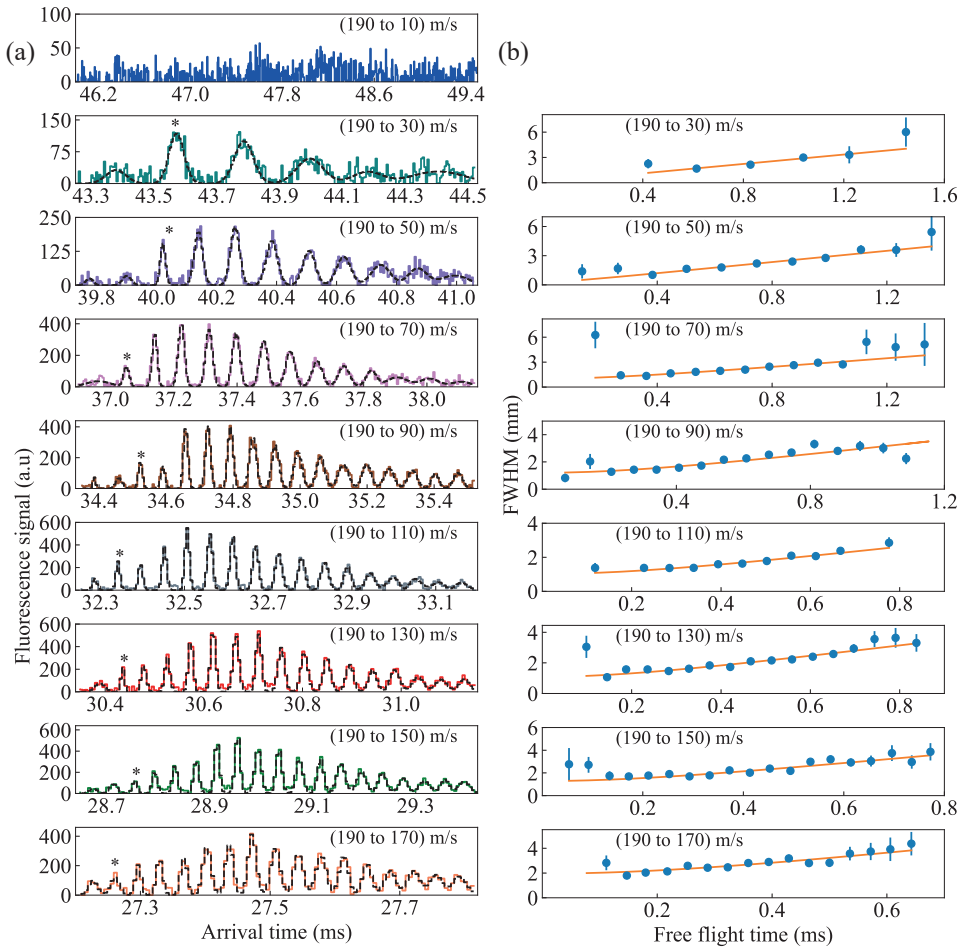


**Figure 6.8** | (a) Zoom-in of the TOF signals (binsize =  $5 \mu\text{s}$ ) around the arrival time of the decelerated SrF beams from an initial velocity of 190 m/s to final velocities between (170-10) m/s. The peak labelled (\*) corresponds to the synchronous molecules. When the synchronous molecular packet reaches the end of the decelerator, the electric fields inside the decelerator are switched off. The dashed black lines are the multiple Gaussian fittings to extract the width of these peaks. Peak substructure is not visible for beams decelerated to 10 m/s. (b) A quadratic function,  $\sqrt{(\Delta z)^2 + (\Delta v \cdot t)^2}$  is fit (orange line) to the increment in the widths of the individual peaks (blue scatter points), where  $\Delta z$  and  $\Delta v$  is the longitudinal position and velocity spread of the molecular beam and  $t$  is the free flight time till the LIF point after the release from the electric traps ( $t=0$ ) for all deceleration cases. The Gaussian fitting to some of the individual peaks with small amplitude results in negative width values. The negative width values are not plotted in panel (b) but are taken into account during the quadratic fit and for error estimation.

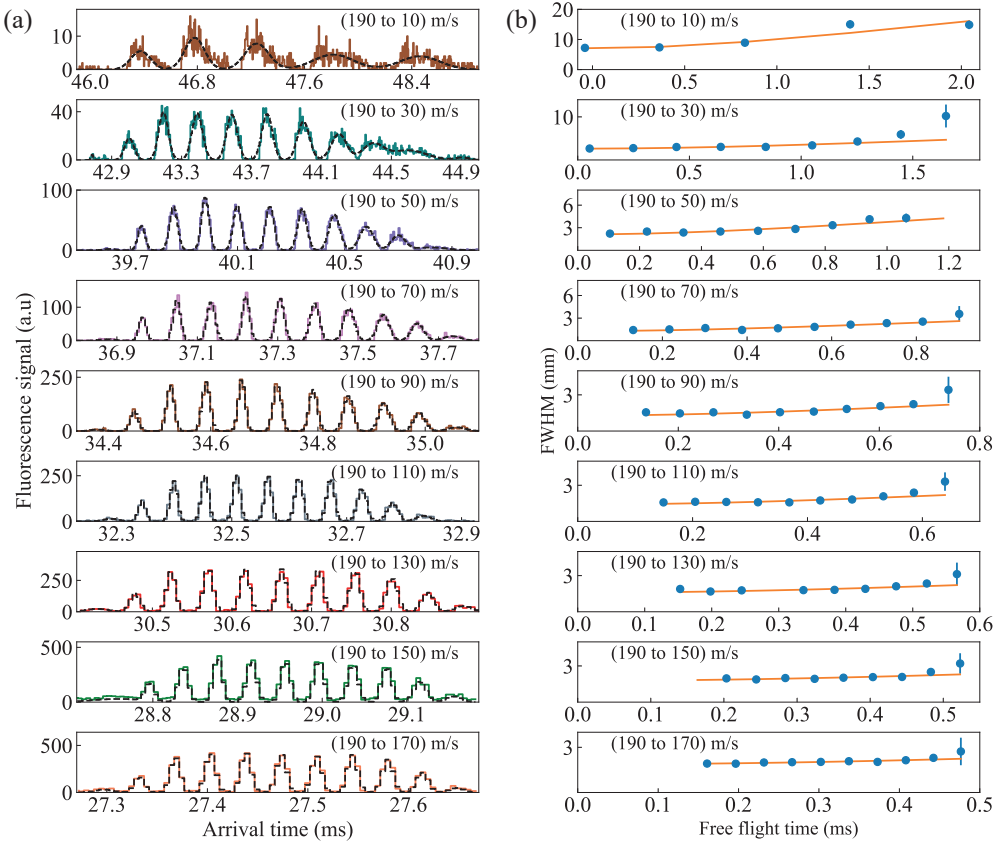


**Figure 6.9** | (a) Zoom-in of the simulated TOF signals (binsize =  $5 \mu\text{s}$ ) around the arrival time of the decelerated SrF beams from an initial velocity of 190 m/s to final velocities between (170-10) m/s. The dashed black lines are the multiple Gaussian fittings to extract the width of these peaks. (b) A quadratic function is fit (in coral) (similar to Figure 6.8) to the widths (blue scatter points) of the adjacent peaks for all final velocities. The Gaussian fitting to some of the individual peaks with very small amplitude in the time-of-flight profiles result in negative width values similar to the case of experimental data. The negative width values are not plotted but are taken into account for the quadratic fit and error estimation.

30) m/s are shown in Figure 6.8(b) (blue dots). We can extract the longitudinal position and velocity spread of the molecular beam at different final velocities by fitting a quadratic function  $\sqrt{(\Delta z)^2 + (\Delta v \cdot t)^2}$  to the trend of the increment in the widths of the adjacent peaks [267] for a certain final velocity [orange line in Figure 6.8(b)]. Here,  $\Delta z$  and  $\Delta v$  corresponds to the longitudinal position and velocity spread, respectively of the molecular beam at a specific final decelerated velocity and  $t$  is the free-flight time of the molecular packet till the LIF point after the release from electric traps. The width of the first peaks in the substructure for almost all the final velocities to which molecules are decelerated do not lie

Deceleration case	Deceleration strength (km/s <sup>2</sup> )	Position spread $\Delta z$ (mm)		Velocity spread $\Delta v$ (m/s)	
		Exp.	Sim.	Exp.	Sim.
190 $\rightarrow$ 170	0.8	2.1(3)	1.9(1)	10(2)	9(1)
190 $\rightarrow$ 150	1.5	1.8(3)	1.8(1)	9(3)	9(1)
190 $\rightarrow$ 130	2.1	1.3(2)	1.6(1)	6(2)	7(1)
190 $\rightarrow$ 110	2.6	1.2(2)	1.4(1)	4(1)	6(1)
190 $\rightarrow$ 90	3.1	1.4(3)	1.3(1)	3(1)	4(1)
190 $\rightarrow$ 70	3.4	1.2(3)	1.3(1)	3(1)	4(1)
190 $\rightarrow$ 50	3.7	1.0(2)	2.1(2)	3(1)	3(1)
190 $\rightarrow$ 30	3.9	-	2.6(2)	3(1)	2(1)
190 $\rightarrow$ 10	4.0	-	2.4(3)	-	1(1)

**Table 6.2** | (a) Longitudinal velocity spread and (b) longitudinal position spread of the SrF molecular beams decelerated from an initial velocity of 190 m/s to final velocities of (170, 150, 130, 110, 90, 70, 50, 30, 10) m/s, calculated from the experimental (Exp.) and simulated (Sim.) datasets.

on the quadratic fit. This is likely because the first peaks have a very small corresponding peak amplitude and the peak width cannot be deduced convincingly by the Gaussian fit.

The longitudinal velocity and position spread of the decelerated molecules which were extracted from the quadratic fits are shown in Table 6.2. The position spread cannot be deduced for a beam at a final velocity of 30 m/s due to the limited number of peaks that are detected in that specific case. At low deceleration strengths (1 km/s<sup>2</sup>), the molecules with a longitudinal velocity spread (FWHM) of 10 m/s around the central deceleration velocity are accepted into the decelerator. At higher deceleration strengths, molecules with a longitudinal velocity spread of 3 m/s are accepted into the decelerator. This might be an effect of the divergence of the molecular packets away from the detection volume at higher deceleration strengths. The spatial spread of the SrF beam at a velocity of 170 m/s is 2 mm, which reduces to 1 mm at lower longitudinal velocities.

With the same method, we determine the longitudinal velocity spread and position spread of the molecular beam at different final velocities from the simulated data by fitting a quadratic function to the increment in the widths of the adjacent peaks in the substructure [see Figure 6.9(b)]. The Gaussian fit used to obtain the width of the adjacent peak is shown by the dashed line in Figure 6.9(a). The extracted values are shown in Table 6.2. The initial molecular packet in the simulations seems to be a bit shorter with a spatial extent of about 11 sub-packets, in comparison to 17-19 individual packets detected for the experimental data. However, the value of the longitudinal velocity spread of the beam in the simulations was chosen to match the broad non-slowed distribution in the simulated time of flight profile with the corresponding experimental signal in Figure 6.5.

The values of the longitudinal velocity acceptance match well for the experimental and simulated data within the error bars. The longitudinal position acceptance values also matches for the most part, except for a sudden increase in the position spread of the beam

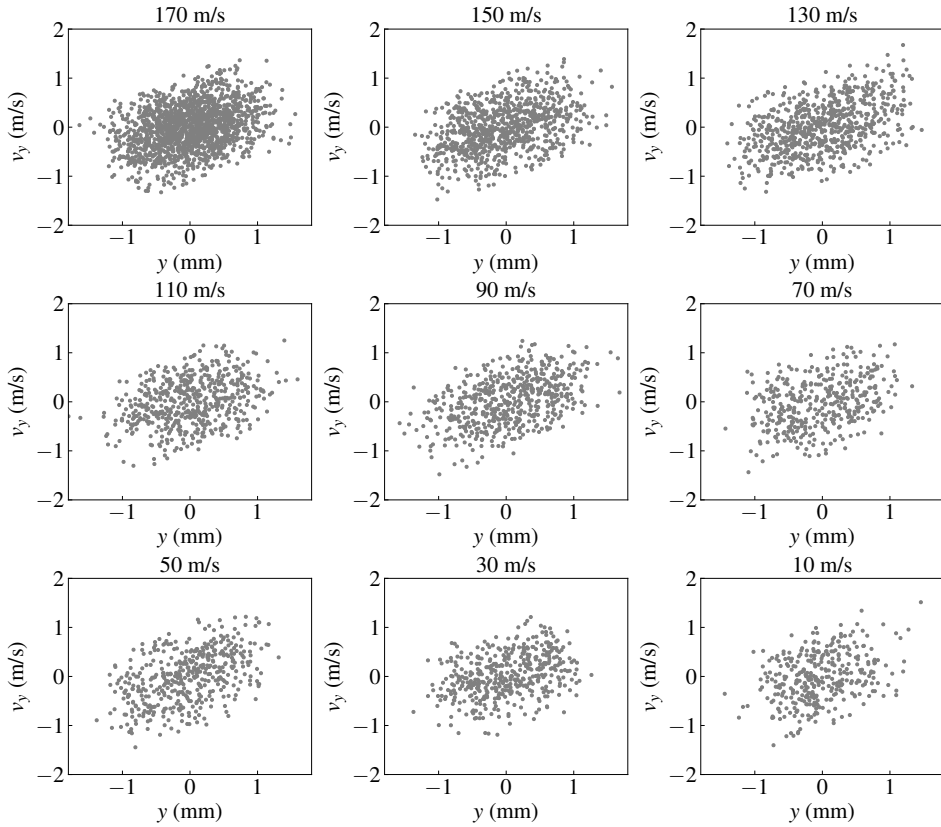


**Figure 6.10** | Transverse phase-space distribution of SrF molecules deduced from the simulations at the instant when the synchronous packet enters the first ring electrode of the decelerator, for deceleration from an initial velocity of 190 m/s to different final velocities between 170 m/s and 10 m/s.

at lower velocities observed in the simulated data. For the experimental data, there is a decrease in the longitudinal spread by a factor of 2, between deceleration to 170 m/s and deceleration to 50 m/s. We do not expect an increase in the position spread at lower velocities which is calculated from the simulated data yet. It seems that the quadratic fit does not work very well for these specific cases.

#### 6.2.4. Transverse position and velocity spread

We deduce the values of the transverse position and velocity spread of the beam at different final velocities from the simulations. The trajectories of the individual data points which correspond to the molecules, are saved for the entire path along the length of the decelerator. Only the trajectories of those molecules are saved which are present within the 4 mm diameter of the ring electrode till the time the voltage on the ring/rod electrodes is non-



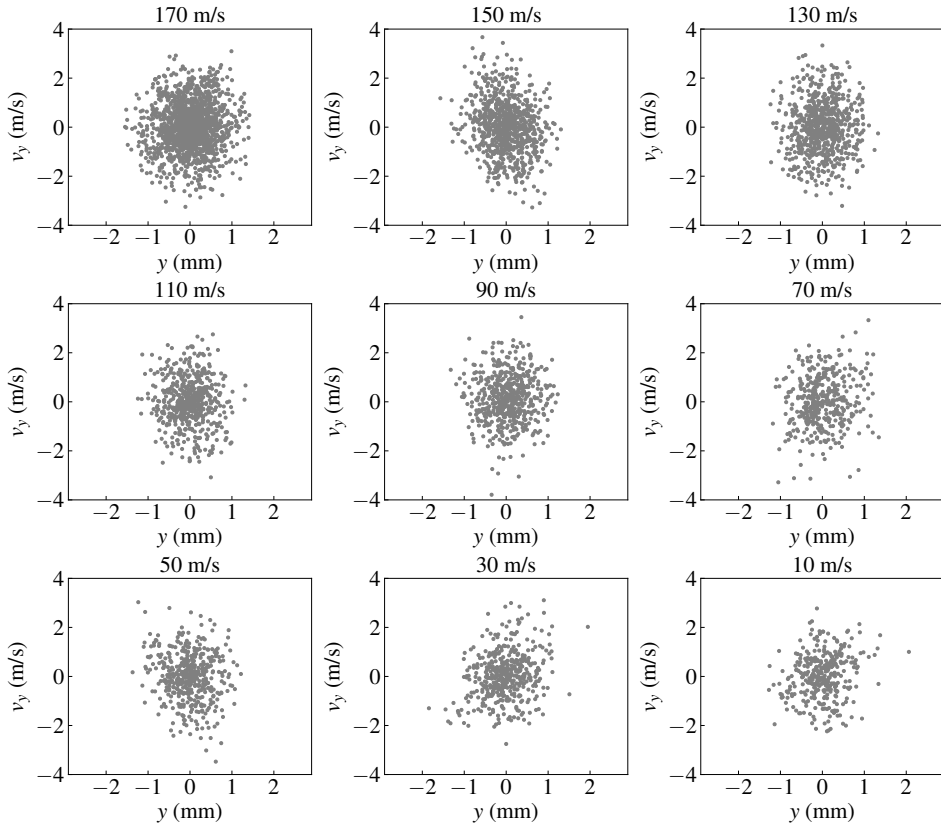


**Figure 6.11** | Transverse phase-space distribution of the SrF molecules deduced from the simulations at the instant when the synchronous packet reaches the last ring electrode of the decelerator and voltages on the electrodes are switched off, for deceleration from an initial velocity of 190 m/s to different final velocities between 170 m/s and 10 m/s.

zero. After the voltages on the electrodes are switched off, the molecules could be present beyond the 4 mm diameter of the ring electrode. A total of  $10^4$  trajectories are saved for all molecules which reach the end of the decelerator, but not all of them correspond to the decelerated molecules. The initial 3D phase-space distribution of the molecules at the exit of the cell is similar to the one shown in Figure 6.6. The voltage waveform applied to the ring electrodes is the same as was explained in the preceding sections 6.2.2-6.2.3 of this chapter. The electric fields inside the decelerator are switched off when the synchronous molecules reach the end of the decelerator.

Figures 6.10, 6.11 shows the transverse phase-space distribution of the decelerated molecules in the plane of the first and last ring electrode of the TWSD for the case of deceleration to different final velocities. The values of the transverse velocity and position spread at the entrance and exit of the decelerator is tabulated in Table 6.3. Only 10% of the total

$v$ (m/s)	$\Delta v_i$ (m/s)	$\Delta y_i$ (mm)	$\Delta v_f$ (m/s)	$\Delta y_f$ (mm)
170	1.10(1)	1.34(2)	2.04(5)	1.05(1)
150	1.17(2)	1.52(3)	2.20(5)	1.02(1)
130	1.25(2)	1.59(3)	2.28(4)	1.02(2)
110	1.23(3)	1.40(2)	2.09(6)	0.97(1)
90	1.23(1)	1.54(3)	2.14(4)	1.05(1)
70	1.21(2)	1.54(5)	2.41(6)	1.08(3)
50	1.32(3)	1.44(3)	2.16(4)	1.01(2)
30	1.06(2)	1.43(3)	1.92(6)	1.04(1)
10	1.19(2)	1.13(4)	2.04(5)	0.89(2).

**Table 6.3** | Transverse position spread and velocity spread (FWHM) of the SrF molecular beam at the plane of the first ( $\Delta y_i$ ,  $\Delta v_i$ ) and last ring electrode ( $\Delta y_f$ ,  $\Delta v_f$ ) of the TWSD for deceleration to different final velocities between 170 m/s and 10 m/s.

saved trajectories correspond to the decelerated molecules at a final velocity of 170 m/s. The number of molecule trajectories for a final velocity of 10 m/s is lower in comparison to 170 m/s due to the reduced phase space acceptance (See Table 6.1).

The transverse phase-space distribution at the plane of the first ring electrode is titled for all final velocities due to the large free-flight distance for the molecules between the source and the decelerator. Based on the values in Table 6.3, we can see that the initial transverse velocity of the molecules is restricted to  $\pm 0.5$  m/s, even though the transverse velocity acceptance of the decelerator is  $\pm 5$  m/s [257]. This is also a consequence of the large source-decelerator distance. The phase-space acceptance of the decelerator is therefore under-filled and as a result, the initial transverse velocity spread and position spread of the molecules that make it to the end is also similar for very different deceleration strengths. The transverse velocity spread at the exit of the decelerator is larger than the velocity spread at the entrance of the decelerator due to exchange of energy with longitudinal velocity components.

### 6.3. Stopping and trapping of molecules

We have decelerated SrF molecules down to 10 m/s by the combination of cryogenic molecular beams and TWSD. It is natural now to proceed one step further to bring molecules to a standstill or even trap the molecules in the lab frame for a certain time. This would be a beneficial demonstration for a variety of experiments requiring trapped molecules. Although it is possible to first decelerate molecules to a velocity that can be captured by a trap of some type (e.g. an electric trap or a MOT) with the full decelerator length of 4.5 m and then load them to the trap, a more convenient but also useful approach we employ here is to stop and trap molecules inside the decelerator. Specifically in our measurements, SrF molecules are first decelerated from 190 m/s to 0 m/s within a length of 4.2 m, and then held for a trapping time  $\Delta t$  in the inherent electric traps of the decelerator, and then accelerated out of the decelerator with the same magnitude of acceleration strength as the deceleration strength, meaning that molecules are accelerated to 52 m/s in the remaining 0.3 m length of the decelerator and detected 1 cm away from the last ring of the decelerator.

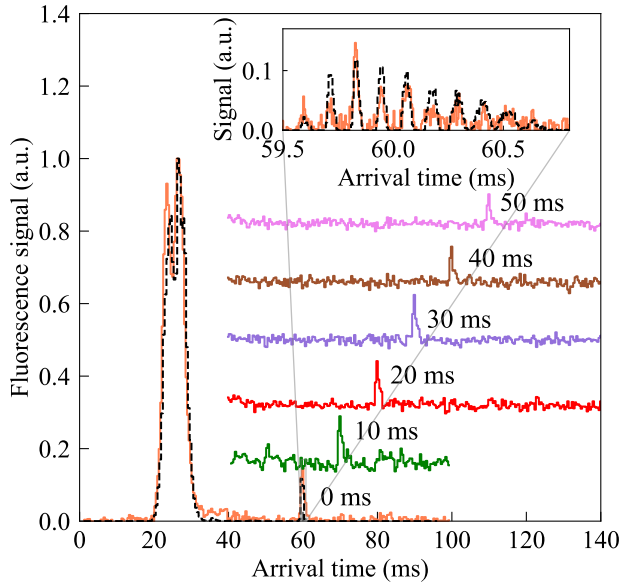


**Figure 6.12** | The time-of-flight profile of SrF molecules (amplitude normalised, binsize =  $400 \mu\text{s}$ ) demonstrating the trapping of SrF molecules for different times, ( $\Delta t$ ). Molecules are decelerated from  $190 \text{ m/s}$  to  $0 \text{ m/s}$  in  $4.2 \text{ m}$ , and then held in the electric traps of the TWSD for  $\Delta t = (0, 10, 20, 30, 40 \text{ and } 50) \text{ ms}$  and then accelerated to  $52 \text{ m/s}$  in the remaining  $0.3 \text{ m}$  of the TWSD. The undecelerated molecules are only shown for the case of  $\Delta t = 0$ . A vertical offset has been added to the plots for clarity. The inset shows a zoom-in of the trapping peak (binsize =  $5 \mu\text{s}$ ) for the  $\Delta t = 0 \text{ ms}$  case for both experimental and simulated TOF. Molecules are detected by exciting them on the transition  $A^2\Pi_{1/2} (\nu = 0, J = 1/2) \leftarrow X^2\Sigma^+ (\nu = 0, N = 1)$  and imaging the emitted fluorescence on the PMT.

### 6.3.1. Experimental and simulation results

The resultant TOF signals of SrF molecules (normalised with respect to the amplitude of the non-decelerated peak) for different trapping times,  $\Delta t = (0, 10, 20, 30, 40 \text{ and } 50) \text{ ms}$  are shown in Fig. 6.12. Each plot is integrated over a total of 72000 shots. In each time-of-flight profile, the first peak arriving at around 20-30 ms represents the molecules that are confined transversely but not longitudinally, and then there is a relatively smaller amplitude peak arriving at a later time which corresponds to the molecules that have been trapped in the lab frame for  $\Delta t$ . Moreover, a zoom-in of the small amplitude peak for the  $\Delta t = 0 \text{ ms}$  case in the inset of Fig. 6.13 shows the molecules have been confined inside about ten consecutive electric traps of the decelerator. The dashed black line represents the TOF profile of the SrF molecules obtained from simulations for the same voltage waveform file as was applied during the experimental run and initiated by the same initial 3D phase-space distribution of the molecular beam as was used for the deceleration case (see Figure 6.6).

A fraction 2.8(1)%, 1.9(1)%, 2.1(1)%, 2.1(1)%, 1.5(1)%, 1.2(1)% of the total photons counts

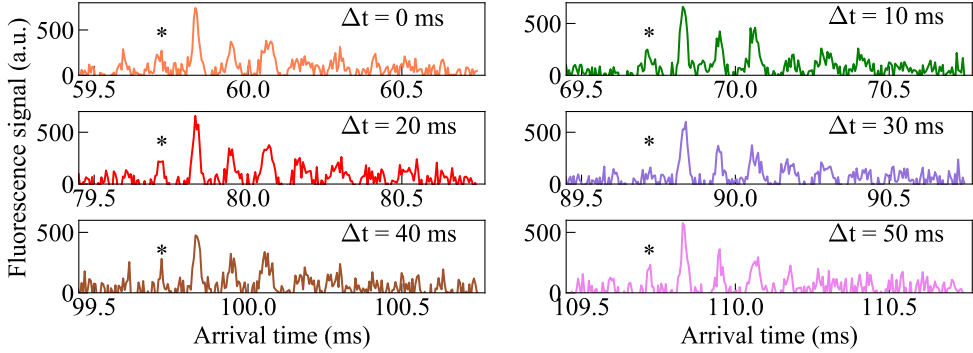


**Figure 6.13** | A zoom-in (binsize =  $5 \mu\text{s}$ ) of the TOF profiles shown in Figure 6.12 (accumulated over 72000 shots) around the arrival time of the trapped SrF molecular beams for a trapping times of  $\Delta t = (0, 10, 20, 30, 40, 50)$  ms. The peak labelled (\*) corresponds to the synchronous molecules.

detected by the PMT corresponds to the molecules trapped for (0, 10, 20, 30, 40 and 50) ms, respectively. The peak corresponding to the decelerated and trapped SrF beam in the simulated TOF accounts for a fraction of 2.2(1)% of the total photon counts. The amplitude of the decelerated/trapped peak in the simulated TOFs corresponding to the arrival of the molecular beam at the detection spot is the same for all different trapping times. This is because the simulations do not take into account the losses due to collisions with the background case for longer trapping times. Figure 6.13 shows the zoom-in of the peak corresponding to the decelerated and trapped SrF molecules for different trapping times as shown in Figure 6.12 for  $\Delta t = 0$ . The number of peaks in the substructure detected for a certain trapping time reduces from about 10 peaks for 0 ms trapping time to 5 peaks for 50 ms trapping time.

### 6.3.2. Lifetime of the molecules in the electric trap

We integrate the number of signal photons counts around the arrival time of the trapped molecules from the TOF profile integrated over a total of 72000 shots as shown in Figure 6.13. The integrated signal is described by  $S(t) \propto e^{-t/\tau_{BG}}$ , where  $t_{BG}$  is the decay time due to the background gas collisions. In Fig 6.14, we plot the integrated signal on a logarithmic scale versus the trap time,  $t$ . A fitted decay constant of  $\tau_{BG} = 73(15)$  ms, primarily limited due to the collisions with the background gas, is reasonable at the background pressure of  $7 \times 10^{-7}$  mbar.

### 6.3.3. Longitudinal velocity and position spread of the trapped molecular beam

The longitudinal position and velocity spread of the molecular beam trapped inside the electric traps of the decelerator for different trap times will be the same as they all have the same applied deceleration and acceleration strength. A zoom-in of the individual peak

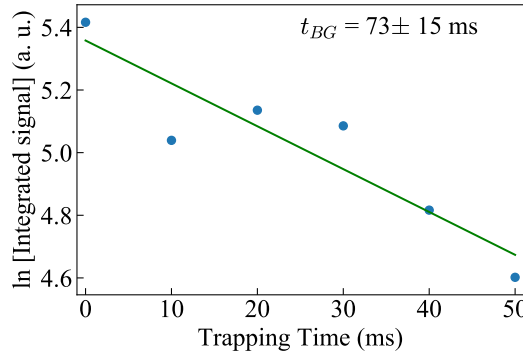


**Figure 6.14** | Log of the integrated fluorescence signal detected in the  $N = 1$  rotational state of the electronic ground state  $X^2\Sigma^+(v = 0, N = 1)$  of SrF, proportional to the fraction of the photon counts per shot detected at various trapping times (0-50) ms, as a function of trap time (ms). Here, we fit a straight line to the data assuming that the decay in the number of molecules due to the background collisions is exponential,  $S(t) \propto e^{-t/\tau_{BG}}$ , where  $t_{BG}$  is the decay time due to the background gas collisions. We extract a decay time of 73(15) ms.

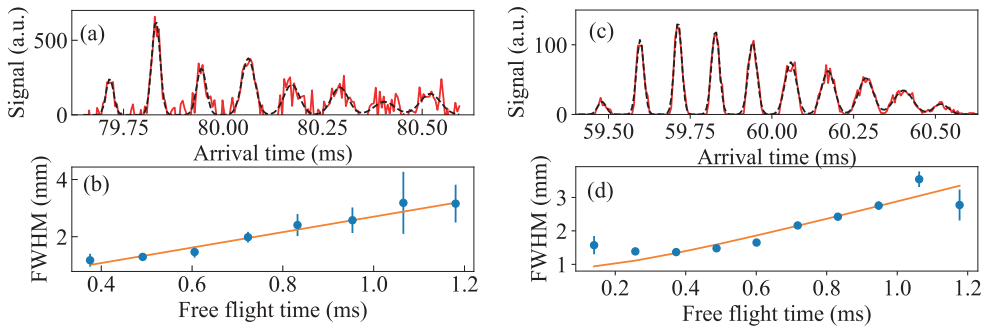


**Figure 6.15** | (a) A zoom-in (in red) of the peak in the experimental TOF profile corresponding to the molecules trapped for 20 ms. The dashed black line is the multi-Gaussian fit to the individual peaks to extract the individual peak widths. (b) A quadratic function,  $\sqrt{(\Delta z)^2 + (\Delta v \cdot t)^2}$  is fit (orange line) to the increment in the widths of the individual peaks (blue scatter points), where  $\Delta z$  and  $\Delta v$  is the longitudinal position and velocity spread of the beam and  $t$  is the free-flight time to reach the detection point after the release from the electric traps. (c) A zoom-in (in red) of the peak in the simulated TOF corresponding to the molecules trapped for 0 ms. The dashed black line corresponds to the multi-Gaussian fit to the individual peaks to extract the widths. (d) A quadratic fit (orange line) to the widths of the individual peaks (blue points).

substructure around the arrival time of the molecules trapped for 20 ms has been shown in Figure 6.15 (a). The dashed black line shows the multiple Gaussian fit to the individual

peak to extract the peak widths. The widths of the eight peaks (blue dots) are shown in Figure 6.15 (b). A quadratic fit to the widths of the adjacent peaks is also shown in dashed orange line as was explained for the case of deceleration. The velocity and the position spread at half maxima are extracted to be 4(1) m/s and 1.0(2) mm respectively. Using  $v_z = \sqrt{8 \ln 2 kT / m}$ , this corresponds to a temperature of about 40(20) mK. With a similar method, the velocity and position spread of the molecular beam obtained from the simulated data is 3(1) and 0.9(2) mm, respectively (see Figure 6.15 (c,d)), which is in reasonable agreement with the values obtained from the experimental data.

## 6.4. Number of molecules

In this section, we estimate the number of molecules that are decelerated to low velocities and that are trapped in the measurements presented in the preceding sections of this chapter. Depending on the size of the molecular packets in the decelerator, their forward velocity and their velocity spreads, only a fraction of the molecules from the moment they are released from the decelerator make it to our detection volume. Further, only a fraction of the total photons counts per shot emitted by the molecules that reach the detection volume is detected based on the collection solid angle ( $\Omega$ ), PMT quantum efficiency (QE) and transmission of the optics assembly (T). Our first task is to determine these fractions.

We have made an analytical model to determine the transfer of molecules from the moment the decelerator is switched off to the detection volume. The distances are well known; 6 mm between the adjacent electric field traps and 10 mm between the end of the decelerator and the detection volume. The detection volume is also well known; it is limited by the size of the detection laser beam (waist 0.7 mm) in one transverse direction, and in the other transverse direction to 1.9 mm, by the magnification factor ( $M = 2.7$ ) of the fluorescence collection system onto the active area of the PMT (5 mm x 5 mm). The average forward velocity of the decelerated molecules from the decelerator is also well known, as it is set by the frequency of the waveforms applied to the ring electrodes inside the decelerator. We see from the guiding measurements at 190 m/s that about 17-19 traps are filled with molecules produced by a single ablation shot.

Relatively less known parameters are the size and velocity spread of the packets of the molecules. From the data analysis presented in section 6.2.3, we have information on the size and velocity spread of the molecules at different final velocities in the longitudinal direction. These results indicate a longitudinal position spread,  $\Delta z = (1-2)$  mm, and a longitudinal velocity spread,  $\Delta v_z = (1-10)$  m/s, where the strongest deceleration strengths lead to smaller packets and smaller velocity spreads. This is expected since the acceptance of the decelerator is somewhat reduced at higher deceleration strengths (a factor of 3 is estimated from the simulations presented in Table 6.1). The transverse size and velocity spread have been discussed in section 6.2.4, where we have to rely on the numerical simulations. We deduced the transverse size of the decelerated beams of the order,  $\Delta y = 1$  mm, and the transverse velocity spread of the order,  $\Delta v_y = 2.2$  m/s, rather independent of the deceleration strength.

We have calculated using an analytical model, the transfer probability of the molecules in the decelerator from the point of release from the electric traps to the detection volume by

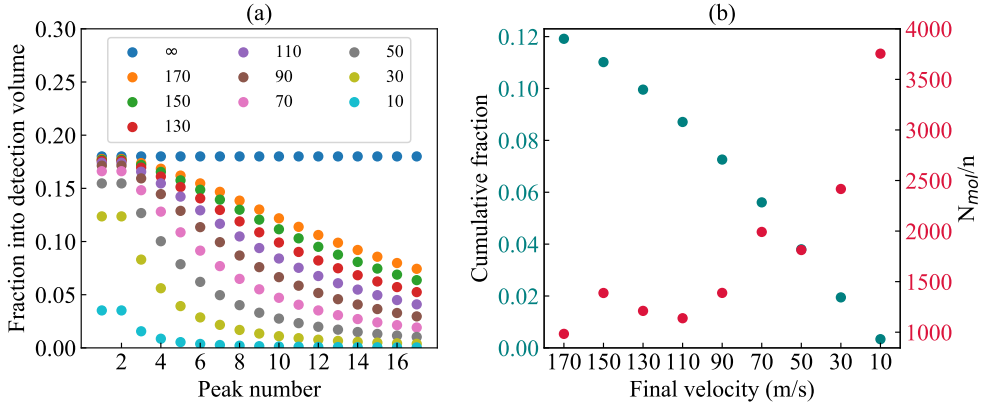


**Figure 6.16** | (a) The fraction of the individual molecular packets (equal weights) within the decelerated signal which enter the detection volume after a free flight from the time of release from the electric field traps till the detection volume for the final velocities between (170-10) m/s. The  $v = \infty$  case is shown for the sake of reference. The maximum fraction is limited at 0.18 due to the detection efficiency. (b) The cumulative weighted sum of the fraction of molecules (green dots) in all the traps that enter the detection volume. The corresponding number of molecules per scattered photon (red dots) for different final velocities are calculated using the Equation 6.2 by taking into account the fluorescence collection efficiency.

taking into account the geometry of the situation. We initiated the model by assuming 17 adjacent traps (of equal weights) which correspond to the molecules in different electric field traps. The second peak is assumed to be the synchronous peak which is mostly the case for all of the experimental data. We used the transverse position and velocities deduced from simulations. The moment of release from the traps is the one when the synchronous molecular packet reaches the end of the decelerator. The results are given in Figure 6.16. It can clearly be seen in panel (a) that the molecules in the traps closest to the detection volume are detected with the highest probability. For the lowest velocities, the effect is dramatic, with most molecules missing the detection volume. This matches the reduction in the number of traps observed in the experiments presented in Figure 6.8.

In Figure 6.16 (b), the total fraction of molecules in all traps that reach the detection volume is shown. It is obtained by a weighted sum of the fractions of molecules from the individual traps that reach the detection volume. The weights are obtained from the guiding measurements at 190 m/s. By combining this number with the total fluorescence collection efficiency, the velocity-dependent number of molecules ( $N_{mol}$ ) per detected photon ( $n$ ) can be determined using the formula:

$$N_{mol} = \frac{S(\text{decelerated})}{T \times QE \times \Omega/4\pi \times f \times n} = \frac{S(\text{decelerated})}{0.83 \times 0.39 \times 0.94/4\pi \times f \times n} = \frac{42 * S(\text{decelerated})}{f * n}, \quad (6.2)$$

Final average velocity (m/s)	Peaks in the substructure	Photon counts S(total)	Photon counts S(decelerated)
170	17	20.78(5)	2.79(2)
150	19	25.03(5)	3.64(2)
130	17	26.75(5)	2.87(2)
110	17	27.68(5)	2.36(2)
90	17	22.51(5)	2.40(2)
70	14	29.27(5)	2.66(2)
50	11	24.12(5)	1.64(1)
30	6	23.74(5)	1.12(1)
10	-	23.18(5)	0.30(1)

**Table 6.4** | The number of photon counts (averaged over 12000 shots) for a single pulse of SrF molecules (absorption 1%) decelerated to different final velocities, detected by the laser-induced fluorescence in a single rotational state of the electronic ground state  $X^2\Sigma^+(v = 0, N = 1)$ . The systematic uncertainties arising from the fluctuations in the number of molecules produced in the source, long term detection laser frequency drifts are primarily common to all measurements and are estimated to be below 20%.

where  $S(\text{decelerated})$  is the number of detected photons per shot for molecules decelerated to various final velocities, reported in Table 6.4. This product results in an estimated 1000-3700 molecules/shot, with the highest number for the lowest velocity [see Figure 6.16(b)]. During these measurements the amplitude of the absorption signal from the source was 1.0%, and the numbers are based on the assumption that for all velocities, we have scattered a single photon per molecule ( $n = 1$ ).

The order of magnitude roughly matches the expectations based on the number of molecules produced in the source (out of the total molecules produced ( $\sim 10^9$ ), a fraction  $10^{-5}$  is captured into the decelerator (Table 6.1)), and also is in reasonable agreement with the numbers estimated from the deceleration measurements presented in Chapter 5. However, the increase in the molecule numbers at lower velocities is counter-intuitive. The increase may be due to prolonged interaction time at low velocities, which causes the scattering of multiple photons per molecule ( $n > 1$ ). Another reason would be that the increase is caused by the constant size and velocity spread currently used for the molecular packets over the different velocities. In other words, the reduced phase-space acceptance of the decelerator at larger deceleration strengths is not taken into account in the analytical model. Of course, the input parameters could now be tuned to make the numbers match our expectation but since there are so many unknowns, instead of doing that we'd rather show the dependence of the number of molecules per scattered photon on the transverse position ( $\Delta y$ ) and transverse velocity ( $\Delta v_y$ ). This is shown in Figure 6.17.

For the data on the trapped molecules, the situation is rather similar. Our estimate of the initial transverse position and velocity spread is  $\Delta y = 1.0$  mm and  $\Delta v_y = 2.0$  m/s, based on the simulations for a velocity during the free flight of 50 m/s as the molecules were accelerated to this velocity after in-decelerator trapping (see Table 6.3). We use the analytical model for transfer to translate the signal intensities in Table 6.5 to corresponding molecule numbers.



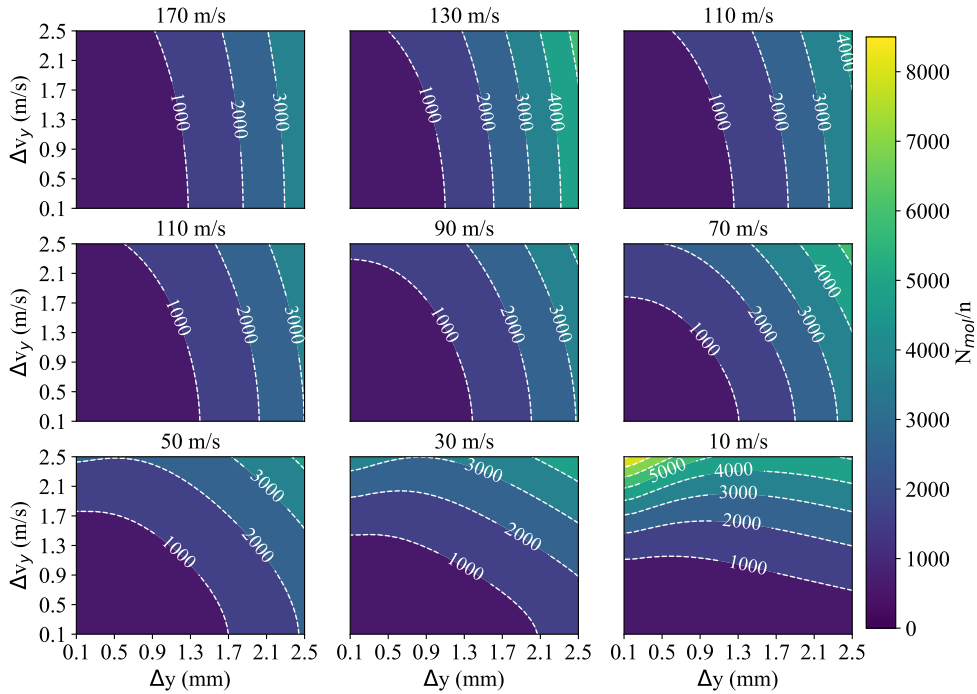


**Figure 6.17** | The number of molecules per scattered photon ( $N_{mol}/n$ ) as a function of the transverse position spread ( $\Delta y$ ) and velocity spread ( $\Delta v_y$ ) of the SrF molecular beams at the time of release from the electric traps inside the decelerator, for deceleration to different final velocities between 170 m/s and 10 m/s from an initial velocity of 190 m/s.

Trap time $\Delta t$ (ms)	Peaks in the substructure	Photon counts S(total)	Photon counts S(decelerated+trapped)
0	8-9	13.40(1)	0.38(9)
10	7-8	13.45(1)	0.26(7)
20	8-9	15.30(1)	0.32(8)
30	5-6	14.97(1)	0.31(8)
40	5-6	15.79(1)	0.24(6)
50	5-6	14.83(1)	0.18(5)

**Table 6.5** | The number of photon counts per shot averaged over 72000 shots (absorption 0.5%) detected by the PMT in a single rotational state of the electronic ground state  $X^2\Sigma^+(v = 0, N = 1)$  of SrF molecules held for different times in the electric traps inside the decelerator. The quoted uncertainties are statistical only. The systematic uncertainties arising from the fluctuations in the number of molecules produced in the source, long term detection laser frequency drifts are primarily common to all measurements and are estimated to be below 20%.

The weighted cumulative fraction for the individual traps is 4.6%. Using Equation 6.2, we found that the number of molecules per scattered photon ( $N_{mol}/n$ ) decreases from 350 for a trap time of 0 ms to 160 molecules for a trap time of 50 ms, respectively. Combined with the fact that during these measurements, the amplitude of the absorption signal was 0.5% (against 1% absorption for the deceleration measurements), the numbers give a consistent picture. Overall, we can currently produce on the order  $10^3$  molecules/shot ( $n=1$ ) for a beam intensity that leads to 1% absorption amplitude at the cryogenic source.

## 6.5. Conclusion and outlook

In conclusion, we demonstrated the deceleration and trapping of a SrF molecular beam in the state  $X^2\Sigma^+(v = 0, N = 1)$  produced in a cryogenic buffer gas source in a 4.5 m-long TWSD. SrF molecules with an average velocity of 190 m/s are decelerated down to arbitrarily low velocities, and are brought to a standstill and trapped for about 50 ms in a series of consecutive electric wells inside the decelerator. In the future, we plan to improve the detection efficiency. Potential ways to increase the molecular numbers also include implementing a better matching of the cryogenic source to the decelerator with a hexapole guide, by optically pumping the molecules into the state of interest before they enter the decelerator [161], and by increasing the electric field strength of the decelerator to allow deceleration in a higher rotational state like ( $N = 2$ ) state, which has a larger Stark shift in comparison to  $N = 1$  rotational state.

Although the SrF molecule is also amenable to laser cooling and trapping, the technique we employ here relies only on its Stark shift. Therefore, this method gives access to molecular species for which laser cooling is not feasible, opening the prospects for controlling more diverse and complex molecular species desirable for many applications in quantum science and technology and new physics searches. Also lighter molecules with an unfavourable Stark shift over mass ratio [268] can now be decelerated and trapped. The sensitivity to the eEDM, which scales with a higher power of the atomic number [53], furthermore increases linearly with the long interaction time offered by cold and slow beams of heavy molecules. We will therefore apply the principle of the method demonstrated here to BaF, which is a prime candidate to probe physics beyond the Standard Model of particle physics [90].

# Summary and Outlook

The Standard Model (SM) of elementary particles gives a very elegant description of the world around us [1], but it cannot explain everything [269]. Many fundamental questions remain unanswered by the SM, for example, why is there an abundance of matter over anti-matter despite the laws of physics treating both nearly equivalently, what are dark matter and dark energy. Many beyond the Standard Model (BSM) theories which seek to answer these questions predict new particles with masses up to several  $\text{TeV}/c^2$  [20] and/or light axions with masses  $\sim \text{meV}$  [21]. The search for yet undiscovered massive particles (at energy scales  $\sim \text{TeV}$ ) is conducted in a direct way at the Large Hadron Collider at CERN. Protons are made to collide at high energies in the  $\text{TeV}$  range and the particles produced are detected or inferred from the decay products. The measurement of the electron's electric dipole moment (eEDM) is one complementary approach to the collider experiments for the discovery of high energy particles. It is predicted that the interaction of the electron with the yet undiscovered massive particles imparts it an electric dipole moment [36]. According to the SM, the value of the eEDM should be less than  $10^{-38} \text{ e.cm}$  [36]. However, many BSM theories predict the value of the eEDM many orders of magnitude higher, which brings it into the range of the current experimental sensitivity. Any non-zero measurement of an EDM of an electron in a range higher than that predicted by the Standard Model would be a signature of new physics.

## Electron's electric dipole moment searches using molecules

The work presented in this thesis has been done as a part of the NL-eEDM collaboration. Within the collaboration, we aim to make a precision measurement of the eEDM using BaF molecules [90]. The individual chapters in this thesis describe crucial steps on the path from a conceptual design towards a precision measurement. There is a rich tradition in the attempts to measure the eEDM. The history of eEDM experiments is almost seven decades old (see Figure 1.1, **Chapter 1**). Most of the eEDM searches are currently pursued with heavy paramagnetic polar molecular systems. There is an enhancement in the sensitivity to the

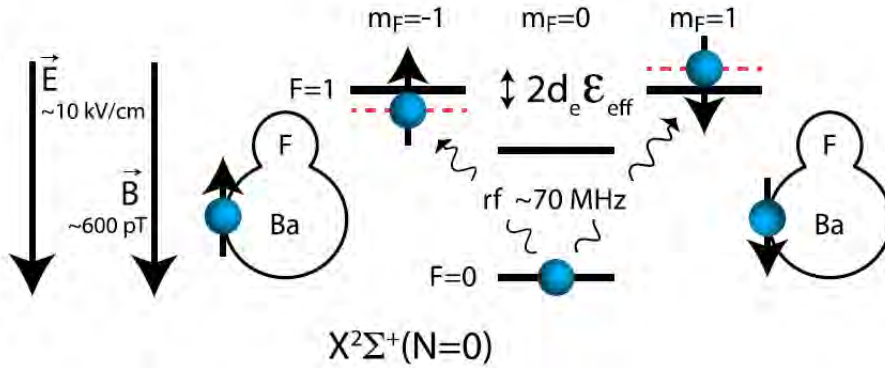


**Figure 7.1** | *Measurement strategy: The molecule is prepared in a pure spin state, such as the  $|F, m_F\rangle = |0, 0\rangle$  hyperfine state of  $X^2\Sigma^+$  ( $\nu=0$ ,  $N=1$ ) electronic level (for e.g. in heavy paramagnetic molecular systems like BaF and YbF). The molecule is prepared further in a superposition of hyperfine substates,  $m_F = -1$  and  $m_F = 1$  of the  $F = 1$  [ $X^2\Sigma^+$  ( $\nu=0$ ,  $N=1$ )] hyperfine state. The molecule evolves for some time (called the interaction time) in the electric and magnetic fields and accumulates a phase difference in its state due to Zeeman and Stark effects. The difference in the total phase for the parallel and antiparallel orientation of the magnetic and electric field is proportional to the product of the eEDM magnitude and the effective electric field of the molecule. The phase accumulated during the interaction time can be read out by projecting the superposition state back onto the  $X^2\Sigma^+$  ( $\nu=0$ ,  $N=1$ ,  $F=0$ ) state and then collecting fluorescence by exciting the molecules in that state to a higher-lying electronic state.*

electron EDM by many orders of magnitude in heavy paramagnetic atomic and molecular systems due to relativistic effects [54]. The sensitivity of such a table-top precision experiment with polar molecules can be maximised by using a high beam flux, a long interaction time and a long coherence time (see Equation 1.11, **Chapter 1**). For a beam experiment, we would like to start with an intense source of molecules. By reducing the velocity of the beam, we can get a long coherent interaction time for a given length of the interaction zone.

The experimental concept for the measurement of the eEDM using molecules is illustrated in Figure 7.1. A molecule is prepared in a superposition of hyperfine states. This state accumulates a phase difference during the interaction with the electric and magnetic fields. The eEDM signal is detectable through a difference in the total accumulated phase for the parallel and anti-parallel orientation of the magnetic and electric fields. These steps shown in Figure 7.1 are referred to as the state preparation, interaction zone, state analysis and optical readout in the planned NL-eEDM experiment setup (see Figure 7.2).

### NL-eEDM experimental setup

In the planned NL-eEDM experimental setup, we will produce the BaF molecular beam in a cryogenic buffer gas source. The beams produced in the cryogenic source are more

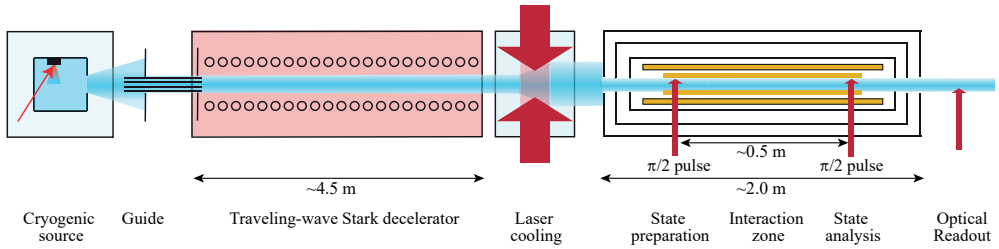


**Figure 7.2** | Schematic overview of the planned experimental setup [90]. The molecular beam of BaF travels from left to right. A beam of BaF molecules with a velocity of 190 m/s created in the cryogenic source will subsequently be decelerated to 30 m/s in a traveling-wave Stark decelerator. A laser cooling section will reduce the transverse velocity spread of the beam, to limit the beam from spreading out during the 15 ms transit through the 0.5 m interaction zone. For a horizontal beam at such low velocities, the gravitational fall needs some addressing while launching the beam into the interaction zone. In the magnetically shielded interaction zone, the molecules are prepared in a superposition of the hyperfine substates,  $X^2\Sigma^+$  ( $\nu=0$ ,  $N=0$ ,  $F=1$ ,  $m_F=\pm 1$ ), which builds up a phase difference in the presence of an electric and a magnetic field. For the state analysis, the superposition state is projected back onto the  $X^2\Sigma^+$  ( $\nu=0$ ,  $N=0$ ,  $F=0$ ,  $m_F=0$ ) state. Readout of the state will be done via laser-induced fluorescence detection.

intense and also have a lower longitudinal velocity than the ones produced in conventional supersonic sources [92]. This will ensure a high flux of molecules and also a large coherent interaction time. The cryogenic beam with an average longitudinal velocity of 190-200 m/s will be decelerated in a 4.5 m long traveling-wave Stark decelerator (TWSD) to a final velocity of 30 m/s. To stop the beam from diverging and ensure that the maximum number of molecules from the decelerator enter the interaction zone, we will transversally laser cool the beam. With the long coherent interaction times obtainable in a cold beam of BaF, we aim to achieve a sensitivity of  $5 \times 10^{-30}$  e-cm in the eEDM measurement [90]. Preparation of cold beams requires a good understanding of the energy level structure of the BaF molecule, specifically for the preparation of the superposition state and for the laser cooling of the molecule. The theory of the molecular level structure is discussed in detail in **Chapter 2**.

### Preparation of slow, cold and intense molecular beams

The work presented in this thesis has primarily been done with the aim to produce intense and slow molecular beams for the final eEDM measurement. I worked on the construction of a supersonic source of BaF and SrF molecules. This was achieved by combining the expansion of a carrier gas (a mixture of 2%  $\text{SF}_6$  and 98% Ar) from an Even-Lavie valve with laser ablation of a barium/strontium target to produce SrF and BaF molecular beams. The supersonic source is being used to perform spectroscopy on the BaF beam and later will be used for the testing of the interaction zone. The results from the source are discussed in **Chapter 3**.

Within the collaboration, theoretical investigations of the ground and the first excited electronic state of BaF were carried out in the framework of relativistic Fock-space coupled

cluster and multireference configuration interaction methods [165]. This included the calculation of the Franck-Condon factors (FCFs) and transition dipole moments (TDMs) between the different states. The transition  $A^2\Pi_{1/2}(\nu = 0) \leftarrow X^2\Sigma^+(\nu = 0, N = 1)$  was found to be suitable for the laser cooling of BaF, with highly diagonal FCFs. Together with a fellow Ph.D. student, I did a measurement of the lifetime of one of the low-lying excited states of the BaF involved in the main laser cooling of BaF. The results of that measurement are presented in **Chapter 4**. The lifetime of the  $A^2\Pi_{1/2}(\nu = 0)$  and  $A^2\Pi_{3/2}(\nu = 0)$  states were determined to be 57.1(3) ns and 47.9(7) ns, respectively. These results will also serve as a benchmark for current molecular energy level structure calculations.

In **Chapter 5**, I present the results for the deceleration of a cryogenic beam of SrF molecules in a 4 m long TWSD. In the past, only molecular beams from supersonic sources have been decelerated in a Stark decelerator. The combination of a cryogenic source with a decelerator will lead to new possibilities, e.g the deceleration of beams of heavy molecules to low velocities. These slow beams of heavy molecules will be interesting for many BSM physics searches. The cryogenic source emit a longer molecular pulse in comparison to the pulse from a supersonic source. As a result, multiple co-moving electric field minima are filled which have to be all decelerated to the same final velocity. We have decided to first work with SrF molecules over BaF molecules for practical reasons. SrF molecules have an energy level structure similar to the BaF molecules. BaF is heavier than SrF. The main components of the experimental setup are discussed in detail in the former sections of this chapter: the cryogenic source, the principle and the design of the TWSD and the laser-induced fluorescence detection. In the latter sections, the results for the guiding and deceleration of the SrF molecules from the source are presented. The molecules are detected at a distance of 18 cm from the last ring of the decelerator. The molecules decelerated to a longitudinal velocity of 60 m/s from an initial velocity of 190 m/s were detected. The beams with a longitudinal velocity below 60 m/s could not be detected because molecules transversally diffuse away before reaching the detection spot.

As a consequence of the results in **Chapter 5**, we moved the laser-induced fluorescence detection spot for the SrF molecules from 18 cm to 1 cm from the last ring electrode of the decelerator. Further, we add an additional module of  $\sim 0.5$  m length to this decelerator. In **Chapter 6**, the results for the deceleration of the SrF molecules in 4.5 m long decelerator is presented. With this combination, we demonstrate that beams of SrF molecules can be decelerated to a complete standstill. We can hold the molecules in the stationary electric field minima in the decelerator and then accelerate the molecules out of the decelerator to detect them. The SrF molecules in the different electric field minima of the decelerator have been held for up to 50 ms. The experimental results compare well with numerical trajectory simulations of the deceleration process. We have estimated the total number of molecules per shot at different final velocities that reach the end of the decelerator to be on the order of 1000.

## Outlook

We are working towards achieving an intense and slow beam of heavy molecules like SrF and BaF with a combination of a cryogenic source and a TWSD, a combination which was unexplored so far. The SrF molecule is the heaviest molecule to be decelerated to zero velocity and trapped. We expect the BaF molecular beam to also be decelerated with similar

(slightly lower) efficiency. We see possibilities to increase the number of molecules decelerated from the TWSD for the eEDM measurement. For the results presented in **Chapters 5 and 6**, the SrF molecules have a free-flight distance of  $\sim 37$  cm between the source and TWSD, which leads to a loss of factor  $\sim 25$  in the number of molecules. A multipole guide can be inserted between the cryogenic source and the TWSD to ensure that the maximum number of molecules from the source enter the TWSD. This improves the matching of the phase-space distribution of the beam to the phase-space acceptance of the TWSD.

Within the collaboration, there is also work ongoing on the voltage upgrade of the decelerator from a maximum amplitude of  $10 \text{ kV}_{\text{pp}}$  to  $20 \text{ kV}_{\text{pp}}$ . Currently, we detect the deceleration of the molecules in the  $N = 1$  rotational state of the vibrational and electronic ground state  $X^2\Sigma^+(\nu = 0)$  of SrF molecule. The maximum Stark shift for the SrF molecule in  $N = 1$  rotational state is  $0.16 \text{ cm}^{-1}$ , whereas it is  $0.56 \text{ cm}^{-1}$  in  $N = 2$  rotational state as shown in Figure 2.5, **Chapter 2**. The SrF molecules in  $N = 1$  rotational state becomes high-field seeking at an electric field strength larger than  $21 \text{ kV/cm}$ . Similarly, the maximum Stark shift of the BaF molecule in  $N = 1$  and  $N = 2$  rotational state is  $0.14 \text{ cm}^{-1}$  and  $0.48 \text{ cm}^{-1}$ , respectively (see Figure 2.6, **Chapter 2**). As a result, provided the voltage sources can be created, it is advantageous to decelerate BaF molecules for the NL-eEDM project in  $N = 2$  rotational state. The molecule numbers can further be increased by optically pumping the molecules from other rotational states to  $N = 2$  rotational state. An additional possibility is to carry out transverse laser cooling of the BaF molecule between the cryogenic source and the TWSD to improve the coupling of the source to the decelerator. In view of the planned NL-eEDM experiment setup, the next step after the deceleration of the cryogenic beam in the TWSD is the transverse laser cooling of the beam.

Based on the results obtained in this thesis on the deceleration of SrF beams, we can estimate the statistical sensitivity of an eEDM measurement that can be achieved with the current flux of the molecular beam (at  $\sim 10^3$  molecules per shot) from the decelerator. Here, we assume that the deceleration of the BaF beam would work very similar to SrF. In the planned experimental setup, we aim to decelerate a total of  $\sim 10^6$  BaF molecules per shot to  $30 \text{ m/s}$  (see [90]). The present intensities of the beam are, hence, three orders of magnitude lower than the intensities we wish to achieve. Based on Equation 1.11, **Chapter 1**, we would obtain a statistical uncertainty of  $2 \times 10^{-28} \text{ e}\cdot\text{cm}/\sqrt{\text{Day}}$  with a BaF beam at  $30 \text{ m/s}$  at a flux comparable to the decelerated SrF beams, against an estimated sensitivity of  $5 \times 10^{-30} \text{ e}\cdot\text{cm}/\sqrt{\text{Day}}$  with the planned setup shown in Figure 7.2.

SrF is an example of a molecule that can be both laser-cooled as well as Stark decelerated [127]. The possibility of laser cooling and Stark-deceleration of BaF has also been investigated [165, 90]. In general, laser cooling can only be applied to molecules with sufficiently closed cycles of transition. Only a handful of molecules besides SrF have been laser-cooled, YO [128], CaF [129, 130], YbF [91] and BaH [131]. This combination of a cryogenic source with the TWSD alone can significantly extend the species of neutral molecules of which slow beams can be created for different purposes like collision studies, precision measurements and trapping experiments. However, to create an intense, slow and cold beam for a highly sensitive eEDM measurement with BaF molecules, we want to use the combination of the transverse laser cooling with the Stark deceleration of cryogenic beams [90]. This combination could potentially also be used to load the beams of heavy molecules into a

magneto-optical trap.



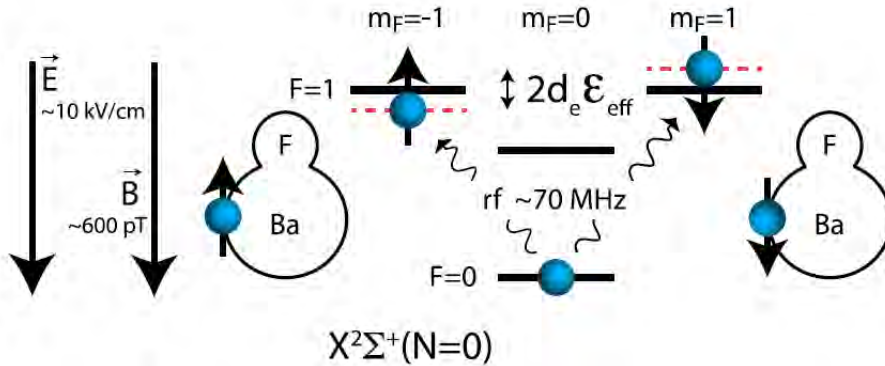
# 8

## Nederlandse Samenvatting

Het standaardmodel (SM) van de deeltjesfysica geeft een elegante beschrijving van de wereld om ons heen [1], maar beschrijft niet alles [269]. Veel fundamentele vragen blijven onbeantwoord door het SM, bijvoorbeeld: waarom is er veel meer materie dan antimaterie, ondanks dat ze bijna gelijk behandeld worden door de fysische wetten en wat zijn donkere energie en donkere materie? Veel buiten het standaardmodel (BSM) theorieën die deze vragen proberen te beantwoorden, voorspellen nieuwe deeltjes met massa's tot enkele  $\text{TeV}/c^2$  [20] en/of lichte axionen met massa's van  $\sim \text{meV}$  [21]. De zoektocht naar de nog te ontdekken massieve deeltjes (met energieën in de orde van  $\text{TeV}$ ) wordt op een directe manier gedaan in de Grote Hadronen-Botser (Large Hadron Collider) bij CERN. Protonen worden met elkaar in botsing gebracht bij energieën in de orde van  $\text{TeV}$  en de geproduceerde deeltjes worden gedetecteerd of afgeleid van andere vervalproducten. Het meten aan het elektrisch dipoolmoment van het elektron (eEDM) is een complementaire benadering ten opzichte van experimenten in botsers voor het ontdekken van hoogenergetische deeltjes. Er is voorspeld dat de interactie van het elektron met de nog te ontdekken hoogenergetische deeltjes leidt tot een eEDM [36]. Volgens het SM van de deeltjesfysica is de waarde van het eEDM kleiner dan  $10^{-38}$  e-cm [36]. Aan de andere kant, voorspellen veel BSM theorieën een eEDM vele ordes van grootte groter, die mogelijk meetbaar is met de huidige experimentele gevoeligheid. Elke niet-nul meetresultaat van het eEDM, hoger dan de waarde voorspeld door het SM, zou een teken zijn van nieuwe fysica.

### Metingen aan het elektron elektrisch dipoolmoment met behulp van moleculen

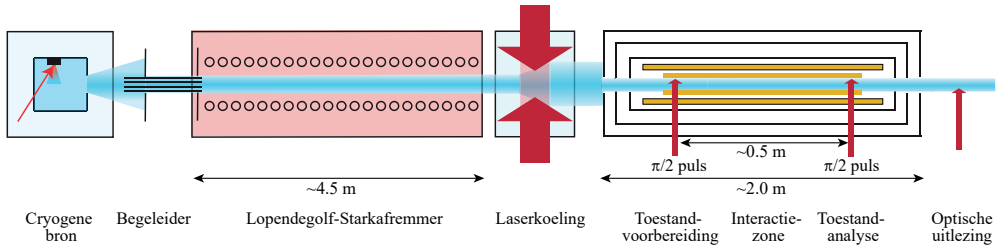
Het werk gepresenteerd in dit proefschrift is verricht als onderdeel van het samenwerkingsverband NL-eEDM. Het doel van dit samenwerkingsverband is het verrichten van een precisiemeting van het eEDM, gebruikmakend van BaF moleculen [90]. De hoofdstukken in dit proefschrift beschrijven cruciale stappen op weg van een conceptontwerp naar een daadwerkelijke precisiemeting. In het verleden zijn tal van pogingen gedaan om het eEDM te meten. De geschiedenis van eEDM-experimenten is bijna 70 jaar oud (zie Figuur 1.1, **Hoofdstuk 1**). Het overgrote deel van de huidige eEDM-metingen wordt verricht met be-



**Figuur 8.1** | Meetconcept: Het molecuul wordt in een wzuivere spintoestand voorbereid, bijvoorbeeld de  $|F, m_F\rangle = |0, 0\rangle$  hyperfijn-toestand van de  $X^2\Sigma^+(\nu = 0, N = 1)$  toestand (bijvoorbeeld in zware, paramagnetische moleculen als BaF en YbF). Het molecuul wordt in een superpositie van hyperfijn-subtoestanden  $m_F = -1$  en  $m_F = 1$  van de  $F = 1$  [ $X^2\Sigma^+(\nu = 0, N = 1)$ ] toestand gebracht. Het molecuul evolueert voor een tijdje in een elektromagnetisch veld (de interactietijd) en een faseverschil bouwt op in de toestand vanwege het Zeeman- en Stark-effect. Het verschil van de opgebouwde faseverschillen voor een parallelle en antiparallelle configuratie van het elektromagnetische veld is proportioneel met de grootte van het eEDM en het effectieve elektrische veld van het molecuul. De opgebouwde fase tijdens de interactietijd kan uitgelezen worden via de projectie van de superpositietoestand op de  $X^2\Sigma^+(\nu = 0, N = 1, F = 0)$  toestand en het meten van de fluorescentie na het aanslaan van de moleculen naar een hogergelegen elektronische toestand.

hulp van zware, paramagnetische, polaire, moleculen. Er is een versterking van vele ordes van grootte in de gevoeligheid van het eEDM als men gebruik maakt van paramagnetische atoom- en molecuulsystemen, dit komt door relativistische effecten [54]. De gevoeligheid van een dergelijke kleinschalige precisie-experiment met polaire moleculen kan geoptimaliseerd worden door gebruik te maken van een groot aantal deeltjes in een molecuulbundel, een lange interactietijd en een lange coherentietijd (zie vergelijking 1.11, **Hoofdstuk 1**). Voor een bundelexperiment is het beginnen met een intense bundel van moleculen wenselijk. Het reduceren van de snelheid van de bundel leidt tot een lange coherente interactietijd bij een bepaalde lengte van de interactiezone.

Het experimentele concept voor de meting van het eEDM met moleculen wordt geïllustreerd in Figuur 8.1. Een molecuul wordt in een superpositie van hyperfijn-toestanden gebracht, in deze toestand ontstaat een toenemende faseverschil tijdens de interactie met een elektrisch en magnetisch veld. Uit het verschil tussen de opgebouwde faseverschillen in een parallelle en antiparallelle configuratie van de velden kan het eEDM afgeleid worden. The stappen in Figuur 8.1 worden aangeduid als: toestandvoorbereiding, interactiezone, toestandanalyse en optische uitlezing in de geplande NL-eEDM experimentele opstelling (zie Figuur 8.2).



**Figuur 8.2** | Een Schematische weergave van de geplande experimentele opstelling [90]. De molecuulbundel van BaF beweegt van links naar rechts. De cryogene bron creëert molecuulbundels van BaF met een snelheid van 190 m/s, deze worden daarna afgeremd in een lopendegolf-Starkafremmer tot een snelheid van 30 m/s. Daarna wordt middels laserkoeling de transversale spreiding van de bundel gereduceerd om de transversale spreiding tijdens de 15 ms durende reis in de 0.5 m lange interactiezone te beperken. Bij een horizontale bundel die met een dergelijke lage snelheid door de interactiezone reist, moet er rekening gehouden worden met afbuiging door de zwaartekracht van de aarde. In de magnetisch afgeschermd interactiezone worden de moleculen in een superpositie van hyperfijn-subtoestanden gebracht  $X^2\Sigma^+(\nu = 0, N = 1, F = 0, m_F = \pm 1)$ , in de aanwezigheid van een elektromagnetisch veld zorgt dit voor de opbouw van een faseverschil in de toestand. Om de toestand te analyseren wordt de superpositietoestand geprojecteerd op de  $X^2\Sigma^+(\nu = 0, N = 1, F = 0, m_F = 0)$  toestand. Voor het uitlezen van de toestand, wordt lasergeïnduceerde fluorescentie gebruikt.

## De NL-eEDM experimentele opstelling

In de geplande NL-eEDM experimentele opstelling zullen de BaF molecuulbundels geproduceerd worden met een cryogene buffergasbron. The bundels geproduceerd met de cryogene bron zijn intens en hebben een lagere longitudinale snelheid vergeleken met bundels geproduceerd met conventionele supersonische bronnen [92]. Dit garandeert een grote hoeveelheid moleculen en een lange coherente interactietijd. De cryogene bundel met een gemiddelde longitudinale snelheid van 190-200 m/s zal worden afgeremd in een 4.5 m lange lopendegolf-Starkafremmer (afremmer) tot een eindsnelheid van 30 m/s. Om divergentie van de bundel te beperken en ervoor te zorgen dat zoveel mogelijk moleculen na de afremmer de interactiezone bereiken, zal de bundel transversaal lasergekoeld worden. Door de haalbaarheid van lange coherente interactietijden met een koude bundel van BaF verwachten we een meetgevoeligheid van  $5 \times 10^{-30}$  e-cm in de meting van het eEDM [90]. Het voorbereiden van koude bundels vereist goede kennis van de energiestructuur van het BaF molecuul, in het bijzonder voor het voorbereiden van de superpositietoestand en het lasergekoelen van het molecuul. Een gedetailleerde beschrijving van de theorie omtrent de energiestructuur wordt gegeven in **Hoofdstuk 2**.

## Vorbereiding van langzame, koude, intense molecuulbundels

Het werk gepresenteerd in dit proefschrift is voornamelijk gedaan om intense, langzame molecuulbundels te produceren voor een uiteindelijke eEDM-meting. Ik heb gewerkt aan het bouwen van een supersonische bron voor BaF en SrF moleculen. Dit is bereikt door de

expansie van een buffergas (een mengsel van 2% SF<sub>6</sub> en 98% Ar) uit een Even-Lavie klep te combineren met de ablatie van een barium of strontium doelwit om respectievelijk BaF of SrF molecuulbundels te produceren. De supersonische bron wordt gebruikt om spectroscopiemetingen te doen aan de BaF-bundel en zal later gebruikt worden om de interactiezone te testen. De resultaten verkregen met de bron worden besproken in **Hoofdstuk 3**.

In het samenwerkingsverband NL-eEDM zijn theoretische studies gedaan naar de elektronische grondtoestand en eerste aangeslagen toestand van BaF, gebruikmakend van relativistische Fock-ruimte gekoppelde cluster (Fock-space coupled cluster) en meervoudige referentieconfiguratie (multireference configuration) interactiemethoden [165]. Dit bevat ook de calculatie van de Franck-Condon factoren (FCF's) en de transitiedipoolmomenten (TDM's) tussen de verschillende toestanden. De overgang tussen  $A^2\Pi_{1/2}(\nu = 0)$  en  $X^2\Sigma^+(\nu = 0, N = 1)$  is geschikt gebleken voor het laserkoelen van BaF door de zeer diagonale FCF's. Samen met mijn collega heb ik een meting gedaan aan de levensduur van één van de laagenergetische aangeslagen toestanden van BaF, deze toestand is betrokken bij het laserkoelen van BaF. De resultaten van deze meting zijn besproken in **Hoofdstuk 4**. De meetresultaten voor de levensduur van de  $A^2\Pi_{1/2}(\nu = 0)$  en  $A^2\Pi_{3/2}(\nu = 0)$  toestanden zijn respectievelijk, 57.1(3) ns en 47.9(7) ns. Deze resultaten dienen als referentie voor andere calculaties aan de energiestructuur van het molecuul.

In **Hoofdstuk 5**, bespreek ik de resultaten van de afremming van een cryogene SrF molecuulbundel door een 4 m lange lopendegolf-Starkafremmer. In het verleden werden alleen molecuulbundels uit een supersonische bron afgeremd in een Starkafremmer. De combinatie van een cryogene bron en een Starkafremmer biedt nieuwe mogelijkheden, bijvoorbeeld het afremmen van zware molecuulbundels tot lage snelheden. Deze langzame molecuulbundels zullen interessant zijn voor verschillende onderzoeken naar BSM-fysica. In het algemeen zijn pulsen van molecuulbundels uit een cryogene bron langer dan die uit een supersonische bron. Het gevolg is dat meerdere meebewegende elektrische veldminima gevuld worden, welke allemaal tot dezelfde eindsnelheid afgeremd moeten worden. Om praktische redenen hebben we besloten om eerst met SrF moleculen te werken in plaats van BaF. SrF en BaF moleculen hebben een vergelijkbare energiestructuur, maar BaF is zwaarder dan SrF. De hoofdcomponenten van de experimentele opstelling zijn gedetailleerd besproken in de eerder paragrafen van dit hoofdstuk: de cryogene bron, de werking en ontwerp van de Starkafremmer, en de laser geïnduceerde fluorescentie detectie. In de latere paragrafen worden de resultaten van de begeleiding en afremming van SrF moleculen uit de bron gepresenteerd. De moleculen worden 18 cm na de laatste ring van de afremmer gedetecteerd. Moleculen die longitudinaal zijn afgeremd van 190 m/s naar 60 m/s werden gedetecteerd. Moleculen met lagere eindsnelheden konden niet gedetecteerd worden vanwege een te grote transversale spreiding van de bundel voordat deze het detectiepunt bereikt.

Als gevolg van de resultaten in **Hoofdstuk 5** hebben we de plek van lasergeïnduceerde fluorescentiedetectie van 18 cm naar 1 cm na de laatste ringelektrode van de afremmer verplaatst. Daarnaast hebben we een extra afremmodule van ~0.5 m toegevoegd aan de afremmer. In **Hoofdstuk 6** worden de afremresultaten voor SrF moleculen in een 4.5 meter lange afremmer weergegeven. Met deze opstelling laten we zien dat bundels van SrF moleculen helemaal tot stilstand gebracht kunnen worden. De moleculen kunnen in stationaire elektrisch veldminima gehouden worden om ze vervolgens te versnellen uit de

afremmer voor detectie. Het was mogelijk om de moleculen tot 50 ms lang vast te houden in de minima. De experimentele resultaten komen overeen met resultaten van numerieke trajectsimulaties van het afremproces. We hebben uitgerekend dat er aan het einde van de afremmer ongeveer duizend tot enkele duizenden moleculen worden gedetecteerd per puls voor verschillende eindsnelheden.

## Vooruitzicht

We werken toe naar een intense, langzame bundel van zware moleculen zoals SrF en BaF middels aan combinatie van een cryogene bron en een lopendegolf-Starkafremmer. Deze combinatie is niet eerder onderzocht. SrF is het zwaarste molecuul dat tot nog toe afgeremd en ingevangen is. De verwachting is dat BaF moleculen met een vergelijkbare (iets lagere) efficiëntie afgeremd kunnen worden. We verwachten dat het mogelijk is om het aantal afgeremde moleculen in de Starkafremmer te vergroten voor de eEDM-meting. Voor de resultaten gepresenteerd in **Hoofdstuk 5** en **Hoofdstuk 6** geldt dat de vrije vluchtafstand tussen de bron en de afremmer  $\sim 37$  cm is, dit leidt tot een factor  $\sim 25$  reductie in het aantal moleculen. Om de laatstgenoemde reductie te voorkomen kan een meerpolige begeleider tussen de bron en afremmer geplaatst worden. Dit zorgt ook voor een betere overlapping tussen de faseruimteverdeling van de bundel en de acceptatie van de afremmer.

Binnen het samenwerkingsverband NL-eEDM wordt ook gewerkt aan het aanpassen van het voltage op de ringen van de afremmer van maximaal  $10 \text{ kV}_{\text{pp}}$  naar  $20 \text{ kV}_{\text{pp}}$ . Op dit moment worden de moleculen in de  $N = 1$  rotationele toestand van de grond vibrationele en elektronische toestand,  $X^2\Sigma^+(\nu = 0)$ , van het SrF molecuul gemeten. De maximale Starkverschuiving in de  $N = 1$  rotationele toestand is  $0.16 \text{ cm}^{-1}$  en  $0.56 \text{ cm}^{-1}$  in de  $N = 2$  toestand, zoals te zien is in Figuur 2.5 van **Hoofdstuk 2**. De SrF moleculen in de  $N = 1$  rotationele toestand worden hoogveldzoekend bij een elektrisch veld groter dan  $21 \text{ kV/cm}$ . Op dezelfde manier is de Starkverschuiving van BaF in de  $N = 1$  en  $N = 2$  rotationele toestanden respectievelijk  $0.14 \text{ cm}^{-1}$  en  $0.48 \text{ cm}^{-1}$  (zie Figuur 2.6, **Hoofdstuk 2**). Als gevolg hiervan is het voordeliger om BaF moleculen in de  $N = 2$  toestand af te remmen, onder de aanname dat de benodigde voltagebronnen aanwezig zijn. Het aantal beschikbare moleculen kan vergroot worden door moleculen in andere rotationele toestanden optisch te pompen naar de  $N = 2$  toestand. Een andere mogelijkheid is het transversaal laserkoelen van de BaF moleculen om de koppeling tussen de bron en afremmer te verbeteren. Na de afremming van de cryogene bundel is de volgende stap in de geplande NL-eEDM opstelling het transversaal laserkoelen van de bundel.

Aan de hand van de in dit werk verkregen aantal moleculen ( $\sim 10^3$  moleculen per puls) na het afremmen van SrF bundels kan een benadering gemaakt worden van de te verwachten statistische gevoeligheid van een eEDM-meting. Hier nemen we aan dat het afremmen van de BaF bundel op dezelfde manier verloopt als het afremmen van de SrF bundel. Voor de geplande experimentele opstelling is het de bedoeling om  $\sim 10^6$  BaF moleculen per puls af te remmen tot  $30 \text{ m/s}$  (zie [90]). Het huidige aantal moleculen is dus 3 ordes van grootte kleiner dan gepland. Gebruikmakend van vergelijking 1.11 (**Hoofdstuk 1**) resulteert dit in een statistische onzekerheid van  $2 \times 10^{-28} \text{ e-cm} / \sqrt{\text{Dag}}$  met een BaF bundel van  $30 \text{ m/s}$  (uitgaande van dezelfde flux als van de SrF bundels) tegenover een geplande gevoeligheid

van  $5 \times 10^{-30}$  e·cm/ $\sqrt{\text{Dag}}$  met de opstelling in Figuur 8.2.

SrF is een voorbeeld van een molecuul dat zowel lasergekoeld kan worden als afgeremd kan worden met een Starkafremmer [127]. Het laserkoele en Starkafremmen van BaF is ook onderzocht [165, 90]. In het algemeen kunnen alleen moleculen met een afdoende gesloten transitiecyclus lasergekoeld worden. Naast SrF zijn er tot nog toe maar een klein aantal andere molecuulsoorten lasergekoeld: YO [128], CaF [129, 130], YbF [91] en BaH [131]. De combinatie van een Starkafremmer en een cryogene bron maakt het mogelijk meer neutrale molecuulsoorten af te remmen voor verschillende doeleinden zoals botsingstudies, precisiemetingen en invangexperimenten. Om een intense, langzame, koude bundel BaF moleculen te maken voor een zeer gevoelige eEDM-meting willen we transversaal laserkoele combineren met het Starkafremmen van cryogene bundels [90]. Deze combinatie kan mogelijk ook gebruikt worden om een magneto-optische val te laden met zware moleculen.

# Bibliography

- [1] W. N. Cottingham and D. A. Greenwood, *An introduction to the standard model of particle physics* (Cambridge University Press, 2007).
- [2] P. W. Higgs, “Broken symmetries and the masses of gauge bosons”, *Phys. Rev. Lett.* **13**, 508 (1964).
- [3] G. S. Guralnik, C. R. Hagen, and T. W. B. Kibble, “Global conservation laws and massless particles”, *Phys. Rev. Lett.* **13**, 585 (1964).
- [4] F. Englert and R. Brout, “Broken symmetry and the mass of gauge vector mesons”, *Phys. Rev. Lett.* **13**, 321 (1964).
- [5] S. L. Glashow, “Partial-symmetries of weak interactions”, *Nucl. Phys.* **22**, 579 (1961).
- [6] S. Weinberg, “A model of leptons”, *Phys. Rev. Lett.* **19**, 1264 (1967).
- [7] H. D. Politzer, “Reliable perturbative results for strong interactions?”, *Phys. Rev. Lett.* **30**, 1346 (1973).
- [8] D. J. Gross and F. Wilczek, “Ultraviolet behavior of non-abelian gauge theories”, *Phys. Rev. Lett.* **30**, 1343 (1973).
- [9] J. J. Aubert, U. Becker, P. J. Biggs, J. Burger, M. Chen, G. Everhart, P. Goldhagen, J. Leong, T. McCorriston, T. G. Rhoades, M. Rohde, S. C. C. Ting, S. L. Wu, and Y. Y. Lee, “Experimental observation of a heavy particle  $J$ ”, *Phys. Rev. Lett.* **33**, 1404 (1974).
- [10] J. E. Augustin *et al.*, “Discovery of a narrow resonance in  $e^+e^-$  annihilation”, *Phys. Rev. Lett.* **33**, 1406 (1974).
- [11] S. W. Herb *et al.*, “Observation of a dimuon resonance at 9.5 GeV in 400-GeV proton-nucleus collisions”, *Phys. Rev. Lett.* **39**, 252 (1977).
- [12] M. L. Perl *et al.*, “Evidence for anomalous lepton production in  $e^+ - e^-$  annihilation”, *Phys. Rev. Lett.* **35**, 1489 (1975).
- [13] D. P. Barber *et al.*, “Discovery of three-jet events and a test of quantum chromodynamics at PETRA”, *Phys. Rev. Lett.* **43**, 830 (1979).
- [14] G. Arnison *et al.*, “Experimental observation of lepton pairs of invariant mass around 95 GeV/c<sup>2</sup> at the CERN SPS collider”, *Phys. Lett. B* **126**, 398 (1983).
- [15] J. J. Aubert *et al.*, “The ratio of the nucleon structure functions  $F_2^N$  for iron and deuterium”, *Phys. Lett. B* **123**, 275 (1983).
- [16] S. Abachi *et al.*, “Observation of the top quark”, *Phys. Rev. Lett.* **74**, 2632 (1995).
- [17] F. Abe *et al.*, “Observation of top quark production in  $\bar{p}p$  collisions with the collider detector at fermilab”, *Phys. Rev. Lett.* **74**, 2626 (1995).

- [18] K. Kodama *et al.*, “Observation of tau neutrino interactions”, *Phys. Lett. B* **504**, 218 (2001).
- [19] G. Aad *et al.*, “Observation of a new particle in the search for the standard model higgs boson with the ATLAS detector at the LHC”, *Phys. Lett. B* **716**, 1 (2012).
- [20] J. L. Feng, “Naturalness and the status of supersymmetry”, *Annu. Rev. Nucl.* **63**, 351 (2013).
- [21] D. J. E. Marsh, “Axion cosmology”, *Phys. Rep.* **643**, 1 (2016).
- [22] R. H. Sanders and S. S. McGaugh, “Modified newtonian dynamics as an alternative to dark matter”, *Annu. Rev. Astro.* **40**, 263 (2002).
- [23] K. P. Jungmann, “Experimental tests of fundamental symmetries: an overview”, *Hyperfine Interact.* **228**, 21 (2014).
- [24] J. Bailey, K. Borer, F. Combley, H. Drumm, F. J. M. Farley, J. H. Field, W. Flegel, P. M. Hattersley, F. Krienen, F. Lange, E. Picasso, and W. von Rüden, “The anomalous magnetic moment of positive and negative muons”, *Phys. Lett. B* **68**, 191 (1977).
- [25] J. Bailey, K. Borer, F. Combley, H. Drumm, F. J. M. Farley, J. H. Field, W. Flegel, P. M. Hattersley, F. Krienen, F. Lange, E. Picasso, and W. von Rüden, “New limits on the electric dipole moment of positive and negative muons”, *J. Phys. G: Nucl. Phys.* **4**, 345 (1978).
- [26] G. W. Bennett *et al.*, “Improved limit on the muon electric dipole moment”, *Phys. Rev. D* **80**, 052008 (2009).
- [27] G. F. Giudice, P. Paradisi, and M. Passera, “Testing new physics with the electron g-2”, *J. High Energ. Phys.* **11**, 113 (2012).
- [28] B. Abi *et al.* (Muon g-2 Collaboration), “Measurement of the positive muon anomalous magnetic moment to 0.46 ppm”, *Phys. Rev. Lett.* **126**, 141801 (2021).
- [29] K. P. Jungmann, “g-2 of the muon”, *Hyperfine Interact* **210**, 1 (2012).
- [30] D. Hanneke, S. Fogwell, and G. Gabrielse, “New measurement of the electron magnetic moment and the fine structure constant”, *Phys. Rev. Lett.* **100**, 120801 (2008).
- [31] B. Odom, D. Hanneke, B. D’Urso, and G. Gabrielse, “New measurement of the electron magnetic moment using a one-electron quantum cyclotron”, *Phys. Rev. Lett.* **97**, 030801 (2006).
- [32] R. H. Parker, C. Yu, W. Zhong, B. Estey, and H. Müller, “Measurement of the fine-structure constant as a test of the standard model”, *Science* **360**, 191 (2018).
- [33] L. Maiani, “CP violation in purely left-handed weak interactions”, *Phys. Lett. B* **62**, 183 (1976).
- [34] J. Ellis, M. K. Gaillard, and D. V. Nanopoulos, “Left-handed currents and CP violation”, *Nucl. Phys. B.* **109**, 213 (1976).
- [35] B. W. Lee, “Gauge theories of microweak CP violation”, *Phys. Rev. D* **15**, 3394 (1977).



- [36] M. Pospelov and A. Ritz, “Electric dipole moments as probes of new physics”, *Ann. Phys.* **318**, 119 (2005).
- [37] J. Engel, M. J. Ramsey-Musolf, and U. van Kolck, “Electric dipole moments of nucleons, nuclei, and atoms: the standard model and beyond”, *Prog. Part. Nucl. Phys.* **71**, 21 (2013).
- [38] V. Andreev, G. Ang, D. DeMille, J. M. Doyle, G. Gabrielse, J. Haefner, N. R. Hutzler, Z. Lasner, C. Meisenhelder, B. R. O’Leary, C. D. Panda, E. P. West, E. P. West, and X. Wu, “Improved limit on the electric dipole moment of the electron”, *Nature* **562**, 355 (2018).
- [39] N. F. Ramsey, “Electric-dipole moments of elementary particles”, *Rep. Prog. Phys.* **45**, 95 (1982).
- [40] A. D. Sakharov, “Violation of CP Invariance, C asymmetry, and baryon asymmetry of the Universe”, *JETP Lett.* **5**, 24 (1967).
- [41] O. Bertolami, D. Colladay, V. Alan Kostelecký, and R. Potting, “CPT violation and baryogenesis”, *Phys. Lett. B* **395**, 178 (1997).
- [42] V. A. Kostelecký and R. Potting, “CPT and strings”, *Nucl. Phys. B* **359**, 545 (1991).
- [43] C. Gemmel, W. Heil, S. Karpuk, K. Lenz, Y. Sobolev, K. Tullney, M. Burghoff, W. Kilian, S. Knappe-Grüneberg, W. Müller, A. Schnabel, F. Seifert, L. Trahms, and U. Schmidt, “Limit on lorentz and CPT violation of the bound neutron using a free precession  $^3\text{He}/^{129}\text{Xe}$  comagnetometer”, *Phys. Rev. D* **82**, 111901 (2010).
- [44] F. Allmendinger, W. Heil, S. Karpuk, W. Kilian, A. Scharth, U. Schmidt, A. Schnabel, Y. Sobolev, and K. Tullney, “New limit on lorentz-invariance and CPT-violating neutron spin interactions using a free-spin-precession  $^3\text{He}$ - $^{129}\text{Xe}$  comagnetometer”, *Phys. Rev. Lett.* **112**, 110801 (2014).
- [45] A. Sytma, J. E. van den Berg, O. Böll, D. Chernowitz, E. A. Dijk, J. O. Grasdijk, S. Hoekstra, K. Jungmann, S. C. Mathavan, C. Meinema, A. Mohanty, S. E. Müller, J. P. Noordmans, M. Nuñez Portela, C. J. G. Onderwater, C. Pijpker, R. G. E. Timmermans, K. K. Vos, L. Willmann, and H. W. Wilschut, “Test of lorentz invariance in  $\beta$  decay of polarized  $^{20}\text{Na}$ ”, *Phys. Rev. C* **94**, 025503 (2016).
- [46] C.-P. Liu and R. G. E. Timmermans, “P- and T-odd two-nucleon interaction and the deuteron electric dipole moment”, *Phys. Rev. C* **70**, 055501 (2004).
- [47] A. Placci, E. Polacco, E. Zavattini, K. Ziock, G. Carboni, U. Gastaldi, G. Gorini, G. Neri, and G. Torelli, “Observation of muonic X-rays in helium gas and measurement of the two-photon decay rate of the 2s metastable state”, *Nuov. Cim. A* **1**, 445 (1971).
- [48] V. W. Hughes and C. S. Wu, *Muon physics I* (Academic Press, New York, 1977).
- [49] D. T. Wilkinson and H. R. Crane, “Precision measurement of the g factor of the free electron”, *Phys. Rev.* **130**, 852 (1963).
- [50] D. F. Nelson, A. A. Schupp, R. W. Pidd, and H. R. Crane, “Search for an electric dipole moment of the electron”, *Phys. Rev. Lett.* **2**, 492 (1959).

- [51] T. E. Chupp, P. Fierlinger, M. J. Ramsey-Musolf, and J. T. Singh, “Electric dipole moments of atoms, molecules, nuclei, and particles”, *Rev. Mod. Phys.* **91**, 015001 (2019).
- [52] L. I. Schiff, “Measurability of nuclear electric dipole moments”, *Phys. Rev.* **132**, 2194 (1963).
- [53] P. G. H. Sandars, “Electric dipole moments of charged particles”, *Contemp Phys* **42**, 97 (2001).
- [54] P. G. H. Sandars, “The electric dipole moment of an atom”, *Phys. Lett.* **14**, 194 (1965).
- [55] P. G. H. Sandars and E. Lipworth, “Electric dipole moment of the cesium atom. a new upper limit to the electric dipole moment of the free electron”, *Phys. Rev. Lett.* **13**, 718 (1964).
- [56] T. S. Stein, J. P. Carrico, E. Lipworth, and M. C. Weisskopf, “Electric dipole moment of the cesium atom. a new upper limit to the electric dipole moment of the free electron”, *Phys. Rev. Lett.* **19**, 741 (1967).
- [57] M. C. Weisskopf, J. P. Carrico, H. Gould, E. Lipworth, and T. S. Stein, “Electric dipole moment of the cesium atom. A new upper limit to the electric dipole moment of the electron”, *Phys. Rev. Lett.* **21**, 1645 (1968).
- [58] S. A. Murthy, D. Krause, Z. L. Li, and L. R. Hunter, “New limits on the electron electric dipole moment from cesium”, *Phys. Rev. Lett.* **63**, 965 (1989).
- [59] K. Abdullah, C. Carlberg, E. D. Commins, H. Gould, and S. B. Ross, “New experimental limit on the electron electric dipole moment”, *Phys. Rev. Lett.* **65**, 2347 (1990).
- [60] E. D. Commins, S. B. Ross, D. DeMille, and B. C. Regan, “Improved experimental limit on the electric dipole moment of the electron”, *Phys. Rev. A* **50**, 2960 (1994).
- [61] B. C. Regan, E. D. Commins, C. J. Schmidt, and D. DeMille, “New limit on the electron electric dipole moment”, *Phys. Rev. Lett.* **88**, 071805 (2002).
- [62] V. A. Dzuba and V. V. Flambaum, “Calculation of the  $(T, P)$ -odd electric dipole moment of thallium and cesium”, *Phys. Rev. A* **80**, 062509 (2009).
- [63] P. G. H. Sandars, “Measurability of the proton electric dipole moment”, *Phys. Rev. Lett.* **19**, 1396 (1967).
- [64] L. V. Skripnikov, “Combined 4-component and relativistic pseudopotential study of ThO for the electron electric dipole moment search”, *J. Chem. Phys.* **145**, 214301 (2016).
- [65] S. K. Lamoreaux and R. Golub, “Experimental searches for the neutron electric dipole moment”, *J. Phys. G: Nucl. Part. Phys.* **36**, 104002 (2009).
- [66] S. Eckel, P. Hamilton, E. Kirilov, H. W. Smith, and D. DeMille, “Search for the electron electric dipole moment using  $\Omega$ -doublet levels in PbO”, *Phys. Rev. A* **87**, 052130 (2013).

- [67] E. E. Salpeter, “Some atomic effects of an electronic electric dipole moment”, *Phys. Rev.* **112**, 1642 (1958).
- [68] J. Goldemberg and Y. Torizuka, “Upper limit of the electric dipole moment of the electron”, *Phys. Rev.* **129**, 2580 (1963).
- [69] J. P. Carrico, E. Lipworth, P. G. H. Sandars, T. S. Stein, and M. C. Weisskopf, “Electric dipole moments of alkali atoms. A limit to the electric dipole moment of the free electron”, *Phys. Rev.* **174**, 125 (1968).
- [70] H. Gould, “Search for an electric dipole moment in thallium”, *Phys. Rev. Lett.* **24**, 1091 (1970).
- [71] M. A. Player and P. G. H. Sandars, “An experiment to search for an electric dipole moment in the  $^3P_2$  metastable state of xenon”, *J. Phys. B: At. Mol. Phys.* **3**, 1620 (1970).
- [72] N. Sachdeva, I. Fan, E. Babcock, M. Burghoff, T. E. Chupp, S. Degenkolb, P. Fierlinger, S. Haude, E. Kraegleloh, W. Kilian, S. Knappe-Grüneberg, F. Kuchler, T. Liu, M. Marino, J. Meinel, K. Rolfs, Z. Salhi, A. Schnabel, J. T. Singh, S. Stuber, W. A. Terrano, L. Trahms, and J. Voigt, “New limit on the permanent electric dipole moment of  $^{129}\text{Xe}$  using  $^3\text{He}$  comagnetometry and squid detection”, *Phys. Rev. Lett.* **123**, 143003 (2019).
- [73] S. K. Lamoreaux, J. P. Jacobs, B. R. Heckel, F. J. Raab, and N. Fortson, “New constraints on time-reversal asymmetry from a search for a permanent electric dipole moment of  $^{199}\text{Hg}$ ”, *Phys. Rev. Lett.* **59**, 2275 (1987).
- [74] J. P. Jacobs, W. M. Klipstein, S. K. Lamoreaux, B. R. Heckel, and E. N. Fortson, “Testing time-reversal symmetry using  $^{199}\text{Hg}$ ”, *Phys. Rev. Lett.* **71**, 3782 (1993).
- [75] J. P. Jacobs, W. M. Klipstein, S. K. Lamoreaux, B. R. Heckel, and E. N. Fortson, “Limit on the electric-dipole moment of  $^{199}\text{Hg}$  using synchronous optical pumping”, *Phys. Rev. A* **52**, 3521 (1995).
- [76] M. V. Romalis, W. C. Griffith, J. P. Jacobs, and E. N. Fortson, “New limit on the permanent electric dipole moment of  $^{199}\text{Hg}$ ”, *Phys. Rev. Lett.* **86**, 2505 (2001).
- [77] W. C. Griffith, M. D. Swallows, T. H. Loftus, M. V. Romalis, B. R. Heckel, and E. N. Fortson, “Improved limit on the permanent electric dipole moment of  $^{199}\text{Hg}$ ”, *Phys. Rev. Lett.* **102**, 101601 (2009).
- [78] B. Graner, Y. Chen, E. G. Lindahl, and B. R. Heckel, “Reduced limit on the permanent electric dipole moment of  $^{199}\text{Hg}$ ”, *Phys. Rev. Lett.* **116**, 161601 (2016).
- [79] B. Graner, Y. Chen, E. G. Lindahl, and B. R. Heckel, “Erratum: reduced limit on the permanent electric dipole moment of  $^{199}\text{Hg}$  [Phys. Rev. Lett. 116, 161601 (2016)]”, *Phys. Rev. Lett.* **119**, 119901 (2017).
- [80] D. Cho, K. Sangster, and E. A. Hinds, “Tenfold improvement of limits on T violation in thallium fluoride”, *Phys. Rev. Lett.* **63**, 2559 (1989).
- [81] J. J. Hudson, B. E. Sauer, M. R. Tarbutt, and E. A. Hinds, “Measurement of the electron electric dipole moment using YbF molecules”, *Phys. Rev. Lett.* **89**, 023003 (2002).

- [82] J. J. Hudson, D. M. Kara, I. J. Smallman, B. E. Sauer, M. R. Tarbutt, and E. A. Hinds, “Improved measurement of the shape of the electron”, *Nature* **473**, 493 (2011).
- [83] S. Eckel, A. O. Sushkov, and S. K. Lamoreaux, “Limit on the electron electric dipole moment using paramagnetic ferroelectric  $\text{Eu}_{0.5}\text{Ba}_{0.5}\text{TiO}_3$ ”, *Phys. Rev. Lett.* **109**, 193003 (2012).
- [84] W. B. Cairncross, D. N. Gresh, M. Grau, K. C. Cossel, T. S. Roussy, Y. Ni, Y. Zhou, J. Ye, and E. A. Cornell, “Precision measurement of the electron’s electric dipole moment using trapped molecular ions”, *Phys. Rev. Lett.* **119**, 153001 (2017).
- [85] J. Baron, W. C. Campbell, D. DeMille, J. M. Doyle, G. Gabrielse, Y. V. Gurevich, P. W. Hess, N. R. Hutzler, E. Kirilov, I. Kozyryev, B. R. O’Leary, C. D. Panda, M. F. Parsons, E. S. Petrik, B. Spaun, A. C. Vutha, and A. D. West, “Order of magnitude smaller limit on the electric dipole moment of the electron”, *Science* **343**, 269 (2014).
- [86] B. V. Vasil’Ev and E. V. Kolycheva, “Measurement of the electric dipole moment of the electron with a quantum interferometer”, *Sov. Phys. JETP* **47**, 243 (1978).
- [87] B. J. Heidenreich, O. T. Elliott, N. D. Charney, K. A. Virgien, A. W. Bridges, M. A. McKeon, S. K. Peck, D. Krause, J. E. Gordon, L. R. Hunter, and S. K. Lamoreaux, “Limit on the electron electric dipole moment in gadolinium-iron garnet”, *Phys. Rev. Lett.* **95**, 253004 (2005).
- [88] Y. J. Lim, C.-Y. Liu, S. K. Lamoreaux, and G. Reddy, “Experimental search for the electron electric dipole moment using solid state techniques”, *J. Phys.: Conf. Ser.* **312**, 102009 (2011).
- [89] A. collaboration, “Improved limit on the electric dipole moment of the electron”, *Nature* **562**, 355 (2018).
- [90] P. Aggarwal, H. L. Bethlem, A. Borschevsky, M. Denis, K. Esajas, P. A. B. Haase, Y. Hao, S. Hoekstra, K. Jungmann, T. B. Meijknecht, M. C. Mooij, R. G. E. Timmermans, W. Ubachs, L. Willmann, and A. Zapara, “Measuring the electric dipole moment of the electron in BaF”, *Eur. Phys. J. D* **72**, 197 (2018).
- [91] J. Lim, J. R. Almond, M. A. Trigatzis, J. A. Devlin, N. J. Fitch, B. E. Sauer, M. R. Tarbutt, and E. A. Hinds, “Laser cooled YbF molecules for measuring the electron’s electric dipole moment”, *Phys. Rev. Lett.* **120**, 123201 (2018).
- [92] N. R. Hutzler, H. I. Lu, and J. M. Doyle, “The buffer gas source: an intense, cold, and slow source for atoms and molecules”, *Chem. Rev.* **112**, 4803 (2012).
- [93] A. Kantrowitz and J. Grey, “A high intensity source for the molecular beam. Part I. Theoretical”, *Rev. Sci. Instrum.* **22**, 328 (1951).
- [94] G. Scoles, *Atomic and molecular beam methods* (Oxford University Press, New York-Oxford, 1988).
- [95] J. Wang, V. A. Shamamian, B. R. Thomas, J. M. Wilkinson, J. Riley, C. F. Giese, and W. R. Gentry, “Speed ratios greater than 1000 and temperatures less than 1 mK in a pulsed He beam”, *Phys. Rev. Lett.* **60**, 696 (1988).
- [96] U. Even, “Pulsed supersonic beams from high pressure source: simulation results and experimental measurements”, *Adv. Chem.* **2014**, 636042 (2014).

- [97] B. Yan, P. F. H. Claus, B. G. M. van Oorschot, L. Gerritsen, and A. T. J. B. Eppink, “A new high intensity and short-pulse molecular beam valve”, *Rev. Sci. Instrum.* **84**, 023102 (2013).
- [98] M. R. Tarbutt, J. J. Hudson, B. E. Sauer, E. A. Hinds, V. A. Ryzhov, V. L. Ryabov, and V. F. Ezhov, “A jet beam source of cold YbF radicals”, *J. Phys. B: At. Mol. Opt. Phys.* **35**, 5013 (2002).
- [99] H. Loh, J. Wang, M. Grau, T. S. Yahn, R. W. Field, C. H. Greene, and E. A. Cornell, “Laser-induced fluorescence studies of  $\text{HfF}^+$  produced by autoionization”, *J. Chem. Phys.* **135**, 154308 (2011).
- [100] D. Patterson, J. Rasmussen, and J. M. Doyle, “Intense atomic and molecular beams via neon buffer-gas cooling”, *New J. Phys.* **11**, 055018 (2009).
- [101] N. R. Hutzler, M. F. Parsons, Y. V. Gurevich, P. W. Hess, E. Petrik, B. Spaun, A. C. Vutha, D. DeMille, G. Gabrielse, and J. M. Doyle, “A cryogenic beam of refractory, chemically reactive molecules with expansion cooling”, *Phys. Chem. Chem. Phys.* **13**, 18976 (2011).
- [102] A. Jadbabaie, N. H. Pilgram, J. Klos, S. Kotochigova, and N. R. Hutzler, “Enhanced molecular yield from a cryogenic buffer gas beam source via excited state chemistry”, *New J. Phys.* **22**, 022002 (2020).
- [103] L. Baum, N. B. Vilas, C. Hallas, B. L. Augenbraun, S. Raval, D. Mitra, and J. M. Doyle, “1D magneto-optical trap of polyatomic molecules”, *Phys. Rev. Lett.* **124**, 133201 (2020).
- [104] I. Kozyryev and N. R. Hutzler, “Precision measurement of time-reversal symmetry violation with laser-cooled polyatomic molecules”, *Phys. Rev. Lett.* **119**, 133002 (2017).
- [105] H. L. Bethlem, G. Berden, and G. Meijer, “Decelerating neutral dipolar molecules”, *Phys. Rev. Lett.* **83**, 1558 (1999).
- [106] H. L. Bethlem, G. Berden, F. M. H. Crompvoets, R. T. Jongma, A. J. A. van Roij, and G. Meijer, “Electrostatic trapping of ammonia molecules”, *Nature* **406**, 491 (2000).
- [107] E. R. Hudson, J. R. Bochinski, H. J. Lewandowski, B. C. Sawyer, and J. Ye, “Efficient stark deceleration of cold polar molecules”, *Eur. Phys. J. D* **31**, 351 (2004).
- [108] E. R. Hudson, C. Ticknor, B. C. Sawyer, C. A. Taatjes, H. J. Lewandowski, J. R. Bochinski, J. L. Bohn, and J. Ye, “Production of cold formaldehyde molecules for study and control of chemical reaction dynamics with hydroxyl radicals”, *Phys. Rev. A* **73**, 063404 (2006).
- [109] S. Y. T. van de Meerakker, I. Labazan, S. Hoesktra, J. Küpper, and G. Meijer, “Production and deceleration of a pulsed beam of metastable  $\text{NH}$  ( $a^1\Delta$ ) radicals”, *J. Phys. B: At. Mol. Opt. Phys.* **39**, S1077 (2006).
- [110] S. Jung, E. Tiemann, and C. Lisdat, “Cold atoms and molecules from fragmentation of decelerated  $\text{SO}_2$ ”, *Phys. Rev. A* **74**, 040701 (2006).

- [111] S. Hoekstra, J. J. Gilijamse, B. Sartakov, N. Vanhaecke, L. Scharfenberg, S. Y. T. van de Meerakker, and G. Meijer, “Optical pumping of trapped neutral molecules by blackbody radiation”, *Phys. Rev. Lett.* **98**, 133001 (2007).
- [112] S. K. Tokunaga, J. M. Dyne, E. A. Hinds, and M. R. Tarbutt, “Stark deceleration of lithium hydride molecules”, *New J. Phys.* **11**, 055038 (2009).
- [113] T. E. Wall, J. F. Kanem, J. M. Dyne, J. J. Hudson, B. E. Sauer, E. A. Hinds, and M. R. Tarbutt, “Stark deceleration of CaF molecules in strong- and weak-field seeking states”, *Phys. Chem. Chem. Phys.* **13**, 18991 (2011).
- [114] S. Y. T. van de Meerakker, H. L. Bethlem, and G. Meijer, “Taming molecular beams”, *Nature Physics* **4**, 595 (2008).
- [115] S. Y. T. van de Meerakker, H. L. Bethlem, N. Vanhaecke, and G. Meijer, “Manipulation and control of molecular beams”, *Chem. Rev.* **112**, 4828 (2012).
- [116] S. Y. T. van de Meerakker, N. Vanhaecke, H. L. Bethlem, and G. Meijer, “Transverse stability in a stark decelerator”, *Phys. Rev. A* **73**, 023401 (2006).
- [117] E. Narevicius, A. Libson, C. G. Parthey, I. Chavez, J. Narevicius, U. Even, and M. G. Raizen, “Stopping supersonic oxygen with a series of pulsed electromagnetic coils: a molecular coilgun”, *Phys. Rev. A* **77**, 051401 (2008).
- [118] T. Momose, Y. Liu, S. Zhou, P. Djuricanin, and D. Carty, “Manipulation of translational motion of methyl radicals by pulsed magnetic fields”, *Phys. Chem. Chem. Phys.* **15**, 1772 (2013).
- [119] M. Motsch, P. Jansen, J. A. Agner, H. Schmutz, and F. Merkt, “Slow and velocity-tunable beams of metastable He<sub>2</sub> by multistage zeeman deceleration”, *Phys. Rev. A* **89**, 043420 (2014).
- [120] A. Osterwalder, S. A. Meek, G. Hammer, H. Haak, and G. Meijer, “Deceleration of neutral molecules in macroscopic traveling traps”, *Phys. Rev. A* **81**, 051401 (2010).
- [121] M. Quintero-Pérez, P. Jansen, T. E. Wall, J. E. van den Berg, S. Hoekstra, and H. L. Bethlem, “Static trapping of polar molecules in a traveling wave decelerator”, *Phys. Rev. Lett.* **110**, 133003 (2013).
- [122] C. Cheng, A. P. P. van der Poel, P. Jansen, M. Quintero-Pérez, T. E. Wall, W. Ubachs, and H. L. Bethlem, “Molecular fountain”, *Phys. Rev. Lett.* **117**, 253201 (2016).
- [123] S. C. Mathavan, A. Zapara, Q. Esajas, and S. Hoekstra, “Deceleration of a supersonic beam of SrF molecules to 120 ms<sup>-1</sup>”, *ChemPhysChem* **17**, 3709 (2016).
- [124] L. Scharfenberg, J. Klos, P. J. Dagdigan, M. H. Alexander, G. Meijer, and S. Y. T. van der Meerakker, “State-to-state inelastic scattering of stark-decelerated OH radicals with Ar atoms”, *Phys. Chem. Chem. Phys.* **12**, 10660 (2010).
- [125] W. D. Phillips and H. Metcalf, “Laser deceleration of an atomic beam”, *Phys. Rev. Lett.* **48**, 596 (1982).
- [126] E. S. Shuman, J. F. Barry, and D. DeMille, “Laser cooling of a diatomic molecule”, *Nature* **467**, 820 (2010).

- [127] J. F. Barry, E. S. Shuman, E. B. Norrgard, and D. DeMille, “Laser radiation pressure slowing of a molecular beam”, *Phys. Rev. Lett.* **108**, 103002 (2012).
- [128] M. T. Hummon, M. Yeo, B. K. Stuhl, A. L. Collopy, Y. Xia, and J. Ye, “2D magneto-optical trapping of diatomic molecules”, *Phys. Rev. Lett.* **110**, 143001 (2013).
- [129] V. Zhelyazkova, A. Cournol, T. E. Wall, A. Matsushima, J. J. Hudson, E. A. Hinds, M. R. Tarbutt, and B. E. Sauer, “Laser cooling and slowing of CaF molecules”, *Phys. Rev. A* **89**, 053416 (2014).
- [130] B. Hemmerling, E. Chae, A. Ravi, L. Anderegg, G. K. Drayna, N. R. Hutzler, A. L. Collopy, J. Ye, W. Ketterle, and J. M. Doyle, “Laser slowing of CaF molecules to near the capture velocity of a molecular MOT”, *J. Phys. B: At. Mol. Opt. Phys.* **49**, 174001 (2016).
- [131] R. L. McNally, I. Kozyryev, S. Vazquez-Carson, K. Wenz, T. Wang, and T. Zelevinsky, “Optical cycling, radiative deflection and laser cooling of barium monohydride ( $^{138}\text{Ba}^1\text{H}$ )”, *New J. Phys.* **22**, 083047 (2020).
- [132] C. J. Foot, *Atomic physics* (Oxford University Press, 2005).
- [133] J. F. Barry, D. J. McCarron, E. B. Norrgard, M. H. Steinecker, and D. DeMille, “Magneto-optical trapping of a diatomic molecule”, *Nature* **512**, 286 (2014).
- [134] D. J. McCarron, E. B. Norrgard, M. H. Steinecker, and D. DeMille, “Improved magneto-optical trapping of a diatomic molecule”, *New J. Phys.* **17**, 035014 (2015).
- [135] L. Anderegg, B. L. Augenbraun, E. Chae, B. Hemmerling, N. R. Hutzler, A. Ravi, A. Collopy, J. Ye, W. Ketterle, and J. M. Doyle, “Radio frequency magneto-optical trapping of CaF with high density”, *Phys. Rev. Lett.* **119**, 103201 (2017).
- [136] H. J. Williams, S. Truppe, M. Hambach, L. Caldwell, N. J. Fitch, E. A. Hinds, B. E. Sauer, and M. R. Tarbutt, “Characteristics of a magneto-optical trap of molecules”, *New J. Phys.* **19**, 113035 (2017).
- [137] A. L. Collopy, S. Ding, Y. Wu, I. A. Finneran, L. Anderegg, B. L. Augenbraun, J. M. Doyle, and J. Ye, “3D magneto-optical trap of yttrium monoxide”, *Phys. Rev. Lett.* **121**, 213201 (2018).
- [138] W. Gerlach and O. Stern, “Der experimentelle nachweis der richtungsquantelung in magnetfeld”, *Zeitschrift für Physik* **9**, 349 (1922).
- [139] W. Gerlach and O. Stern, “Über die richtungsquantelung im magnetfeld”, *Annalen der Physik* **379**, 673 (1924).
- [140] H. J. Metcalf and P. van der Straten, *Laser cooling and trapping* (Springer, 1999).
- [141] J. D. Weinstein, R. DeCarvalho, T. Guillet, B. Friedrich, and J. M. Doyle, “Magnetic trapping of calcium monohydride molecules at millikelvin temperatures”, *Nature* **395**, 148 (1998).
- [142] B. C. Sawyer, B. L. Lev, E. R. Hudson, B. K. Stuhl, M. Lara, J. L. Bohn, and J. Ye, “Magnetoelectrostatic trapping of ground state OH molecules”, *Phys. Rev. Lett.* **98**, 253002 (2007).

- [143] E. Tsikata, W. C. Campbell, M. T. Hummon, H.-I. Lu, and J. M. Doyle, “Magnetic trapping of NH molecules with 20 s lifetimes”, *New J. Phys.* **12**, 065028 (2010).
- [144] H.-I Lu, I. Kozyryev, B. Hemmerling, J. Piskorski, and J. M. Doyle, “Magnetic trapping of molecules via optical loading and magnetic slowing”, *Phys. Rev. Lett.* **112**, 113006 (2014).
- [145] D. J. McCarron, M. H. Steinecker, Y. Zhu, and D. DeMille, “Magnetic trapping of an ultracold gas of polar molecules”, *Phys. Rev. Lett.* **121**, 013202 (2018).
- [146] H. J. Williams, L. Caldwell, N. J. Fitch, S. Truppe, J. Rodewald, E. A. Hinds, B. E. Sauer, and M. R. Tarbutt, “Magnetic trapping and coherent control of laser-cooled molecules”, *Phys. Rev. Lett.* **120**, 163201 (2018).
- [147] L. Anderegg, B. L. Augenbraun, Y. Bao, S. Burchesky, L. W. Cheuk, W. Ketterle, and J. M. Doyle, “Laser cooling of optically trapped molecules”, *Nature Physics* **14**, 890 (2018).
- [148] W. H. Wing, “Electrostatic trapping of neutral atomic particles”, *Phys. Rev. Lett.* **45**, 631 (1980).
- [149] J. Kleinert, C. Haimberger, P. J. Zabawa, and N. P. Bigelow, “Trapping of ultracold polar molecules with a thin-wire electrostatic trap”, *Phys. Rev. Lett.* **99**, 143002 (2007).
- [150] S. D. Hogan, C. Seiler, and F. Merkt, “Rydberg-state-enabled deceleration and trapping of cold molecules”, *Phys. Rev. Lett.* **103**, 123001 (2009).
- [151] B. G. U. Englert, M. Mielenz, C. Sommer, J. Bayerl, M. Motsch, P. W. H. Pinkse, G. Rempe, and M. Zeppenfeld, “Storage and adiabatic cooling of polar molecules in a microstructured trap”, *Phys. Rev. Lett.* **107**, 263003 (2011).
- [152] F. H. Crawford, “Zeeman effect in diatomic molecular spectra”, *Rev. Mod. Phys.* **6**, 90 (1934).
- [153] E. P. West, “A thermochemical cryogenic buffer gas beam source of ThO for measuring the electric dipole moment of the electron”, PhD thesis (Harvard University, 2017).
- [154] W. B. Cairncross, “Searching for time-reversal symmetry violation with molecular ions: quantum state control and photofragment imaging”, PhD thesis (University of Colorado, Boulder, 2019).
- [155] L. V. Skripnikov, A. N. Petrov, and A. V. Titov, “Communication: theoretical study of ThO for the electron electric dipole moment search”, *J. Chem. Phys.* **139**, 221103 (2013).
- [156] A. N. Petrov, N. S. Mosyagin, T. A. Isaev, and A. V. Titov, “Theoretical study of  $\text{HfF}^+$  in search of the electron electric dipole moment”, *Phys. Rev. A* **76**, 030501 (2007).
- [157] M. G. Kozlov, “Enhancement of the electric dipole moment of the electron in the YbF molecule”, *J. Phys. B: At. Mol. Opt. Phys.* **30**, L607 (1997).
- [158] E. R. Meyer and J. L. Bohn, “Prospects for an electron electric-dipole moment search in metastable ThO and  $\text{ThF}^+$ ”, *Phys. Rev. A* **78**, 010502 (2008).



- [159] K. Gaul and R. Berger, “Zeroth order regular approximation approach to electric dipole moment interactions of the electron”, *J. Chem. Phys.* **147**, 014109 (2017).
- [160] L. V. Skripnikov and A. V. Titov, “Theoretical study of  $\text{ThF}^+$  in the search for  $T$ ,  $P$ -violation effects: effective state of a Th atom in  $\text{ThF}^+$  and  $\text{ThO}$  compounds”, *Phys. Rev. A* **91**, 042504 (2015).
- [161] C. J. Ho, J. A. Devlin, I. M. Rabey, P. Yzombard, S. C. Wright, N. J. Fitch, E. A. Hinds, M. R. Tarbutt, and B. E. Sauer, “New techniques for a measurement of the electron’s electric dipole moment”, *New J. Phys.* **22**, 053031 (2020).
- [162] N. J. Fitch, J. Lim, E. A. Hinds, B. E. Sauer, and M. R. Tarbutt, “Methods for measuring the electron’s electric dipole moment using ultracold  $\text{YbF}$  molecules”, *Arxiv* **2009.00346** (2020).
- [163] S. Truppe, M. Hambach, S. M. Skoff, N. E. Bulleid, J. S. Bumby, R. J. Hendricks, E. A. Hinds, B. E. Sauer, and M. R. Tarbutt, “A buffer gas beam source for short, intense and slow molecular pulses”, *J. Mod. Opt.* **65**, 648 (2017).
- [164] M. I. Fabrikant, T. Li, N. J. Fitch, N. Farrow, J. D. Weinstein, and H. J. Lewandowski, “Method for traveling-wave deceleration of buffer-gas beams of  $\text{CH}$ ”, *Phys. Rev. A* **90**, 033418 (2014).
- [165] Y. Hao, L. F. Pašteka, L. Visscher, P. Aggarwal, H. L. Bethlem, A. Boeschoten, A. Borschevsky, M. Denis, K. Esajas, S. Hoekstra, K. Jungmann, V. R. Marshall, T. B. Meijknecht, M. C. Mooij, R. G. E. Timmermans, A. Touwen, W. Ubachs, L. Willmann, Y. Yin, and A. Zapara, “High accuracy theoretical investigations of  $\text{CaF}$ ,  $\text{SrF}$ , and  $\text{BaF}$  and implications for laser-cooling”, *J. Chem. Phys.* **151**, 034302 (2019).
- [166] B. H. Bransden and C. J. Joachain, *Physics of atoms and molecules* (Prentice Hall, 2003).
- [167] J. M. Brown and A. Carrington, *Rotational spectroscopy of diatomic molecules* (Cambridge Univ. Press, 2003).
- [168] F. Hund, “Zur deutung einiger erscheinungen in den molekelspektren”, *Zeitschrift für Physik* **36**, 657 (1926).
- [169] F. Hund, “Zur deutung der molekelspektren. I”, *Zeitschrift für Physik* **40**, 742 (1927).
- [170] R. A. Frosch and H. M. Foley, “Magnetic hyperfine structure in diatomic molecules”, *Phys. Rev.* **88**, 1337 (1952).
- [171] K. P. Huber and G. Herzberg, *Molecular spectra and molecular structure: constants of diatomic molecules* (Springer US, 1979).
- [172] J. M. Brown and A. J. Merer, “Lambda-type doubling parameters for molecules in  $\Pi$  electronic states of triplet and higher multiplicity”, *J. Mol. Spec.* **74**, 488 (1979).
- [173] R. S. Mulliken and A. Christy, “ $\Lambda$ -type doubling and electron configurations in diatomic molecules”, *Phys. Rev.* **38**, 87 (1931).
- [174] P. M. Sheridan, J.-G. Wang, M. J. Dick, and P. F. Bernath, “Optical-optical double resonance spectroscopy of the  $\text{C}^2\Pi\text{-A}^2\Pi$  and  $\text{D}^2\Sigma^+\text{-A}^2\Pi$  transitions of  $\text{SrF}$ ”, *J. Phys. Chem. A* **113**, 13383 (2009).

- [175] P. Colarusso, B. Guo, K. Q. Zhang, and P. F. Bernath, “High resolution infrared emission spectrum of strontium monofluoride”, *J. Mol. Spectrosc.* **175**, 158 (1996).
- [176] T. C. Steimle, P. J. Domaille, and D. O. Harris, “Rotational analysis of the  $A^2\Pi$ - $X^2\Sigma$  system of SrF using a CW tunable dye laser”, *J. Mol. Spectrosc.* **73**, 441 (1978).
- [177] T. C. Steimle, D. A. Fletcher, and C. T. Scurlock, “A molecular beam study of the (0, 0)  $A^2\Pi$ - $X^2\Sigma$  band system of SrF”, *J. Mol. Spectrosc.* **158**, 487 (1993).
- [178] W. J. Childs, L. S. Goodman, and I. Renhorn, “Radio-frequency optical double-resonance spectrum of SrF: the  $X^2\Sigma^+$  state”, *J. Mol. Spectrosc.* **87**, 522 (1981).
- [179] A. Bernard, C. Effantin, E. Andrianavalona, J. Vergès, and R. F. Barrow, “Laser-induced fluorescence of BaF: further results for six electronic states”, *J. Mol. Spectrosc.* **152**, 174 (1992).
- [180] C. Effantin, A. Bernard, J. d’Incan, G. Wannous, J. Vergès, and R. Barrow, “Studies of the electronic states of the BaF molecule”, *Mol. Phys.* **70**, 735 (1990).
- [181] W. E. Ernst, J. Kändler, and T. Törring, “Hyperfine structure and electric dipole moment of BaF  $X^2\Sigma^+$ ”, *J. Chem. Phys.* **84**, 4769 (1986).
- [182] W. Ernst, J. Kändler, S. Kindt, and T. Törring, “Electric dipole moment of SrF  $X^2\Sigma^+$  from high-precision stark effect measurements”, *Chem. Phys. Lett.* **113**, 351 (1985).
- [183] C. Ryzlewicz, H. U. Schütze-Pahlmann, J. Hoeft, and T. Törring, “Rotational spectrum and hyperfine structure of  $^2\Sigma$  radicals BaF and BaCl”, *Chem. Phys.* **71**, 389 (1982).
- [184] R. Campargue, *Atomic and molecular beams: the state of the art 2000* (Springer-Verlag Berlin Heidelberg, 2001).
- [185] R. E. Smalley, L. Wharton, and D. H. Levy, “The fluorescence excitation spectrum of rotationally cooled  $\text{NO}_2$ ”, *J. Chem. Phys.* **63**, 4977 (1975).
- [186] J. Lim, J. R. Almond, M. R. Tarbutt, D. T. Nguyen, and T. C. Steimle, “The [557]- $X^2\Sigma^+$  and [561]- $X^2\Sigma^+$  bands of ytterbium fluoride,  $^{174}\text{YbF}$ ”, *J. Mol. Spec.* **338**, 81 (2017).
- [187] T. C. Steimle, S. Frey, A. Le, D. DeMille, D. A. Rahmlow, and C. Linton, “Molecular-beam optical stark and zeeman study of the  $A^2\Pi$ - $X^2\Sigma^+$  (0,0) band system of BaF”, *Phys. Rev. A* **84**, 012508 (2011).
- [188] M. Costes and C. Naulin, “Observation of quantum dynamical resonances in near cold inelastic collisions of astrophysical molecules”, *Chem. Sci.* **7**, 2462 (2016).
- [189] I. W. M. Smith, “Reactions at very low temperatures: gas kinetics at a new frontier”, *Angew. Chem. Int. Ed.* **45**, 2842 (2006).
- [190] S. N. Vogels, Z. Gao, and S. Y. T van de Meerakker, “Optimal beam sources for stark decelerators in collision experiments: a tutorial review”, *EPJ Techn Instrum* **2**, 12 (2015).
- [191] U. Even, J. Jortner, D. Noy, and N. Lavie, “Cooling of large molecules below 1 K and He clusters formation”, *J. Chem. Phys.* **112**, 8068 (2000).

- [192] A. Cournol, P. Pillet, H. Lignier, and D. Comparat, “Rovibrational optical pumping of a molecular beam”, *Phys. Rev. A* **97**, 031401 (2018).
- [193] T. G. Dietz, M. A. Duncan, D. E. Powers, and R. E. Smalley, “Laser production of supersonic metal cluster beams”, *J. Chem. Phys.* **74**, 6511 (1981).
- [194] D. E. Powers, S. G. Hansen, M. E. Geusic, A. C. Puiiu, J. B. Hopkins, T. G. Dietz, M. A. Duncan, P. R. R. Langridge-Smith, and R. E. Smalley, “Supersonic metal cluster beams: laser photoionization studies of copper cluster  $\text{Cu}_2$ ”, *J. Phys. Chem.* **86**, 2556 (1982).
- [195] J. B. Hopkins, P. R. R. Langridge-Smith, M. D. Morse, and R. E. Smalley, “Supersonic metal cluster beams of refractory metals: spectral investigations of ultracold  $\text{Mo}_2$ ”, *J. Chem. Phys.* **78**, 1627 (1983).
- [196] G. Dorthé, M. Costes, C. Naulin, and J. Joussot-Dubien, “Reactive scattering using pulsed crossed supersonic molecular beams. example of the  $\text{C}+\text{NO}\rightarrow\text{CN}+\text{O}$  and  $\text{C}+\text{N}_2\text{O}\rightarrow\text{CN}+\text{NO}$  reactions”, *Rev. Sci. Instrum.* **83**, 3171 (1985).
- [197] M. Costes, C. Naulin, G. Dorthé, G. Daleua, J. Joussot-Dubien, C. Lalaude, M. Vinckert, A. Destor, C. Vaucamps, and G. Nouchi, “A pulsed crossed supersonic molecular beam apparatus to study the dynamics of refractory atom reactions”, *J. Phys. E: Sci. Instrum.* **22**, 1017 (1989).
- [198] R. I. Kaiser and A. G. Suits, “A high-intensity, pulsed supersonic carbon source with  $\text{C}(^3P_J)$  kinetic energies of 0.08–0.7 eV for crossed beam experiments”, *Rev. Sci. Instrum.* **66**, 5405 (1995).
- [199] A. G. Adam, L. P. Fraser, W. D. Hamilton, and M. C. Steeves, “Gas-phase electronic spectroscopy of cobalt monofluoride”, *Chem. Phys. Lett.* **230**, 82 (1994).
- [200] D. A. Fletcher, K. Y. Jung, C. T. Scurlock, and T. C. Steimle, “Molecular beam pump/probe microwave-optical double resonance using a laser ablation source”, *J. Chem. Phys.* **98**, 1837 (1993).
- [201] A. E. Leanhardt, J. L. Bohn, H. Loh, P. Maletinsky, E. R. Meyer, L. C. Sinclair, R. P. Stutz, and E. A. Cornell, “High-resolution spectroscopy on trapped molecular ions in rotating electric fields: a new approach for measuring the electron electric dipole moment”, *J. Mol. Spec.* **270**, 1 (2011).
- [202] E. Altuntas, J. Ammon, S. B. Cahn, and D. DeMille, “Measuring nuclear-spin-dependent parity violation with molecules: experimental methods and analysis of systematic errors”, *Phys. Rev. A* **97**, 042101 (2018).
- [203] U. Even, “The Even-Lavie valve as a source for high intensity supersonic beam”, *EPJ Techn Instrum* **2**, 17 (2015).
- [204] C. Dong, J. Liu, F. Li, and F. Wang, “Laser ablation atomic beam apparatus with time-sliced velocity map imaging for studying state-to-state metal reaction dynamics”, *Chin. J. Chem. Phys.* **29**, 99 (2016).
- [205] D. Yan, Y. Ma, F. Li, J. Liu, G. Wang, and F. Wang, “Imaging reaction dynamics of  $\text{Y}+\text{SO}_2$ ”, *Chin. J. Chem. Phys.* **33**, 239 (2020).

- [206] N. Akerman, M. Karpov, Y. Segev, N. Bibelnik, J. Narevicius, and E. Narevicius, “Trapping of molecular oxygen together with lithium atoms”, *Phys. Rev. Lett.* **119**, 073204 (2017).
- [207] M. Karpov, M. Pitzer, Y. Segev, J. Narevicius, and E. Narevicius, “Low-energy collisions between carbon atoms and oxygen molecules in a magnetic trap”, *New J. Phys.* **22**, 103055 (2020).
- [208] R. Katzy, M. Singer, S. Izadnia, A. C. LaForge, and C. Stienkemeier, “Doping He droplets by laser ablation with a pulsed supersonic jet source”, *Rev. Sci. Instrum.* **87**, 013105 (2016).
- [209] A. C. Vutha, M. Horbatsch, and E. A. Hessels, “Orientation-dependent hyperfine structure of polar molecules in a rare-gas matrix: a scheme for measuring the electron electric dipole moment”, *Phys. Rev. A* **98**, 032513 (2018).
- [210] J. B. Anderson and J. B. Fenn, “Velocity distributions in molecular beams from nozzle sources”, *Phys. Fluids* **8**, 780 (1965).
- [211] H. Haberland, U. Buck, and M. Tolle, “Velocity distribution of supersonic nozzle beams”, *Rev. Sci. Instrum.* **56**, 1712 (1985).
- [212] F. Reif, *Fundamentals of statistical and thermal physics* (McGraw-Hill, Singapore, 1988).
- [213] A. P. P. van der Poel, P. C. Zieger, S. Y. T. van de Meerakker, J. Loreau, A. van der Avoird, and H. L. Bethlem, “Cold collisions in a molecular synchrotron”, *Phys. Rev. Lett.* **120**, 033402 (2018).
- [214] A. P. P. van der Poel, “Cold collisions in a molecular synchrotron”, Ph.D. thesis (Vrije Universiteit Amsterdam, 2018).
- [215] C. M. Western, “PGOPHER: A program for simulating rotational, vibrational and electronic spectra”, *J. Quant. Spectrosc. Radiat. Transf.* **186**, 221 (2017).
- [216] J. F. Barry, “Laser cooling and slowing of a diatomic molecule”, Ph.D. thesis (Yale University, 2013).
- [217] T. Chen, W. Bu, and B. Yan, “Structure, branching ratios, and a laser-cooling scheme for the  $^{138}\text{BaF}$  molecule”, *Phys. Rev. A* **94**, 063415 (2016).
- [218] S. K. Tokunaga, J. O. Stack, J. J. Hudson, B. E. Sauer, E. A. Hinds, and M. R. Tarbutt, “A supersonic beam of cold lithium hydride molecules”, *J. Chem. Phys.* **126**, 124314 (2007).
- [219] P. C. Waterman and S. A. Stern, “Separation of gas mixtures in a supersonic jet”, *J. Chem. Phys.* **31**, 405 (1959).
- [220] S. Truppe, S. Marx, S. Kray, M. Doppelbauer, S. Hofsäss, H. C. Schewe, N. Walter, J. Pérez-Ríos, B. G. Sartakov, and G. Meijer, “Spectroscopic characterization of aluminum monofluoride with relevance to laser cooling and trapping”, *Phys. Rev. A* **100**, 052513 (2019).
- [221] W. Bu, T. Chen, G. Lv, and B. Yan, “Cold collision and high-resolution spectroscopy of buffer-gas-cooled BaF molecules”, *Phys. Rev. A* **95**, 032701 (2017).

- [222] R. Albrecht, M. Scharwaechter, T. Sixt, L. Hofer, and T. Langen, “Buffer-gas cooling, high-resolution spectroscopy, and optical cycling of barium monofluoride molecules”, *Phys. Rev. A* **101**, 013413 (2020).
- [223] N. R. Hutzler, “A new limit on the electron electric dipole moment: beam production, data interpretation and systematics”, Ph.D. thesis (Harvard University, 2014).
- [224] S. Kang, F. Kuang, G. Jiang, and J. Du, “The suitability of barium monofluoride for laser cooling from ab initio study”, *Mol. Phys.* **114**, 810 (2016).
- [225] S. Tohme and M. Korek, “Theoretical study of the electronic structure with dipole moment calculations of barium monofluoride”, *J. Quant. Spec. Rad. Trans.* **167**, 82 (2015).
- [226] L. Young, W. T. Hill, S. J. Sibener, S. D. Price, C. E. Tanner, C. E. Wieman, and S. R. Leone, “Precision lifetime measurements of Cs  $6p^2P_{1/2}$  and  $6p^2P_{3/2}$  levels by single-photon counting”, *Phys. Rev. A* **50**, 2174 (1994).
- [227] G. Toh, J. A. Jaramillo-Villegas, N. Glotzbach, J. Quirk, I. C. Stevenson, J. Choi, A. M. Weiner, and D. S. Elliott, “Measurement of the lifetime of the  $7s^2S_{1/2}$  state in atomic cesium using asynchronous gated detection”, *Phys. Rev. A* **97**, 052507 (2018).
- [228] M. Safronova, D. Budker, D. DeMille, D. F. J. Kimball, A. Derevianko, and C. W. Clark, “Search for new physics with atoms and molecules”, *Rev. Mod. Phys.* **90**, 025008 (2018).
- [229] L. E. Berg, T. Olsson, J. C. Chanteloup, A. Hishikawa, and P. Royen, “Lifetime measurements of excited molecular states using a Ti: sapphire laser: radiative lifetimes of the  $A^2\Pi$ ,  $B^2\Sigma^+$  and  $C^2\Pi$  states of BaF”, *Mol. Phys.* **79**, 721 (1992).
- [230] L. E. Berg, N. Gador, D. Husain, H. Ludwigs, and P. Royen, “Lifetime measurements of the  $A^2\Pi_{1/2}$  state of BaF using laser spectroscopy”, *Chem. Phys. Lett.* **287**, 89 (1998).
- [231] P. J. Dagdigian, H. W. Cruse, and R. N. Zare, “Radiative lifetimes of the alkaline earth monohalides”, *J. Chem. Phys.* **60**, 2330 (1974).
- [232] L. Xu, B. Wei, Y. Xia, L. Deng, and J. Yin, “BaF radical: a promising candidate for laser cooling and magneto-optical trapping”, *Chin. Phys. B* **26**, 033702 (2017).
- [233] H. C. Burstyn, “Afterpulsing effects in photon correlation experiments”, *Rev. Sci. Instrum.* **51**, 1431 (1980).
- [234] M. Zhao, L. Jin, B. Chen, Y. Ding, H. Ma, and D. Chen, “Afterpulsing and its correction in fluorescence correlation spectroscopy experiments”, *Appl. Opt.* **42**, 4031 (2003).
- [235] K. Ishii and T. Tahara, “Correction of the afterpulsing effect in fluorescence correlation spectroscopy using time symmetry analysis”, *Opt. Express* **23**, 32387 (2015).
- [236] M. Iliaš and T. Saue, “An infinite-order two-component relativistic hamiltonian by a simple one-step transformation”, *J. Chem. Phys.* **126**, 064102 (2007).
- [237] T. Saue, “Relativistic hamiltonians for chemistry: a primer”, *ChemPhysChem* **12**, 3077 (2011).

- [238] U. Kaldor and E. Eliav, “High-accuracy calculations for heavy and super-heavy elements”, *Adv. Quantum Chem.* **31**, 313 (1998).
- [239] J. L. Bohn, A. M. Rey, and J. Ye, “Cold molecules: progress in quantum engineering of chemistry and quantum matter”, *Science* **357**, 1002 (2017).
- [240] D. DeMille, J. M. Doyle, and A. O. Sushkov, “Probing the frontiers of particle physics with tabletop-scale experiments”, *Science* **357**, 990 (2017).
- [241] S. Ospelkaus, K. K. Ni, K. Wang, M. H. G. de Miranda, B. Neyenhuis, G. Quemener, P. S. Julienne, J. L. Bohn, D. S. Jin, and J. Ye, “Quantum-state controlled chemical reactions of ultracold potassium-rubidium molecules”, *Science* **327**, 853 (2010).
- [242] F. H. J. Hall and S. Willitsch, “Millikelvin reactive collisions between sympathetically cooled molecular ions and laser-cooled atoms in an ion-atom hybrid trap”, *Phys. Rev. Lett.* **109**, 233202 (2012).
- [243] A. Micheli, G. K. Brennen, and P. Zoller, “A toolbox for lattice-spin models with polar molecules”, *Nat. Phys.* **2**, 341 (2006).
- [244] D. DeMille, “Quantum computation with trapped polar molecules”, *Phys. Rev. Lett.* **88**, 067901 (2002).
- [245] R. V. Krems, “Cold controlled chemistry”, *Phys. Chem. Chem. Phys.* **10**, 4079 (2008).
- [246] K. M. Jones, E. Tiesinga, P. D. Lett, and P. S. Julienne, “Ultracold photoassociation spectroscopy: long-range molecules and atomic scattering”, *Rev. Mod. Phys.* **78**, 483 (2006).
- [247] M. Yeo, M. T. Hummon, A. L. Collopy, B. Yan, B. Hemmerling, E. Chae, J. M. Doyle, and J. Ye, “Rotational state microwave mixing for laser cooling of complex diatomic molecules”, *Phys. Rev. Lett.* **114**, 223003 (2015).
- [248] J. E. van den Berg, S. H. Turkesteen, E. B. Prinsen, and S. Hoekstra, “Deceleration and trapping of heavy diatomic molecules using a ring-decelerator”, *Eur. Phys. J. D* **66**, 235 (2012).
- [249] J. E. van der Berg, S. C. Mathavan, C. Meinema, J. Nauta, T. H. Nijbroek, K. Jungmann, H. L. Bethlem, and S. Hoekstra, “Traveling-wave deceleration of SrF molecules”, *J. Mol. Spec.* **300**, 22 (2014).
- [250] S. E. Maxwell, N. Brahms, R. deCarvalho, D. R. Glenn, J. S. Helton, S. V. Nguyen, D. Patterson, J. Petricka, D. DeMille, and J. M. Doyle, “High-flux beam source for cold, slow atoms or molecules”, *Phys. Rev. Lett.* **95**, 173201 (2005).
- [251] J. F. Barry, E. S. Shuman, and D. DeMille, “A bright, slow cryogenic molecular beam source for free radicals”, *Phys. Chem. Chem. Phys.* **13**, 18936 (2011).
- [252] S. Truppe, M. Hambach, S. M. Skoff, N. E. Bulleid, J. S. Bumby, R. J. Hendricks, E. A. Hinds, B. E. Sauer, and M. R. Tarbutt, “A buffer gas beam source for short, intense and slow molecular pulses”, *J. Mod. Opt.* **65**, 648 (2018).
- [253] K. Esajas, “Intense slow beams of heavy molecules to test fundamental symmetries”, Ph.D. thesis (University of Groningen, 2021).

- [254] I. V. Hertel and C.-P. Schulz, *Atoms, molecules and optical physics 1* (Springer, 2015).
- [255] R. Boomstra, “Optimal coupling of a cryogenic source to a stark decelerator”, Bachelor thesis (University of Groningen, 2016).
- [256] A. Zapara, “Dynamics of molecular beams in a traveling-wave stark decelerator”, Ph.D. thesis (University of Groningen, 2019).
- [257] J. van der Berg, “Traveling-wave stark deceleration of SrF molecules”, Ph.D. thesis (University of Groningen, 2015).
- [258] M. R. Tarbutt, J. J. Hudson, B. E. Sauer, and E. A. Hinds, “Prospects for measuring the electric dipole moment of the electron using electrically trapped polar molecules”, *Faraday Discuss.* **142**, 37 (2009).
- [259] H. L. Bethlem, F. M. H. Crompvoets, R. T. Jongma, S. Y. T. van de Meerakker, and G. Meijer, “Deceleration and trapping of ammonia using time-varying electric fields”, *Phys. Rev. A* **65**, 053416 (2002).
- [260] S. Y. T. van de Meerakker, P. H. M. Smeets, N. Vanhaecke, R. T. Jongma, and G. Meijer, “Deceleration and electrostatic trapping of OH radicals”, *Phys. Rev. Lett.* **94**, 023004 (2005).
- [261] S. Hoekstra, M. Metsälä, P. C. Zieger, L. Scharfenberg, J. J. Gilijamse, G. Meijer, and S. Y. T. van de Meerakker, “Electrostatic trapping of metastable NH molecules”, *Phys. Rev. A* **76**, 063408 (2007).
- [262] J. J. Gilijamse, S. Hoekstra, S. A. Meek, M. Metsälä, S. Y. T. van de Meerakker, and G. Meijer, “The radiative lifetime of metastable CO ( $a^3\Pi$ ,  $v = 0$ )”, *J. Chem. Phys.* **127**, 221102 (2007).
- [263] C. Meng, A. P. P. van der Poel, C. Cheng, and H. L. Bethlem, “Femtosecond laser detection of Stark-decelerated and trapped methylfluoride molecules”, *Phys. Rev. A* **92**, 023404 (2015).
- [264] E. B. Norrgard, N. Sitaraman, J. F. Barry, D. J. McCarron, M. H. Steinecker, and D. DeMille, “In-vacuum scattered light reduction with black cupric oxide surfaces for sensitive fluorescence detection”, *Rev. Sci. Instrum.* **87**, 053119 (2016).
- [265] S. M. Vermeulen, “Time-resolved fluorescence signals of barium monofluoride”, Masters thesis (University of Groningen, 2019).
- [266] J. Muller, “Electric fields and molecule motion in a traveling-wave stark decelerator (bachelor’s thesis)”, PhD thesis (University of Groningen, 2017).
- [267] J. van Veldhoven, H. L. Bethlem, M. Schnell, and G. Meijer, “Versatile electrostatic trap”, *Phys. Rev. A* **73**, 063408 (2006).
- [268] M. Motsch, L. D. van Buuren, C. Sommer, M. Zeppenfeld, G. Rempe, and P. W. H. Pinkse, “Cold guided beams of water isotopologs”, *Phys. Rev. A* **79**, 013405 (2009).
- [269] M. Veltman, *Facts and mysteries in elementary particle physics* (World Scientific Pub, 2003).





# List of Publications

Parts of the work described in this thesis is summarised in the following articles:

- Y. Yin, P. Aggarwal, K. Esajas, H. L. Bethlem, A. Boeschoten, A. Borschevsky, S. Hoekstra, K. Jungmann, V. R. Marshall, T. B. Meijknecht, M. C. Mooij, R. G. E. Timmermans, A. Touwen, W. Ubachs, L. Willmann, *Details of the deceleration and trapping of SrF molecules*, (in preparation).
- P. Aggarwal, Y. Yin, K. Esajas, H. L. Bethlem, A. Boeschoten, A. Borschevsky, S. Hoekstra, K. Jungmann, V. R. Marshall, T. B. Meijknecht, M. C. Mooij, R. G. E. Timmermans, A. Touwen, W. Ubachs, L. Willmann, *Deceleration and trapping of SrF molecules*, arXiv:2103.07968 (submitted to Phys. Rev. Lett.) (2021).
- P. Aggarwal, H. L. Bethlem, A. Boeschoten, A. Borschevsky, K. Esajas, Y. Hao, S. Hoekstra, K. Jungmann, V. R. Marshall, T. B. Meijknecht, M. C. Mooij, R. G. E. Timmermans, A. Touwen, W. Ubachs, L. Willmann, Y. Yin and A. Zapara, *A supersonic laser ablation beam source with narrow velocity spreads*, Rev. Sci. Instrum. **92**, 033202 (2021).
- P. Aggarwal, V. R. Marshall, H. L. Bethlem, A. Boeschoten, A. Borschevsky, M. Denis, K. Esajas, Y. Hao, S. Hoekstra, K. Jungmann, T. B. Meijknecht, M. C. Mooij, R. G. E. Timmermans, A. Touwen, W. Ubachs, S. M. Vermeulen, L. Willmann, Y. Yin and A. Zapara, *Lifetime measurements of the  $A^2\Pi_{1/2}$  and  $A^2\Pi_{3/2}$  states in BaF*, Phys. Rev A. **100**, 052503 (2019).



# Acknowledgements

This dissertation is the most fulfilling project that I have ever undertaken and one that I could not have completed alone. I have been extremely fortunate to have had great teachers, mentors, friends and family to encourage me and I am grateful for their generosity in sharing their knowledge and consistent support.

First and foremost, I thank my daily supervisor Steven Hoekstra for giving me the opportunity to work in his group. Steven, I am extremely grateful for your patience with me during my Ph.D. tenure. You gave me the freedom to explore on my own and provided the much-needed guidance to recover when my steps faltered. You would always ask insightful questions during the weekly meetings and direct my course in the right direction. My second promoter, Klaus Jungmann has always been happy to provide mentorship, advice and guidance. Klaus, I'm thankful for your constructive criticism on my papers and my thesis, which helped my work to shape well.

I would like to thank Lorenz Willmann, for his insights and work on the lifetime measurements. Lorenz, it has been inspiring to see you work tirelessly in the lab to get the measurements done, even when that involved working on the weekends. I furthermore want to thank Rick Bethlem for his useful suggestions to obtain the first signal from the supersonic source, his suggestions on the successful operation of the cryogenic source and the Stark decelerator. I would like to express my gratitude to Wim Ubachs for always providing quick and detailed feedback on my papers.

I would like to express my gratitude to the members of the Assessment Committee, Caspar van der Wal, Silke Ospelkaus and Florian Schreck for their careful reading of my thesis and for providing their feedback. Furthermore, I would also like to thank the members of the Examining Committee for agreeing to be part of the opposition at my defense.

I would like to thank Leo Huisman, without whom everything in the cold molecules laboratory would fall apart. Leo, it still amazes me how you manage to help a dozen people at the same time. Thank you for bearing with my impatient attitude, allowing me to disturb your peaceful morning time in the office and giving me a new name 'Pareltje'. I also express my gratitude to Andre, Dirk, Nanko and Sandra from the KVI workshop, for always agreeing to engineer useful parts for our experimental setup. I would also like to thank Hilde van der Meer for helping me with the administrative aspects and also for her amazing organization of the team events.

I have had the privilege of working with the most wonderful and helpful people in the lab. Special thanks to my fellow labmates, Artem and Kevin. Although we were all working on different projects in the beginning, both of you were always willing to provide help in every possible way and find solutions to my problems as if they were your own. If this

dissertation had co-authors, it would have to be you both. I would like to thank Yanning, for our successful collaboration on the cryogenic source and decelerator project. Yanning, your enthusiasm to finish the task at hand on the same day was primarily responsible for our rapid progress on the experiment in a short period of time. Later, even when you moved to Basel for your new job, you would always accommodate my requests for running new simulations for my thesis, which I highly appreciate. I would like to thank Ginny. Ginny, I enjoyed your company while working on the lifetime measurements. Your happy and cheerful nature kept us going during the initial setbacks. We shared our first research publication which would always stay special to me.

I am thankful to Mina, for being the nicest office mate. Mine, I enjoyed our discussions on food recipes. Thanks for always bringing me nice food. I also acknowledge tedious work by Hidde on the alignment of the decelerator. I would like to thank Anno and Joost for taking over the work on the decelerator so that I can focus on my thesis writing. I wish them a lot of success in taking the experiment forward. I also acknowledge work on the experiment by other Bachelor and Master students; Bernard, Celine, Jeroen, Robin and Thya. I would like to thank Oliver Boll for the lasers and optics-related advice and specifically in assisting me in my first attempt of trying to couple the laser light into an optical fiber.

I would further extend my thanks to all other former and present colleagues: Alexander, Elwin, Maarten, Malika, Nivedya, Olivier, Pi, Thomas and Yongliang for the nice physics discussions and fun times outside of work. I also express my sincere gratitude to other staff members at the VSI: Gerco Onderwater, Anastasia Borschevsky, Julia Even and Rob Timmermans.

I also owe thanks to the Personnel department at Nikhef, especially for their help with the visa process and also for familiarising me with different things once I reached the Netherlands. I also appreciated the nice encouraging notes posted to our home addresses by Nikhef during the initial days of complete lockdown. Further, I would like to thank Nederlandse Organisatie voor Wetenschappelijk Onderzoek (NWO) for funding this research.

I would like to thank Sasi and Hyoyin for their friendship and for agreeing to be my paranymphs. Sasi, you were my saviour for the last four years. Hyoyin, thanks for helping me develop a nice running routine. Francesco, thanks for organising the nice cycling trips.

I would like to thank Dr. Nataraj Hulyar for his constant encouragement and trust in my abilities. Thank you for agreeing to write me the recommendation letters. I would like to thank Prof. Ajay Wasan for supervising me on my Master's research project, wherein I got the first-hand experience of working in a research lab.

Last and most importantly, thank you to my longest, unwavering supporters: my parents Sanjeev and Poonam and my brother Hitesh. Thank you for always supporting my career choices. I would not have been able to achieve anything without your constant encouragement.

Parul Aggarwal  
July, 2021